Low Momentum Direct Photons as a Probe of Heavy Ion Collisions

A Dissertation Presented

by

Richard Michael Petti

to

The Graduate School

in Partial Fulfillment of the Requirements

for the Degree of

Doctor of Philosophy

in

Physics

Stony Brook University

December 2013

Stony Brook University

The Graduate School

Richard Michael Petti

We, the dissertation committee for the above candidate for the Doctor of Philosophy degree, hereby recommend acceptance of this dissertation.

Axel Drees – Dissertation Advisor
Professor, Department of Physics and Astronomy

Derek Teaney – Chairperson of Defense
Professor, Department of Physics and Astronomy

Robert McCarthy
Professor, Department of Physics and Astronomy

Gabor David
Physicist, Brookhaven National Lab

This dissertation is accepted by the Graduate School.

Charles Taber
Dean of the Graduate School

Abstract of the Dissertation

Low Momentum Direct Photons as a Probe of Heavy Ion Collisions

by

Richard Michael Petti

Doctor of Philosophy

in

Physics

Stony Brook University

2013

Relativistic heavy ion collisions have been a major research interest in the field of nuclear physics for the past few decades. Large collider facilities have been constructed to study the exotic matter produced in relativistic heavy ion collisions, one of which is the Relativistic Heavy Ion Collider (RHIC) at Brookhaven National Laboratory in Upton, NY. Essential to the study of heavy ion collisions are probes that are produced in the collision itself. Photons are a very useful probe of the collisions, since they escape the fireball virtually unmodified and carry with them information about the environment in which it was produced. Recent interest in low momentum direct photons has increased, due to the onset of the “thermal photon puzzle” and the apparent inability for typical models to explain both a large direct photon yield excess and large azimuthal production asymmetry (v_2) at low momentum measured by PHENIX. The focus of this thesis will be the measurement of direct photons at low momentum with the PHENIX detector in $\sqrt{s_{NN}} = 200 GeV$ Au+Au collisions.

Low momentum direct photons (direct is any photon not from a hadron decay) are notoriously difficult to measure in a heavy ion environment, due to large decay photon backgrounds, neutral hadron contamination, and worsening calorimeter resolution. A novel technique for measuring direct photons via their external conversion to di-electron pairs has been developed. The method virtually eliminates the neutral hadron contamination due to the very clean photon identification based on di-electron pair invariant mass cuts. The direct photon fraction, R_γ, defined as the ratio of the yield of inclusive photons to hadron decay photons, is measured through a double ratio further reducing systematic uncertainties to manageable levels at low momentum. The direct photon fraction is converted to a direct photon invariant yield and a detailed look at the centrality dependence of the excess yield is presented. This dependence is confronted with recent theoretical calculations predicting novel production mechanisms of direct photons and possible solutions to the “thermal photon puzzle”.

Dedicated to my family, both my parents and little sis who put me on my current trajectory in life and without their support this would not have been possible, and the family that I am creating who help me to push into the future. I also want to express my gratitude to my thesis advisor Axel Drees for getting me through this analysis and to the rest of the Stony Brook heavy ion group.

Contents

List of Figures **ix**

List of Tables **xiii**

1 Introduction **1**
- 1.1 Quantum ChromoDynamics, QCD 2
  - 1.1.1 Running of the Coupling Constant and Asymptotic Freedom 3
  - 1.1.2 Color Confinement 5
- 1.2 Heavy Ion Collisions and the Quark Gluon Plasma 6
  - 1.2.1 Early Time Physics: the Color Glass Condensate and the Glasma 8
  - 1.2.2 Early Time Physics: Strong Magnetic Fields 11
  - 1.2.3 v_2 and Elliptic Flow 13
- 1.3 Direct Photon Production 15
  - 1.3.1 Direct Photon Production at High Transverse Momentum 16
  - 1.3.2 Direct Photon Production at Low Momentum, Thermal Photons 18
- 1.4 The Thermal Photon Puzzle 18
- 1.5 Purpose of this Dissertation 25

2 The Experiment **27**
- 2.1 The RHIC Facility 27
- 2.2 The PHENIX Coordinate System 28
- 2.3 The PHENIX Detector 30
  - 2.3.1 Global Detectors 30
  - 2.3.2 Charged Particle Tracking System 35
  - 2.3.3 Electron ID Detectors 44
  - 2.3.4 Electromagnetic Calorimeter 47
  - 2.3.5 Data Acquisition System (DAQ) 50
  - 2.3.6 Event Triggers 51

3 Photon Identification Via External Conversions 53
3.1 Simulations of External Conversion Sources 54
3.2 The Alternate Track Model 58
3.3 Photon ID Cuts 64
3.4 Purity of the Photon Sample 64

4 Analysis: Invariant Yield of Direct Photons 67
4.1 Run QA 68
4.2 Direct Photon Fraction, R_γ 69
  4.2.1 Inclusive Photon Yield 70
  4.2.2 Pion Decay Tagged Photon Yield 72
  4.2.3 The Hadron Decay Photon Cocktail 74
  4.2.4 Corrections from Monte Carlo Simulations 82
  4.2.5 Systematic Uncertainties 96
4.3 Invariant Yield of Direct Photons 108
  4.3.1 Systematic Uncertainties 108
  4.3.2 The Corrected Inclusive Photon Invariant Yield 111

5 Results: Direct Photon Invariant Yield 113
5.1 Results: R_γ 113
5.2 Results: Invariant Yield 113

6 Analysis: v_2 of Direct Photons 119
6.1 Reaction Plane Resolution 120
6.2 Inclusive Photon v_2 122
6.3 Neutral Pion and Hadron Decay Photon v_2 124
6.4 Systematic Uncertainty 128
  6.4.1 Systematic on the Reaction Plane Resolution 129
  6.4.2 Systematic on the Inclusive Photon v_2 129
  6.4.3 Systematic on the Decay Photon v_2 134

7 Results: Direct Photon v_2 135

8 Discussion 139
8.1 The Direct Photon Yield 139
8.2 The Direct Photon v_2 152
8.3 The Thermal Photon Puzzle 152
  8.3.1 The Closing of the QGP Radiation Window 153
  8.3.2 Novel Sources of Direct Photons 157
8.4 Conclusions 163

Bibliography 169

A Data Tables **170**

List of Figures

1.1 Running of the Coupling Constant α_s 4
1.2 Color Confinement 5
1.3 The Phase Diagram of Nuclear Matter 7
1.4 The Evolution of a Heavy Ion Collision in Time 7
1.5 The CGC Picture of a Heavy Ion Collision 8
1.6 Parton Distributions within a Hadron 9
1.7 Gluon Packing in a Hadron 9
1.8 A sheet of CGC 10
1.9 The Passing Of CGC Sheets 11
1.10 Relaxation of the Magnetic Field 13
1.11 Definition of the Reaction Plane 14
1.12 Flow Harmonics 15
1.13 Feynman Diagrams for Direct Photon Production (LO) 17
1.14 Feynman Diagrams for the Production of Direct Photons from the Medium 17
1.15 Previously Published Invariant Yield of Direct Photons from Virtual Photons 19
1.16 The Direct Photon Invariant Yield Compared to Theory . . . 21
1.17 Previously Published Direct Photon v_2 22
1.18 Previously Published Direct Photon v_2 Compared to Theory . 23
1.19 A Calculation of the Evolution of v_2 With Time 24
1.20 A Calculation of the Thermal Photon v_2 25

2.1 The RHIC facility 28
2.2 Coordinate System 29
2.3 Relation Between η and θ 30
2.4 The PHENIX Detector 31
2.5 Beam-Beam Counters 32
2.6 ZDC Tungsten Module 32
2.7 RXPN Detector 33
2.8 BBC Charge Sum for Centrality Determination 34

2.9 Magnetic Field Configurations 36
2.10 The Drift Chamber Frame 37
2.11 A Drift Chamber Keystone 38
2.12 The Wire Layout of a KeyStone 39
2.13 A Schematic of the Pad Chamber 40
2.14 Tracking in the Central Arms 41
2.15 Hough Transform 42
2.16 The RICH Detector 45
2.17 HBD Detector 46
2.18 Lead Scintillator EMCal Sector 48
2.19 Lead Glass EMCal Supermodule 49
2.20 The PHENIX DAQ 51

3.1 Reconstruction Cartoon 55
3.2 Simulation Conversion Radiogram 56
3.3 Invariant Mass of Simulated Conversions 57
3.4 Pair Invariant Mass in Vertex Bins 57
3.5 Recalibration of p_T 60
3.6 Recalibration of ϕ 61
3.7 Recalibration of θ 61
3.8 ATM Residuals 62
3.9 ATM Invariant Mass of Simulated Conversions 63
3.10 2D Mass Space in MB Data 65
3.11 2D Mass Plot for Different Conversion Sources 66

4.1 Run QA 68
4.2 The Raw Inclusive Per Event Yield as a Function of p_T 72
4.3 π^0 Extraction: FG with normalized combinatorial BG 73
4.4 π^0 Extraction: Obtaining the Normalization for the Combinatorial BG 75
4.5 The Subtracted Pion Signal 76
4.6 The Yield of Photons Tagged as Coming From a π^0 Decay . . 77
4.7 Parameterization of the Pion Invariant Yield for the Cocktail . 78
4.8 The Hadron Cocktail 80
4.9 The Centrality Dependence of the Cocktail Ratio 81
4.10 Comparison of Single Electron Cuts in Data and Simulation . 83
4.11 Comparison of Single Positron Cuts in Data and Simulation . 84
4.12 Charged Track Dead Map Comparison in Data and Simulation 85
4.13 Comparison of Emcal χ^2 Cut in Data and Simulation (PbSc) . 86
4.14 Comparison of Emcal χ^2 Cut in Data and Simulation (PbGl) . 87
4.15 Photon Reconstruction Efficiency in the Emcal 88

4.16 Comparison of Pion Reconstruction in Data and Sim: Mean . 89
4.17 Comparison of Pion Reconstruction in Data and Sim: Width . 90
4.18 Comparison of Pions to Published Results 91
4.19 The Pion Acceptance And Efficiency Correction 93
4.20 The Pion Acceptance And Efficiency in More Detail 94
4.21 The Pion Tagging Efficiency and Acceptance 95
4.22 The Reconstruction of Pions with Late Conversions 96
4.23 Conversions from Material in PHENIX 97
4.24 Systematic Uncertainties on R_γ 99
4.25 Systematic Uncertainty on Pion Extraction 99
4.26 Systematic on the Photon Reconstruction Efficiency (I) 100
4.27 Systematic on the Photon Reconstruction Efficiency (II) . . . 101
4.28 Emcal Hit Maps in Simulation and Data 102
4.29 Percent Masked Area in Data and Simulation 102
4.30 Systematic Uncertainty Due to the Energy Scale Mismatch . . 103
4.31 Correction Parameterization Uncertainty 103
4.32 R_γ Calculated With and Without Correction Smoothing . . . 104
4.33 Ratios of Bin by Bin Corrected and Parameterized Correction R_γ 105
4.34 Tsallis Parameterization for Input Pions on Cocktail Ratio . . 107
4.35 Systematic on Cocktail Ratio from Meson to Pion Ratios . . . 108
4.36 η/π^0 From the Cocktail Compared to Data 109
4.37 Test of m_T Scaling Assumption 109
4.38 Systematic on the Cocktail 110
4.39 Corrected Inclusive Photon Yield with Correction 112

5.1 Raw Inclusive to Pion Tagged Photon Ratio 114
5.2 Raw Inclusive to Pion Tagged Photon Ratio in Two Run Groups 114
5.3 $R\gamma$ in Centrality Bins 115
5.4 The Minimum Bias R_γ 115
5.5 R_γ vs Centrality 116
5.6 Direct Photon Invariant Yield (MB) 116
5.7 Centrality Binned Direct Photon Invariant Yield 117
5.8 Comparison of Centrality Binned Yields to Previous Publication 117
5.9 Comparing Two Calculations of the Direct Photon Yield . . . 118

6.1 Extracting the Reaction Plane Resolution Parameter 121
6.2 Reaction Plane Resolution 122
6.3 Correlation Function for Azimuthal Distribution in Min. Bias 123
6.4 Comparison of Run Group Results 124
6.5 Inclusive Photon v_2 125
6.6 Inclusive Photon v_2 Compared with Published Result 126

6.7 Parameterizing the Pion v_2 127
6.8 Hadron Decay Photon v_2 from the Cocktail 128
6.9 Inclusive Photon v_2 Determined With Only North or South Detector 130
6.10 North Only v_2 Comparison 131
6.11 South Only v_2 Comparison 132
6.12 Compare Inclusive Photon v_2 from Two Methods 133
6.13 Systematic on Hadron Decay v_2 from Cocktail Normalization . 134

7.1 The Direct Photon v_2 136
7.2 Compare v_2^{direct} with Published 137
7.3 Compare v_2^{direct} to v_2^{incl} and $v_2^{\pi^0 decay}$ 138

8.1 Fits to the p+p Direct Photon Spectra 140
8.2 Direct Photon Spectra in Au+Au Collisions from 0 to 20GeV 142
8.3 Direct Photon Spectra in Au+Au Collisions 143
8.4 The Subtracted Excess from Each p+p Parameterization . . . 144
8.5 Systematic Uncertainty from the Extrapolation from the p+p Data 145
8.6 The Excess Direct Photon Yield Above pQCD Processes . . . 146
8.7 Exponential Fits to Direct Photon Excess 148
8.8 Local Slopes of Direct Photon Excess 149
8.9 Yield Vs. N_{part} 150
8.10 N_{part} Power Law Scaling 151
8.11 Yield Vs. Number of Quark Participants 151
8.12 N_{qp} Power Law Scaling 152
8.13 Comparison of the Direct Photon v_2 to Published Results . . . 153
8.14 Comparison to Theory Spectra (I) 155
8.15 Theory Comparison of v_2 (I) 155
8.16 Comparison to Theory (PHSD) 156
8.17 Calculation of Glasma Photon Emission 159
8.18 Comparison to Theory Spectra (II) 159
8.19 Triangle Diagram for Conformal Anomaly 161
8.20 Yield of Photons from the Conformal Anomaly 162
8.21 Comparison of v_2 to Theory: Conformal Anomaly 162

List of Tables

4.1 Input Parameters to Cocktail 79
4.2 Hadron to Neutral Pion Ratios 79
4.3 Extracted Radiation Length 92
4.4 Systematic Uncertainty Summary on R_γ 98

6.1 Systematic Uncertainty on the Direct Photon v_2 129

8.1 Glauber Calculated Values Describing Collision Centrality . . 141
8.2 Inverse Slope Parameter from Exponential Fits 147

A.1 Data Table for R_γ 0-20% Centrality 170
A.2 Data Table for R_γ 20-40% Centrality 171
A.3 Data Table for R_γ 40-60% Centrality 171
A.4 Data Table for R_γ 60-90% Centrality 172
A.5 Data Table for R_γ MB Centrality 172
A.6 Data Table for Inclusive Yield MBCentrality 173
A.7 Data Table for γ^{direct} 0-20% Centrality 173
A.8 Data Table for γ^{direct} 20-40% Centrality 174
A.9 Data Table for γ^{direct} 40-60% Centrality 174
A.10 Data Table for γ^{direct} 60-90% Centrality 175
A.11 Data Table for γ^{direct} MB Centrality 175
A.12 Data Table for v_2^{incl} $0 - 20\% Cent.$ 176
A.13 Data Table for v_2^{incl} $20 - 40\% Cent.$ 176
A.14 Data Table for v_2^{incl} $40 - 60\% Cent.$ 177
A.15 Data Table for $v_2^{incl} Min.Bias$ 177
A.16 Data Table for $v_2^{direct} Min.Bias$ 178

Chapter 1

Introduction

Man has looked to the heavens and pondered his own existence and place in the universe since the beginning of scientific inquiry. These ponderings continue today, where scientists from all over the globe dedicate their lives to the pursuit of knowledge on the basic building blocks of matter and their fundamental interactions.

As our exploits have continued and time passed we have uncovered the structure of matter to finer and finer scales. Ancient Greek philosophers (around the 5th century BCE) pondered about the building blocks of matter and first came up with the notion of the atom, that matter as we see it is built up of smaller discrete (and indivisible) components. It was not until much later we began seeing real evidence for this type of structure.

In 1909, Hans Geiger and Ernest Marsden, lead by Ernest Rutherford, made the first observation of the nucleus of the atom with their famous gold foil experiment [1] [2], where α particles were fired at a gold sheet only a few atoms thick. It was observed that most α particles passed through with little deflection. But once in a while α particles would be scattered at a very large angle (greater than $90°$). This indicated that the bulk of charge and mass of an atom was concentrated (and of positive charge) and that the atom was mostly empty space. Before this, the concept of the atom was characterized by the plum-pudding model, with electron "plums" immersed in a sea of positively charged pudding.

As time passed and scattering experiments occurred at higher and higher energies, it was discovered that the nucleon was not indivisible, but had a substructure as well. In 1968, deep inelastic scattering experiments were performed at the Stanford Linear Accelerator Center (SLAC), where high energy electrons were fired at nuclei. Analogous to Rutherford scattering, but at higher energies (so probing smaller length scales), it was found that nuclear matter seems to be made up of smaller point-like particles (coined partons at the time). This observation confirmed emerging theories and was an important step in verifying Quantum ChromoDynamics (QCD) as a correct theory to describe how these partons interact.

Many experiments and tests of QCD have been performed over the years and QCD seems to describe what we observe experimentally quite well, making it is a great success of modern nuclear physics. There are currently large accelerator programs (such as SPS, RHIC, and LHC) comprising multi-national efforts to study QCD and the interactions of partons. At these large colliders, we have evidence that a state of matter has been created in which the fundamental partons of the nucleus (quarks and gluons, collectively called partons) are freed from the protons and neutrons in the nucleus. This state of matter is called the Quark Gluon Plasma, or QGP. It is thought that this state of matter existed in the first early microseconds of the Big Bang at the creation of our universe, and now we get a glimpse of this matter in the laboratory. The study of this QGP matter with a photon probe is discussed within this thesis.

1.1 Quantum ChromoDynamics, QCD

Quantum ChromoDynamics (QCD) is a quantum field theory describing the interactions of quarks and gluons. The fundamental force governing these interactions is known as the strong force. The gluon is the gauge boson which mediates the force within the theory. Under the theory, there are three 'color' charges (analogous to the charge in QED). The gauge group chosen to represent the phase transformations of the color fields is the SU(3) gauge group. As is done with QED, the structure of QCD (i.e. the Lagrangian) can be inferred from symmetry considerations. A local gauge invariance is imposed on transformations of the color fields with respect to the Lagrangian. This means that the Lagrangian is unchanged under a particular form of transformation of the field. Starting with the free Lagrangian, one can work out the consequences of requiring local gauge invariance on SU(3) [3]. The gauge invariant Lagrangian for QCD is shown in Eqn. 1.1, where summation over repeated 'a' indicies is implied.

$$L = \overline{q}(\imath\gamma^{\mu}\partial_{\mu})q - g(\overline{q}\gamma^{\mu}T_{a}q)G^{a}_{\mu} - \frac{1}{4}G^{a}_{\mu\nu}G^{\mu\nu}_{a} \tag{1.1}$$

$$G^{a}_{\mu\nu} = \partial_{\mu}G^{a}_{\nu} - \partial_{\nu}G^{a}_{\mu} - gf_{abc}G^{b}_{\mu}G^{c}_{\nu} \tag{1.2}$$

In QED a vector field needs to be introduced to enforce local gauge invariance (the photon field). This is also true for QCD, but there are eight vector gluon fields, indexed by ‘a’ in Eqn. 1.1. The last term in Eqn. 1.1 is the kinetic term. The kinetic term also needs to be gauge invariant, and so can only involve the gauge invariant field strength tensor, defined in Eqn. 1.2. There is an extra term in the field strength tensor of QCD compared the QED case due to the non-Abelian nature of the SU(3) group. The transformations of the SU(3) group do not commute, giving rise to the third term in Eqn. 1.2 involving the structure functions from the commutator relations.

This extra term leads to very different behavior of QCD compared to QED. It acts as a self-interacting term for the gluon fields. This means that not only do we get quark-gluon (qg) vertices in QCD (analogous to electron-photon (eγ) vertices in QED), but we also get gluon-gluon (gg) vertices where gluons can interact with one another. There is no analog to this in QED, this is strictly a property of non-Abelian gauge groups.

The non-Abelian nature of the theory has two important consequences for the partonic interactions, asymptotic freedom and confinement. These two important phenomena arise from interactions with the quantum vacuum. These interactions lead to a running of the coupling “constant”. The quantum vacuum is not simply empty space in the classical sense. Because of inherent uncertainty within nature (the Heisenberg uncertainty principle), the vacuum actually consists of constantly fluctuating energy distributions. This is the inherent fuzziness of nature, no matter how precise a measurement is, it can never overcome this.

1.1.1 Running of the Coupling Constant and Asymptotic Freedom

The energy fluctuations of the quantum vacuum can manifest as the production of $q\overline{q}$ pairs (or e^+e^- pairs in QED). From this, it follows that there is a charge screening effect due to the quantum vacuum.

It may be most natural to think of this through an example in QED. As a charged particle sits in the vacuum, it can actually polarize the vacuum, the dilepton pairs will be preferentially oriented due to the particle present. As such, in the example of an electron, the electron will be surrounded by a cloud of positive charges. And this screens the electron, so that the charge one measures is dependent on the distance from that charge. In QED, the charge measured increases as distance to the charge decreases (close enough to penetrate the positron cloud). This effect is technically known as the running of the coupling constant.

There is a similar screening in QCD with the color charges, but because the gluons are also colored and self-interact, this screening gives rise to a completely different running of the coupling constant than in QED.

$$\alpha_s(Q^2) = \frac{12\pi}{(33-2n_f)log(Q^2/\Lambda^2)} \tag{1.3}$$

Th running in QCD is shown mathematically in Eqn. 1.3, and graphically in Fig. 1.1. In Eqn. 1.3, $Q^2 = -q^2$ where q is the momentum transfer at an interaction vertex, Λ is related to a parameter introduced in the renormalization of the calculation to avoid infinite terms by introducing a scale, and n_f is the number of flavors. Fig. 1.1 shows the calculated $\alpha_s = g^2/4\pi$ compared to various measurements as detailed in the reference. In QCD, the closer one is to the charge, the smaller the measured charge will be. This is known as asymptotic freedom. If two quarks are close enough, they will feel no force between them and act as free particles. Perturbative calculations can be used in the regime of close distances (or high energy), where the coupling is small. Different techniques must be used in the lower energy, non-perturbative regime. Relating this to Eqn. 1.3 the coupling is small when $Q^2 >> \Lambda^2$, and so a perturbative approach makes sense. When Q^2 is of the order of Λ^2, the coupling is no longer small and so quarks and gluons form tightly bound hadrons. Λ then in a sense marks the boundary of the world of quarks and gluons and that of pions and nucleons.

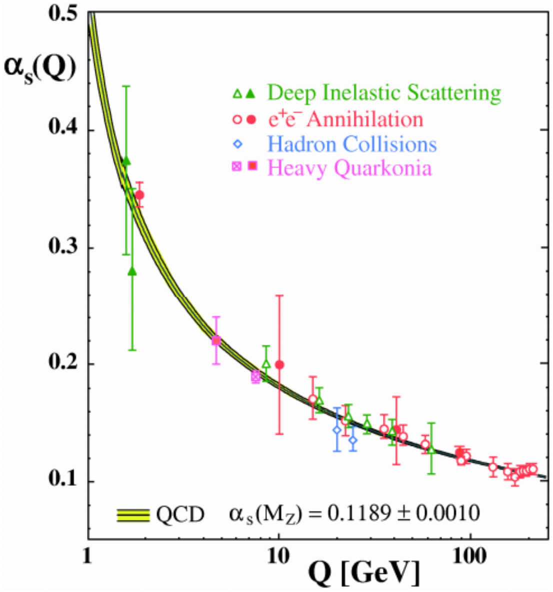

Figure 1.1: $\alpha_s(Q)$ calculated in QCD compared to measurements shown as data points [4].

1.1.2 Color Confinement

Confinement is another important consequence of QCD and the running of the coupling constant. It seems that nature keeps colored objects confined within color neutral objects. Indeed, no one has yet to directly observe a quark (we measure hadrons which fragment from the quark). This can be rationalized if one considers two color charges moving apart from one another. As discussed, the potential energy increases as the distance is increased. The potential energy will increase until the point where there is enough energy to form another $q\bar{q}$ pair, in which case the flux tube connecting the $q\bar{q}$ pair will split into two lower energy tubes, with some of the energy going into the production of more $q\bar{q}$ pairs to fill the open end of the tube. This is why we can never directly observe a bare quark or gluon. The above description is depicted in Fig. 1.2. That of course does not mean we have no way to study the quark properties. We must resort to studying the quark indirectly through its fragmentation process in jet events (in e^+e^- and pp collisions). We can also study QCD in relativistic heavy ion collisions, as this pertains to the subject of this thesis.

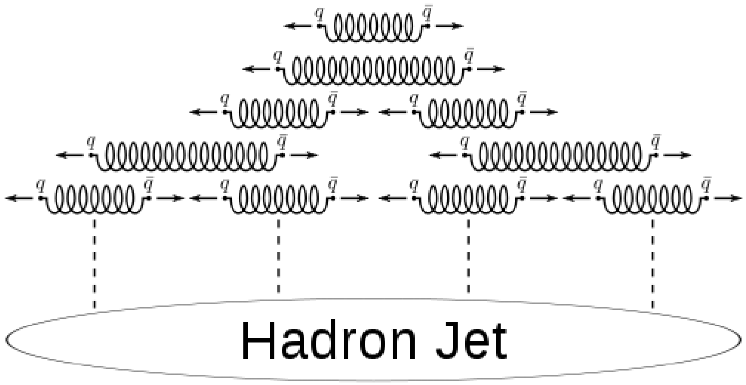

Figure 1.2: A cartoon illustrating quark confinement. The top row depicts a $q\bar{q}$ pair moving away from each other. As they move apart, the flux tube connecting them gets longer, indicating an increase in potential energy. Eventually it becomes more energetically favorable for the tube to break to form a new $q\bar{q}$ pair, closing the open ends of the broken flux tubes, and resulting in two lower energy tubes. This process continues until it is no longer energetically favorable to do so.

Relativistic heavy ion collisions are a testbed for QCD and push how much we can learn and extract from the theory. This requires hand in hand cooperation between theorists and experimentalists to keep the field alive and prosperous. It turns out that at high baryon density and/or high temperature, quarks can become deconfined and become the relevant degrees of freedom of the system. And this is the regime that can be probed in relativistic heavy ion collisions and is one of the major purposes for the PHENIX experiment and the RHIC program. The temperature and density dependence of nuclear matter can be mapped out in a phase diagram. Mapping out this phase diagram and the existence of a critical point between hadronic matter and quark matter is one of the major goals of the RHIC program. The state of matter in which the quarks and gluons become deconfined from their hadronic prisons is named the Quark Gluon Plasma (QGP) and is the subject of the next section.

1.2 Heavy Ion Collisions and the Quark Gluon Plasma

As temperature and/or baryon density increase into the extremes, normal nuclear matter that we encounter every day ceases to exist. The world of protons and neutrons dissolves and in its place is a world where individual quark and gluon interactions become the main driver of the physics. The state of matter in which colorless objects dissolve and partons become the relevant degrees of freedom is named the Quark Gluon Plasma (QGP). The basic phase diagram of nuclear matter is shown in Fig. 1.3.

The approximate region of the diagram probed by RHIC is shown in the diagram. The QGP is produced in the laboratory by colliding heavy ions together at high energy. The system starts very hot, and cools as it expands, hence the arrow on the figure indicating the evolution of the system on the phase diagram. Fig. 1.4 shows a cartoon of the basic time evolution of a heavy ion collision from initial creation of the QGP to the freezeout of the expanding hadronic matter.

The cartoon starts with two gold nuclei (moving in and out of the page) colliding. In the picture, the impact parameter is non-zero and, since the gold nuclei have a finite radius, leads to a region of overlap where the participant particles interact, shown by the colored "particles". The rest of the nucleons in the colliding nuclei are called spectators, since they do not interact to form the QGP. There are many interactions occurring here that can affect the final state hadrons that are observed. There are cold nuclear matter effects that are observed to exist in d+Au collisions (where no QGP is expected to form) and include modification of the parton distribution function for nucleons inside a nucleus, momentum broadening from partons scattering in the nucleus and energy loss in the nucleus [5] [6] [7]. These are mostly irrelevant in the context of this thesis, since these effects are not observed for direct photons [8].

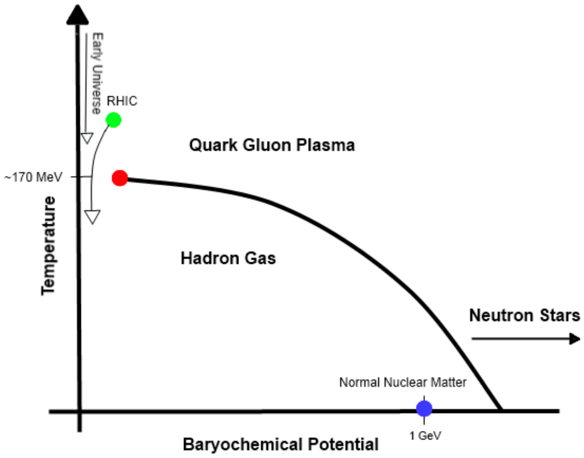

Figure 1.3: A schematic of the phase diagram of nuclear matter as a function of temperature and baryochemical potential

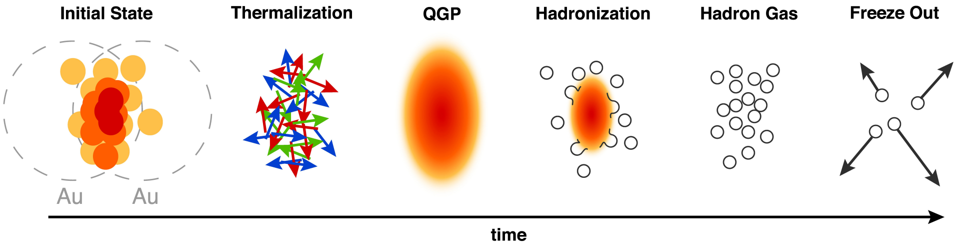

Figure 1.4: A cartoon of the evolution of a heavy ion collision. The system evolves forward in time as you move from left to right. Each stage is discussed in the text.

Next, through some interactions that are not fully understood, the system becomes thermalized. One possible explanation uses the concepts of the Color Glass Condensate (CGC) and the Glasma. These concepts will be elaborated upon further in Sec. 1.2.1. Then the QGP is formed. Here the nucleons are melted into their constituent partons. The effects of pressure gradients are expected to cause the partons to flow and indeed there is evidence that the system begins to flow at the parton level [9]. As the system cools and expands, the partons hadronize and get locked up into colorless particles, such as pions, as the system undergoes a phase transition to a hadron gas. Particle interactions are still taking place, but they are no longer of partonic origin. Finally as the system expands further, freezeout occurs and the hadron gas becomes non-interacting. The formed particles and decay products of unstable particles free-stream to the detectors. This, in a nutshell, is the basic picture a of heavy ion collision and the formation of the QGP in the laboratory.

1.2.1 Early Time Physics: the Color Glass Condensate and the Glasma

There is not much currently known about the very early time dynamics of the heavy ion collisions. One such description involves the concept of the Color Glass Condensate [10]. The Color Glass Condensate gives a description of the colliding ions before they collide by considering a highly coherent, high energy density ensemble of gluon states. As the sheets of colored glass pass through each other, the fields interact and form the Glasma. Then the glasma evolves into the thermalized QGP. We can amend the view of a heavy ion collision in Fig. 1.4 with this description to get the view of 1.5.

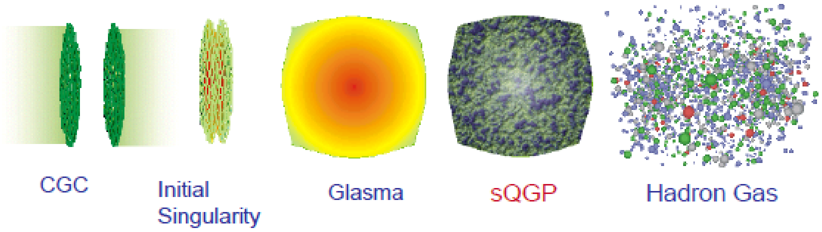

Figure 1.5: A visualization of a heavy ion collision within the CGC and glasma framework.

As stated, the initial incoming ions before the collision can each be described as a sheet of CGC. The Lorentz contraction of the relativistic ions causes them to appear more as pancakes in the lab frame and so can be described as sheets. One essential property of the CGC is how gluons occupy their states, and how this occupation is large in the high energy limit of QCD for the hadron. It is useful to express the energy of the constituents of a hadron as a fraction of energy that constituent holds compared to the entire hadron, or $x = E_{constituent}/E_{hadron}$. A high energy hadron implies that there are many low x gluons in the hadron. The gluon interaction cross-section grows slowly with increasing energy. Along with this, the gluon distribution rises rapidly as $x \to 0$. The parton distributions as a function of x is shown in Fig. 1.6. This implies that there must be a very high density of low x gluons inside the hadron at high energy.

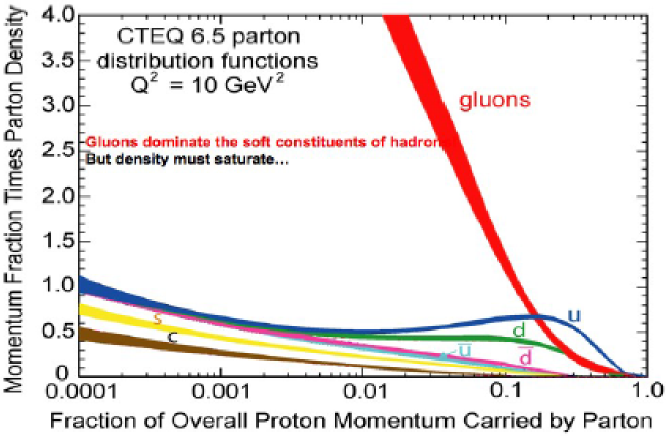

Figure 1.6: The distribution of quarks and gluons inside a hadron of particular energy as a function of x, the fractional energy of a parton to its parent hadron.

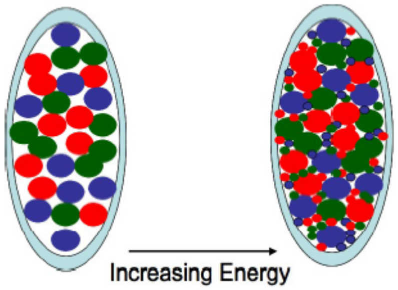

Figure 1.7: An illustration of the packing of gluons in a hadron as the hadron energy is increased.

Fig. 1.7 illustrates how the packing of gluons increases as a function of energy. Since the density is very high, gluons are packed very tightly and thus intrinsically have a small interaction strength (via asymptotic freedom in QCD, Sec. 1.1.1). But these interactions can act coherently and so can become strong inside the hadron. The phase space density is the occupation number of quantum mechanical states. And so as phase space density increases in the high energy limit, the occupation number increases to the point where the gluons can be treated as classical fields. Note that it is only the low x gluons which can be treated as classical fields. High x gluons cannot and are treated as static sources.

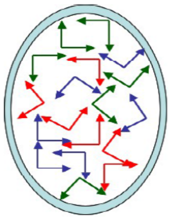

Figure 1.8: An illustration of the color fields inside a sheet of color glass condensate.

A sheet of CGC can be viewed in Fig. 1.8. The vectors represent the color electric and magnetic fields. As can be seen in the figure, $\vec{E}$, $\vec{B}$, and $\hat{z}$ are all orthogonal to one another. $\vec{E}$ is the color electric field, $\vec{B}$ is the color magnetic field, and $\hat{z}$ points along the beam direction (perpendicular to the page). The fields have random polarizations and colors. The strength of the fields are determined by the sources.

Now imagine the case of a heavy ion collision where two sheets of CGC are heading toward each other. The classical field of one ion propagating along the light cone z = t is superimposed with the classical field of the other ion propagating along the light cone z = -t to obtain the initial classical field. This is the description until the hadrons collide, in which case one must solve the classical Yang-Mills equations in the forward light cone.

Fig. 1.9 illustrates what happens as the CGC sheets pass through one another. In addition to the transverse fields present in each of the CGC sheets, longitudinal fields are produced. They form on a very short time scale and the production is associated with the initial singularity in the high energy limit of the collision. These longitudinal fields are produced by the surface color charge induced as the hadrons pass. The induced color electric and color magnetic charges are equal and opposite on each hadron. The matter produced here has different properties than the CGC, due to the longitudinal fields. This stage of matter will transition from the CGC into the quark gluon plasma and so is named by the authors as the glasma. The fields become more disperse as the

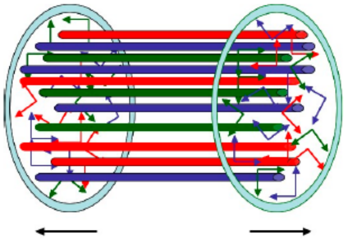

Figure 1.9: An illustration of the production of longitudinal color flux tubes as two CGC sheets collide.

system expands. The fields can be thought of as quanta of gluons when their strength is sufficiently small.

The above described phenomenological framework has many ramifications for observables seen in heavy ion collisions. The decay of the longitudinal fields of the glasma can produce long range 2-particle correlations, similar to that observed at RHIC [11]. One very interesting consequence of the glasma is turbulent instabilities. It turns out that the lowest order solutions for the Yang-Mills equations for the glasma are unstable to turbulent instabilities. This means that a small rapidity dependent perturbation grows rapidly with time and can potentially become larger than the initial glasma field. These instabilities could lead to a fully turbulent system, which can mimic a thermalized system as far as the typical hydrodynamical dynamics is concerned. This means that under a glasma scenario, the QGP need not be thermalized. This needs much more investigation before one can make a solid claim to this, as this is a subject with many unknowns.

Novel sources of direct photon production are expected within the glasma description. This will be discussed in more detail later in the thesis.

1.2.2 Early Time Physics: Strong Magnetic Fields

Some recent theoretical works have begun to focus on the magnetic field produced in heavy ion collisions. Two positively charged ions are moving toward each other in the collisions and so one would expect a magnetic field to be produced based on the motion of the charges alone. Calculations show that this magnetic field can be amazingly large, and can exist throughout the QGP lifetime. This subject is worth investigation, the author of [12] claims that the field affects almost all physics of the QGP. This includes the azimuthally asymmetric production of direct photons with respect to the field direction. First, the strength of the field in heavy ion collisions at RHIC is considered following [12]. For a rough estimate, consider the simple case of two ions of charge Ze and radius R colliding with impact parameter b. The Biot-Savart Law gives the magnetic field, B, due to the stream of ions in Eqn. 1.4.

$$B \sim \gamma Z e \frac{b}{R^3} \tag{1.4}$$

We collide Au ions at an energy of 200 GeV per nucleon in the center of mass frame. This means that Z=79 and R $\approx$ 7fm and the Lorentz factor $\gamma = \sqrt{s_{NN}}/2m_N = 100$. Considering a mid central collision with an impact parameter $b \sim R \approx 7$fm, one can estimate $eB \approx m_\pi^2 \sim 10^{18} G$. This is extremely high. To put it into perspective, the largest man made (pulsed) magnetic field produced is of the order of 10^7 G [13]. Neutron stars typically have magnetic fields on the order of 10^{10} - 10^{12} G and up to 10^{15} G for a magnetar [14]. So producing a magnetic field of 10^{18} G in heavy ion collisions could be the largest field seen in the universe, even if it is produced for an extremely short period of time (on the order of $10 fm/c \approx 10^{-23} s$). This of course is only a very rough order of magnitude estimate and calculations are refined for a more quantitative understanding. Keep in mind that it is already known that classical electrodynamics breaks down and becomes non-linear for fields above the critical Schwinger field strength $F = m_e^2/e \approx 10^{13} G$. Magnetic fields of this magnitude can in principle affect every physical aspect of the QGP. And it is extremely difficult to separate possible magnetic field effects from QGP signatures experimentally, since qualitatively they lead to the same observable effects. Experimentally confirming the presence of these high fields is an important step in understanding the physics of heavy ion collisions.

One can refine the order of magnitude estimate, as is done in [12], by adding the time dependence using the Lienard-Wiechert potentials. For this type of calculation one must know the positions of the nucleons inside of the ions, which can be assumed to follow a Wood-Saxon distribution. The effect of the QGP on the field can also be considered. If the QGP is formed early enough, it may exist while the field is still relatively strong. In the calculations in [12], it is assumed that the QGP is formed at 0.5 fm/c. The electrical conductivity of the QGP is needed for this type of calculation. Not much is known about this quantity, but there are calculations from lattice QCD. The calculation can be refined further, also considering the medium expansion. All of these calculations are shown in Fig. 1.10 from [12], where the strength of the magnetic field at z=0 is shown as a function of time. The different colors show the various refinements made as described above. The blue curve shows the field strength in a vacuum. The red and brown curves show the field in a static conducting medium with two different electrical conductivities, σ, of 5.8MeV and 16 MeV respectively. The green curve further considers the expansion of the medium. As can be seen, the field drops significantly in a vacuum (blue) and is down by more than three orders of magnitude by 3fm/c. The presence of the QGP causes the field to live longer, essentially freezing the field at a particular strength for the lifetime of the QGP. Note that the units in the plot are $\text{fm}^{-2} \approx 2m_\pi^2$.

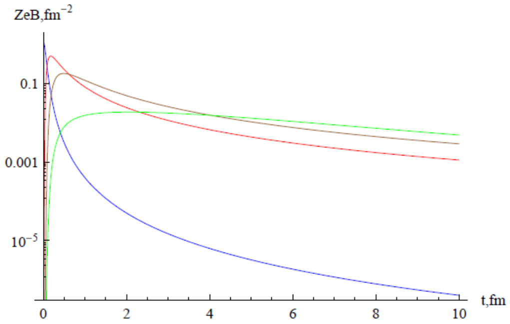

Figure 1.10: The relaxation of the magnetic field in various levels of the calculation from [12]. The colors are described in the text.

1.2.3 v_2 and Elliptic Flow

Before high energy heavy ion collisions took place, it was thought that the QGP produced would be a weakly interacting gas. But this is not the case. It turns out that the QGP produced in the laboratory (specifically at RHIC) is strongly interacting and actually behaves like a fluid. Even further, not only is the QGP a fluid, but it is one of the most perfect fluids known to man (perfect meaning it has a very low viscosity to entropy ratio). Being such a perfect liquid, much of the dynamics imprinted in the bulk particle distributions can be described, with surprising accuracy, with ideal hydrodynamics, i.e. no viscosity [15], [16], [17]. Since the bulk matter of the QGP seems to be a fluid, it flows. The shape of the overlap region is imprinted on the flow the matter exhibits.

The gold nucleus is fairly spherical and so in a collision in which the gold nuclei have near zero impact parameter (central collision), the shape of the overlap region of the collision is almost a circle. But as the impact parameter grows (non-central collision), the overlap region becomes more and more elliptic and is approximately almond shaped. The reaction plane with respect to the impact parameter is defined as shown in Fig. 1.11. The almond shape of non-central collisions will exhibit pressure gradients. The pressure gradients in the reaction plane are larger than that out of plane (or 90° from in the plane

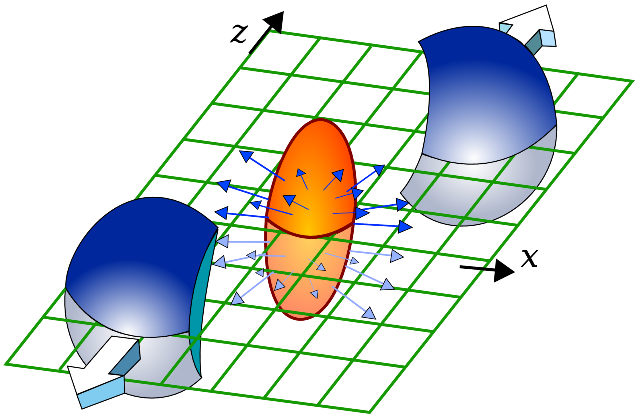

Figure 1.11: The reaction plane of the collision is shown here for a collision in which the overlap region has an almond like shape. This anisotropy results in flow of particles in the direction of the reaction plane. The reaction plane is defined by the direction of the beams, z, and the impact parameter which connects the centers of the colliding nuclei and happens to be along the x direction in this plot.

in the transverse direction), as illustrated in Fig. 1.11. This causes the initial spatial anisotropy of the overlap region to be converted to momentum space anisotropy via the pressure gradients. Further, there will be more particles observed in plane versus out of the reaction plane resulting in some shape to the distribution of particles with respect to the reaction plane ($dN/d(\Delta\phi)$), where $\Delta\phi$ is the angle between the angle of emission of a particle in the plane transverse to the beam direction (azimuth) and angle of the reaction plane.

The $dN/d\Delta\phi$ distributions can be related to how the matter flows and can reveal information about the initial shape and particle distribution of the overlap region. This can be done by performing a Fourier decomposition on the $dN/d\Delta\phi$ distribution, as shown in Eqn. 1.5.

$$dN/d\Delta\phi = \frac{N}{2\pi}\left(1 + \sum_{n}(2v_n cos[n(\phi - \Psi_n)]\right) \tag{1.5}$$

In Eqn. 1.5, v_n is the n^{th} order coefficient to the Fourier decomposition, ϕ is the angle of emission of a particle in the transverse plane perpendicular to the beam, and Ψ_n is the angle of the n^{th} order reaction plane. In principle, each moment of the decomposition has its own reaction plane, which may or may not be correlated with each other, depending on the order [18]. In the context of the bulk matter, v_2 characterizes the so-called elliptic flow and this is something we seek to measure in this thesis. There are other components to the decomposition that are ignored, since they are sub-dominant. Each term takes into account a different type of shape contributing to the flow, see Fig. 1.12. The v_2 is simply a measure of the relative particle emission in plane versus out of plane, but can be related to the dynamics of the collision for bulk particles as explained above. One can also study elliptic flow by studying two-particle correlations by looking at the relative angle between correlated particles [19]. The reaction plane method discussed above is used in this thesis and so two-particle correlations will not be discussed further.

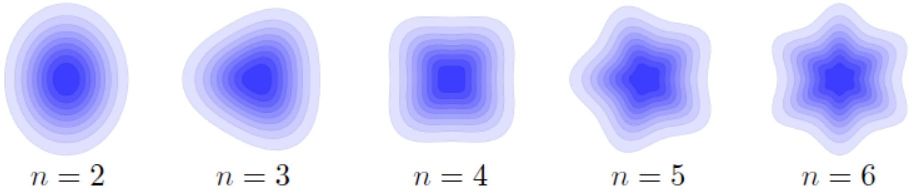

Figure 1.12: The shape of the anisotropy for the 2^{nd} order to 6^{th} order harmonic of the Fourier decomposition.

The study of elliptic flow is very useful in heavy ion collisions. As stated, the elliptic flow is related to the initial spatial anisotropy of the overlap region. Because of this, elliptic flow can be used to study the early dynamics of the collision. Further, the scaling of elliptic flow for different hadron species with the number of constituent quarks is a key piece of evidence in showing that a QGP has been produced [9]. The dynamics of heavy quarks can also be elucidated by studying flow. One of the most surprising results to come out of PHENIX is the observation that the heavy quarks have significant flow as well [20] (calculations done before measurements predicted a smaller flow for heavy quarks compared to light quarks due to a suppression of small angle gluon radiation, the dead cone effect [21] [22]).

Another possible connection of elliptic flow and early collision dynamics concerns the thermalization time. Theory calculations predict that the elliptic flow of thermal photons should be sensitive to the thermalization time [23], [24]. This connection is further discussed in Sec. 1.4. The production mechanisms of direct photons is the focus of the next section.

1.3 Direct Photon Production

Direct photon is a term that distinguishes photons produced by some physics process from photons produced from simple decays from unstable hadrons. As such, direct photons are defined as any photon not from a hadron decay. This still is a blanket term and includes many different processes, which will be detailed here. First, direct photon sources that dominantly contribute at high p_T ($p_T > 4$ GeV) are briefly mentioned, such as hard scattering, Bremsstrahlung, jet conversions, and jet fragmentation. This is followed by a more relevant discussion on sources of low momentum ($p_T < 4$ GeV) direct photons.

Direct photons are a very useful probe of heavy ion collisions because the interaction cross-section with the produced medium is small, since the photons interact electromagnetically and thus production goes as $\alpha = 1/137$ compared to strong interactions with production going as $\alpha_s \approx 0.2$. This is consistent with measurements of the R_{AA} used to quantify medium effects by comparing measured yields in heavy ion collisions to yields from an ensemble of many p+p type collisions. The R_{AA} of direct photons is measured to be consistent with one above $p_T = 4GeV$, indicating production scales as the number of binary collisions [25]. This is in contrast to the measured hadronic $R_{AA} \approx 0.3$ in minimum bias collisions [26], indicating a strong suppression of high p_T hadrons compared to p+p production scaled by the number of binary collisions. The two results are interpreted as illustrating the medium is opaque to hadronic matter, but transparent to electromagnetic probes. And thus photons escape the medium virtually untouched and carry with them information about the environment in which it was produced. Because of this, direct photons can probe the earliest stages of the heavy ion collision and this is the reason they are studied within this thesis.

1.3.1 Direct Photon Production at High Transverse Momentum

One such process that produces direct photons are hard processes in which partons in the colliding nuclei interact and scatter with a large momentum transfer. Processes like gluon Compton scattering and quark-antiquark annihilation contribute to the yield of the high momentum direct photons. See Fig. 1.13 for the diagrams illustrating these leading order processes. These types of processes can be calculated in QCD with perturbative techniques. Direct photons from hard scatterings should also be emitted isotropically over space, thus they have zero v_2.

Bremsstrahlung emitted photons are also considered direct photons. Quarks do carry an electric charge (albeit a fraction of e). As they pass through the medium, they scatter off other charges and emit a photon. If one considers a high p_T quark produced in a hard scattering as described above, then it is conceivable that the parton will emit more Bremsstrahlung radiation in the

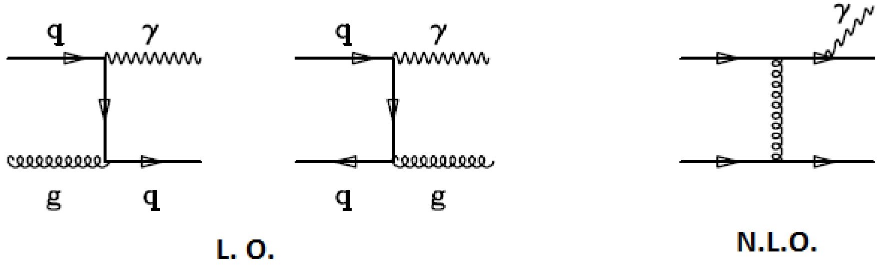

Figure 1.13: Feynman diagrams for direct photon production at high momentum. The diagrams indicate quark-gluon Compton scattering and qq annihilation first order processes on the left and a next to leading order diagram for jet fragmentation photons on the right.

direction where it passes through the most medium (more charges to interact with). Therefore Bremsstrahlung photons should be preferentially emitted out of plane and will have a negative v_2. It is expected that Bremsstrahlung contributes only a small amount to the total direct photon yield.

There are also processes in which a high p_T quark scatters off partons in the medium and converts into a high p_T photon. These are known as jet conversion processes. These processes also exhibit a negative v_2, for the same path-length dependent reason as for Bremsstrahlung photons. The Feynman diagrams for these types of processes can be seen on the left of Fig. 1.14.

High p_T direct photons can also be produced as a jet fragments. Jets are shown to be suppressed by the medium, and so these photons are emitted preferentially in the thinnest direction of the medium. Thus jet fragmentation photons exhibit a positive v_2.

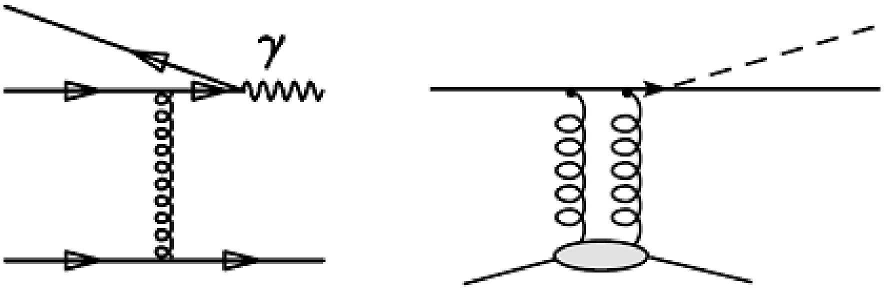

Figure 1.14: Feynman diagrams for the production of direct photons from interaction with the medium.

It should be stressed that for these high p_T direct photon processes, the v_2 measured is not connected to elliptic flow and so is not reflective of the dynamics of the plasma. The v_2 in this case is only reflective of the geometry of the collision, the eccentricity of the overlap region and the opacity of the medium. But for the low momentum thermal photons, discussed below, the v_2 can be interpreted as originating from elliptic flow.

1.3.2 Direct Photon Production at Low Momentum, Thermal Photons

Low momentum direct photons are expected to dominantly originate from thermal radiation from the medium. The term thermal radiation refers to the fact that these particular photons are produced mainly from quark-gluon scattering by partons in the thermalized heat bath of the medium in the QGP phase and $\pi - \pi$ scattering of thermalized pions in the hadron gas phase. The relative yields from each phase is expected to be nearly the same, its not obvious at the current time whether or not the observed shine is dominated by QGP or hadron gas. Naively one would expect that if the medium itself is flowing, then the thermal radiation emitted from this flowing medium should also carry the same v_2 imprint.

1.4 The Thermal Photon Puzzle

PHENIX has recently made measurements on the invariant yield and the v_2 of low momentum direct photons. The invariant yield measurement is discussed in detail in [27] [28]. The invariant yield data from [28] is shown in Fig. 1.15, displaying the yield measured in centrality selections from Au+Au collisions and compared with the p+p result (centrality is defined in Sec. 2.3.1). A fit to the p+p data is done with a modified power law function. No medium is present in p+p collisions and so all direct photons come from hard scattering and jet type processes. Au+Au collisions additionally have contributions from the medium, presumably dominated by thermal radiation at low momentum. Thus the Au+Au data is fit with the sum of the modified power law and an exponential. The fit from the p+p data is scaled by the nuclear overlap function, T_{AA}, for the various centralities for the Au+Au collisions to constrain the shape of the power law to the direct photon yield, while the parameters of the exponential are left to float in the fit. As can be seen in Fig. 1.15, at low momentum (below 3GeV) an excess of yield is seen compared to the extrapolation of the power law fit to low momentum. The shape is consistent with an exponential, and thus seems to be thermal in origin.

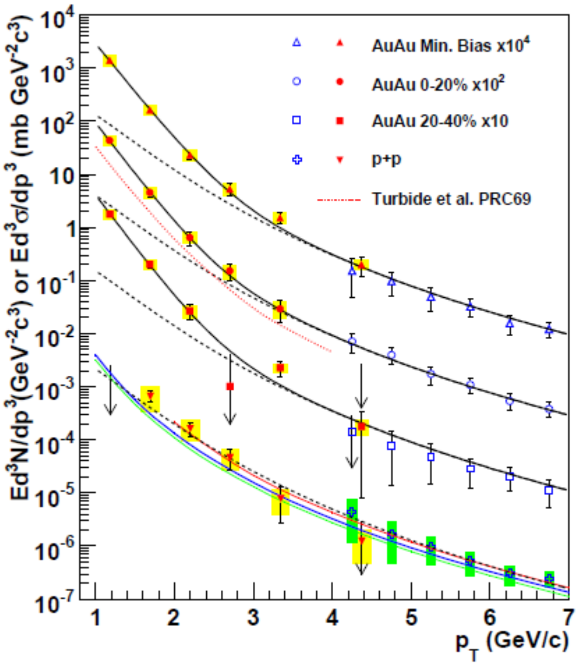

Figure 1.15: The invariant yield of direct photons in Au+Au and p+p collisions. [28]

The yield of thermal photons can be used as a thermometer if we consider the medium as a blackbody radiator. This means that the slope of the thermal spectrum is inversely related to the temperature of the medium. Unfortunately in reality it is not this simple, since the medium is not static, but rapidly expanding. Therefore the photons that we detect are blue-shifted. For a true temperature measurement, model calculations which take Doppler shift into account are needed. Fig. 1.16 shows the direct photon yield compared to various model calculations as detailed in [28]. The various calculations shown do a reasonable job describing the data. These calculations imply that the initial temperature of the medium is in the range of 300-600MeV, with a corresponding thermalization time range of 0.6-0.15fm/c. This range is well above the expected critical temperature of 170MeV for the transition from the hadronic gas to the quark gluon plasma. In these calculations, the production of thermal photons is generally dominated by early time emission, when the medium is the hottest. (Although recently, the meaning of the inverse slope parameter measured from the exponential fits in [27] and the connection to an initially very hot medium may have become obsolete as shown in a revisited hydrodynamics calculation [29]. The current wisdom that most thermal photons are emitted early may be flawed and the large effective temperature extracted from the exponential fit may be due to distortion from radial flow rather than due to a large initial temperature.)

Another recent PHENIX measurement is of the v_2 of direct photons over a large momentum range [30]. The main result from that paper is shown in Fig. 1.17. The left panel of the figure shows the v_2 of neutral pions with two different detectors (covering different pseudo-rapidity ranges) used for the measurement of the reaction plane. The middle panel in the figure shows the inclusive photon v_2. The right panel of the figure shows the v_2 of direct photons. All plots in the figure are for the minimum bias centrality selection. The basic observation is that at low momentum the v_2 is large (of the order of that for hadrons) and at high momentum the v_2 falls and becomes consistent with zero (which is not observed for hadrons). This drop to zero is expected and is interpreted as a signature of hard processes becoming the dominant contribution of direct photons. The statistical and systematic uncertainties do not allow us to see evidence for any other processes that may contribute to a non-zero v_2 at this momentum range as discussed above.

In Fig. 1.18, the result is compared to a theory calculation [23] of the elliptic flow of thermal photons from the QGP and hadron gas. As can be seen, the theory predicts a much smaller v_2 at low momentum. This is the general trend for recent calculations. The calculation for Fig. 1.18 uses hydrodynamics to describe the dynamics of the medium. They put in the most

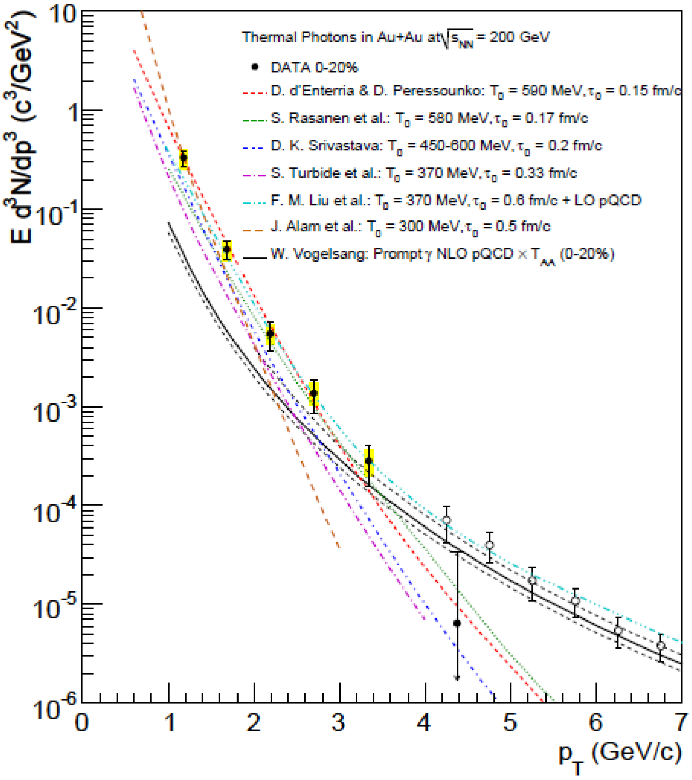

Figure 1.16: The invariant yield of direct photons in 0-20% central Au+Au collisions compared to theory calculations. [28]

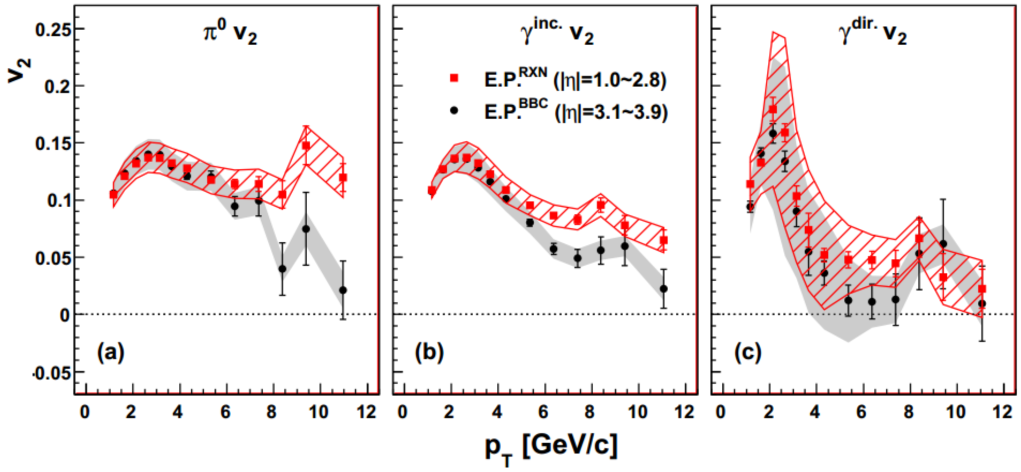

Figure 1.17: The left plot (a) shows the v_2 of the π^0 with two different reaction plane detectors used for reaction plane determination. The middle panel (b) shows the inclusive photon v_2. The rightmost panel (c) shows the direct photon v_2. The results are for the minimum bias centrality selection [30].

recent calculations for thermal rates of photons from the QGP and hadron gas phases. The Cooper-Fry framework is used for the hadronization. This calculation does not include prompt direct photons, which should only serve to make the v_2 smaller. A poor description of the data is observed, with the v_2 significantly underestimated (by about a factor of 2-3) in the calculation below 3 GeV.

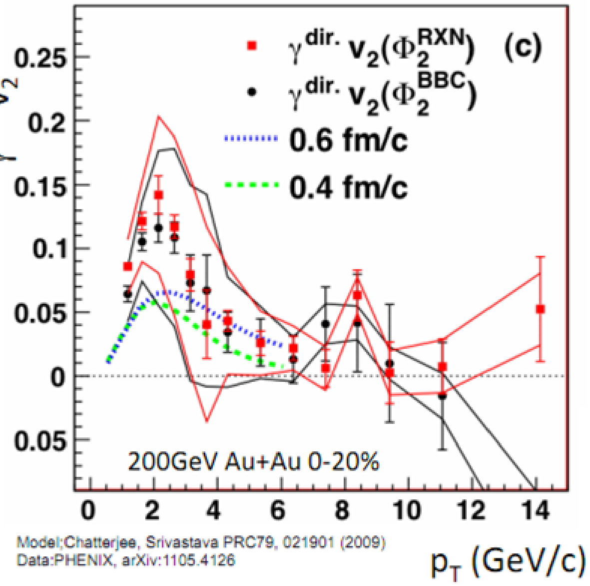

Figure 1.18: The direct photon v_2 from [30] compared to a theory calculation from [23]

The reason current models fail to describe the v_2 at low momentum is simple and has to do with the competition between photon production rates falling and the elliptic flow building up with time. It takes time for the elliptic flow to build up (the v_2 profile in time will look something like Fig. 1.19). So early in the collision, v_2 is small. And in the calculations, most of the photons at low momentum come from early in the collision when the fireball is the hottest. As time passes, the medium cools and the v_2 saturates at its maximum value given the initial geometry. But since the fireball is cooler, there are less thermal photons produced with a large v_2. Thus when an average is taken over the entire collision, the v_2 ends up being small. The relative contributions of the v_2 from the QGP and hadron gas can be seen in Fig. 1.20 [23]. In the figure, the dotted lines represent the v_2 of thermal photons from the QGP phase, the dashed lines represent the v_2 of thermal photons from the hadron gas phase, and the solid lines represent the total observed v_2 averaged over the lifetime of the fireball. The different colors denote different thermalization time assumptions (note the very strong dependence of the observed v_2 with the thermalization time, first mentioned in Sec. 1.2.3). The point being made here is that the v_2 of QGP thermal photons (dotted) is much smaller than that for hadron gas thermal photons (dashed). Note that the hadron gas curves are scaled down by a factor of 2.

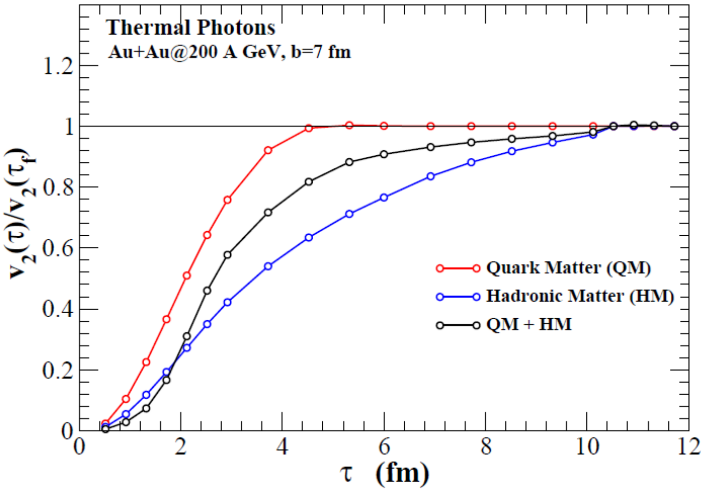

Figure 1.19: A calculation of the profile of the elliptic flow in time, plotted as the ratio at time τ to the final saturated v_2. [31]

These two recent PHENIX results are difficult to reconcile within the basic framework that most calculations utilize. This is the thermal photon puzzle. The large invariant yield excess indicates that thermal photon production dominates early in the collision, but the large v_2 suggests that these thermal photons are mainly emitted late in the collision. These results have generated much interest in the theoretical community and a slew of new ideas and production mechanisms have emerged to explain the data. Two reasonable scenarios can be imagined to solve the puzzle. One scenario is that the direct photon yield observed is actually dominated by thermal radiation, but the radiation mainly comes from late in the collision, giving the large v_2. The other scenarios involve novel sources of production. The two scenarios are discussed further in Chapter 8, where the calculations from these scenarios are confronted with the thesis results. This thesis adds to the existing data on low momentum direct photons in an effort to elucidate possible solutions to the photon puzzle.

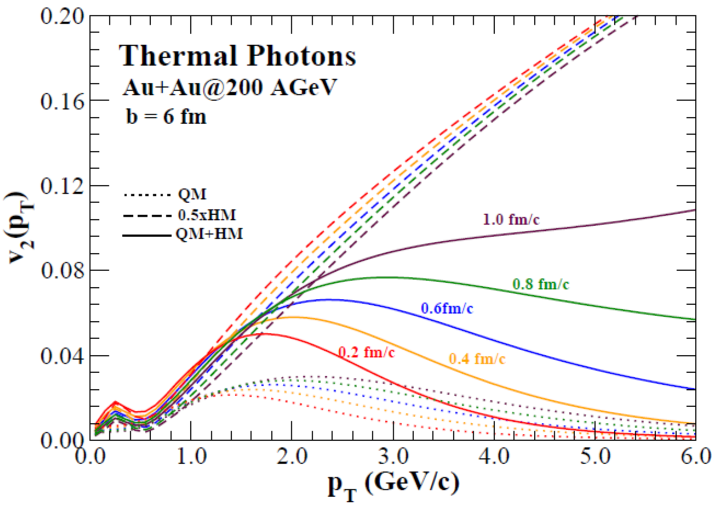

Figure 1.20: A calculation of the thermal photon v_2 from [23]. The dotted curves represent the v_2 of thermal photons emitted from the QGP, dashed curves represent the v_2 of thermal photons emitted from the hadron gas, and solid curves represent the time averaged thermal photon v_2 integrated over the entire evolution of the system. The various colors represent the calculation performed with different thermalization times.

1.5 Purpose of this Dissertation

The purpose of this dissertation is to measure direct photons at low momentum. The measurement will tell us several things. The measurement serves as an important confirmation of the direct photon fraction measurements from the virtual photon analysis [27] [28], which is the main impetus for the undertaking of this analysis. This is not a trivial result, since there are theories that suggest a different direct photon fraction for virtual photons and real photons [32] [33]. The measurement acts as an important confirmation of the virtual photon method in its extrapolation of pairs measured with a mass to zero mass, i.e. $M \times \frac{dN_{ee}}{dM} \to dN_\gamma$ as $M \to 0$.

Secondly, this analysis extends the p_T reach of the measurement compared to [27] from a lower limit of 1GeV to 0.4GeV. The additional data points allow for a better constraint on the spectral shape of the direct photons. Additionally we examine the centrality dependence of the direct photon excess yield in more detail. This will allow for powerful constraints on theoretical models, helping to solve the thermal photon puzzle.

Thirdly, the measurement of the direct photon v_2 with this alternate method via external conversions offers an important cross-check of the published result using the electromagnetic calorimeter [30]. The neutron contamination to the photon signal is substantial at low momentum in [30], where as this contamination is non-existent in the external conversion method.

Chapter 2

The Experiment

This chapter describes the experimental apparatus upon which the measurement is made.

2.1 The RHIC Facility

This section gives a brief description of the RHIC facility located at Brookhaven National Laboratory (BNL) in Upton, NY.

The RHIC (Relativistic Heavy Ion Collider) facility is a collider facility with the ability to collide heavy nuclei as well as proton beams. See Fig. 2.1 for an aerial view. RHIC was built as an upgrade to the previous AGS (Alternate Gradient Synchrotron) rings, which are still used in the process of accelerating the beams to full energy, and was essentially born out of the cancelled ISABELLE project.

The main RHIC rings are 2.4 miles (3.9 km) in circumference. The RHIC accelerator was designed to be a flexible machine, able to collide various species of nuclei (Cu+Cu, Au+Au, d+Au, U+U, Cu+Au) as well as baseline p+p collisions at various beam energies (between 9 and 500 GeV/nucleon center of mass energy depending on the colliding system). Unique to the world colliders is the capability of colliding polarized protons, with the goal of measuring the gluon contribution to the proton spin. This is a separate program and is not discussed further in this thesis. The focus here is on the heavy ion program.

The gold atoms start out their journey to the RHIC rings in the Tandem Van de Graaff accelerators, shown in yellow in Fig. 2.1. Here the atoms are ionized and initially accelerated. They are then sent to the booster synchrotron, shown in light blue in Fig. 2.1. The ions are moving at about 37% the speed of light at the end of their time in the boosters. To accelerate the ions further, they are sent into the AGS rings, the green rings in Fig.2.1. Here they are

Figure 2.1: An aerial photograph of the RHIC facility. The various colors show different facilities that produce the ion beams and bring them up to full energy. The main RHIC rings are the yellow and blue lines as shown.

accelerated to 99.7% the speed of light. Finally the ions are fed into the two main RHIC rings (the blue and yellow rings in the figure), where the ions are brought up to full energy. The ions are traveling in opposite directions in each ring. The beams of ions are delivered in bunches. The beams can circulate inside the RHIC rings for a number of hours (depends on the energy of the beams). In the case of proton-proton collisions, the protons start their journey at the LINAC (LINear ACcelarator) and are then fed into the boosters.

There are six interaction regions around the ring where the beams can cross, four of which are occupied by the RHIC experiments. The four experiments are BRAHMS, PHOBOS, STAR, and PHENIX. The subject of this thesis deals with the PHENIX experiment and detector. The two relatively smaller experiments, BRAHMS and PHOBOS, have completed their data taking, while STAR continues to take data.

2.2 The PHENIX Coordinate System

Before introducing the detector, it is useful discuss the coordinate system used in PHENIX. Fig. 2.2 illustrates the coordinate system used in Cartesian coordinates. The z axis points along the beam line with positive z pointing north. The x axis runs horizontal to the detector with positive x pointing west. The y axis runs vertically. ϕ is defined as the azimuthal angle in the x-y plane. θ is defined as the angle in the y-z plane. The origin of the coordinate system is at the center of the detector.

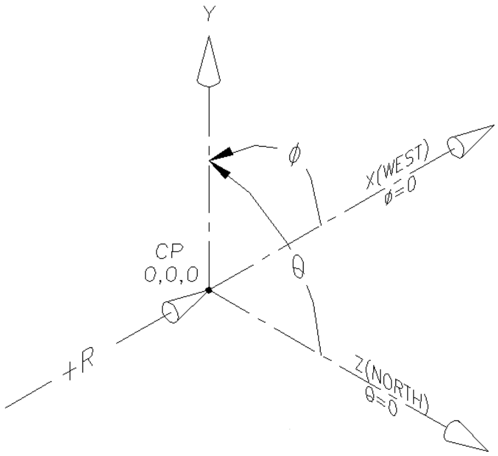

Figure 2.2: A cartoon illustrating the coordinate system used in PHENIX.

It is often convenient to use cylindrical coordinates, where we speak in terms of ϕ and z coordinate along the beam line. Another common coordinate used is psuedorapidity, η, which is related to θ (see Eqn. 2.1). η can also be written as a function of the particle momentum, as shown in Eqn. 2.2. In that equation, p_L is the longitudinal momentum along the z axis.

$$\eta = -\ln\left(\frac{\theta}{2}\right) \tag{2.1}$$

$$\eta = \frac{1}{2}\ln\left(\frac{|\mathbf{p}| + p_L}{|\mathbf{p}| - p_L}\right) \tag{2.2}$$

Fig. 2.3 shows the relation between η and θ in graphical form.

Pseudorapidity is an approximation to rapidity, y. Rapidity is defined in Eqn. 2.3. For relativistic particles, where the mass can be ignored, rapidity becomes equivalent to psuedorapidity.

$$y = \frac{1}{2}\ln\left(\frac{E + p_L}{E - p_L}\right) \tag{2.3}$$

Rapidity and pseudorapidity are useful quantities because the rapidity difference between two particles is invariant under Lorentz boosts along the z axis.

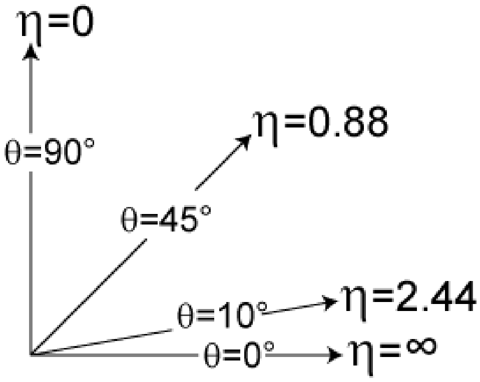

Figure 2.3: A plot illustrating the relation between pseudorapdity, η, and the θ angle relative to the z axis.

2.3 The PHENIX Detector

The PHENIX (Pioneering High Energy Nuclear Interaction eXperiment) detector consists of multiple subsystems designed for different functions. There are global detectors, a charged particle tracking system, and electron and photon id capabilities. The global detectors are used to characterize the geometry of the collision (centrality, reaction plane angle, event vertex). The charged particle tracking system tracks all charged particles through the magnetic field and gives a momentum measurement. Electrons are primarily identified in a RICH detector, while photon identification occurs with an electromagnetic calorimeter. The charged particles studied in this thesis are measured at mid-rapidity in the PHENIX central arms. Each of these groups will be discussed in the following subsections. A cartoon view of the PHENIX detector configuration in 2007 can be seen in Fig. 2.4.

The central arms of the PHENIX detector cover a pseudorapidity range of $|\eta| < 0.35$. The results in this analysis are corrected to one unit of rapidity at mid-rapidity, $-0.5 < \eta < 0.5$. In doing so, we assume that particle production is constant within this rapidity range. As can be seen from Fig. 2.4, the central arms consist of a two arm spectrometer. Each arm covers 90^0 in ϕ and are separated by about 90^0.

2.3.1 Global Detectors

The global detectors all reside in the North and South arms at forward and backward rapidity, see Fig. 2.4.

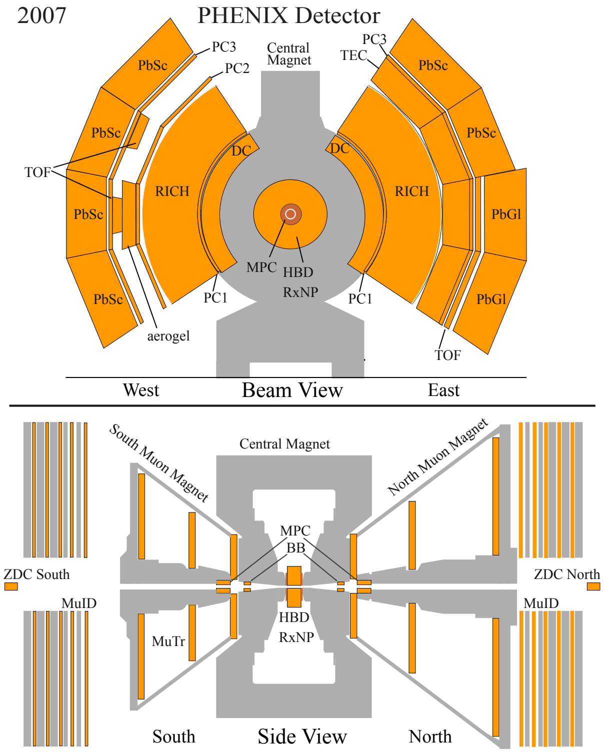

Figure 2.4: The top of the figure shows a cross-sectional view (in the x-y plane) of the PHENIX detector for the 2007 setup, showing the central arms of PHENIX. The bottom of the figure shows a side view, displaying the forward muon arms.

Beam-Beam Counter

Beam-Beam Counters (BBCs) [34] are located down the beam line at 1.44m in both directions for a pseudo-rapidity range of $3.0 < |\eta| < 3.9$. Each detector consists of 64 photomultiplier tubes (PMTs) arranged around the beam pipe for 2π coverage in the transverse plane to the beam. In front of each PMT is $3cm$ of quartz radiator. Particles that pass through the radiator emit Cherenkov light, which is captured by the PMTs. Fig. 2.5 shows the construction of the BBCs.

The BBCs have excellent timing resolution, $54 \pm 4ps$. And so the BBCs set the starting time, T_0, for the entire PHENIX detector.

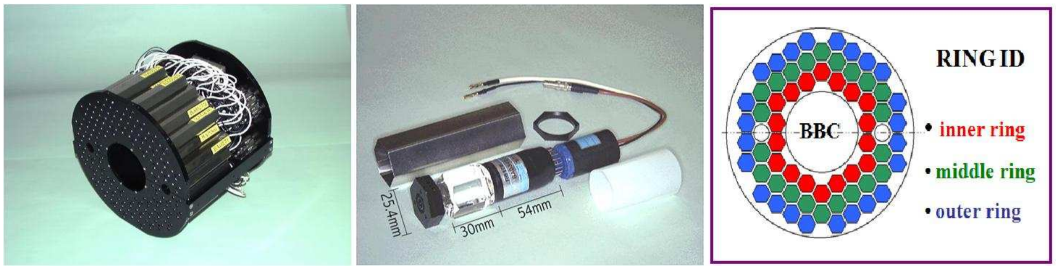

Figure 2.5: The left-most picture shows the assembly of one side of the BBC. The middle photo shows one BBC element. The right-most drawing is a schematic of the PMT configuration around the beam-pipe.

Zero-Degree Calorimeter

The Zero Degree Calorimeters (ZDCs) [34] are hadronic calorimeters installed far down the beam line in both the south and north direction at a distance of 18 meters (pseudo-rapidity about 6). The detectors consist of tungsten inter-laid with optical fibers, connected to PMTs. A schematic of the tungsten modules is shown in Fig. 2.6. Only neutrons are detected in the ZDC since the ZDCs are past the forward dipole magnets, where charge beam remnants are swept away and the yellow and blue lines return to the main rings. The ZDCs are used to measure spectator neutrons thereby assisting in the centrality determination of the event.

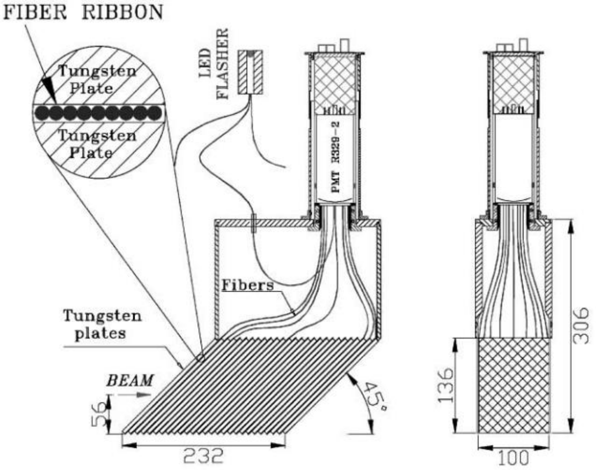

Figure 2.6: A schematic of the tungsten modules of the ZDC. All dimensions are in mm.

Reaction Plane Detector

The Reaction Plane Detector (RXPN) [35] is a dedicated detector installed in Run 7 to determine the reaction plane of an event. It covers a pseudo-rapidity range of $1.0 < |\eta| < 2.8$. The detector is mounted to the face of the central arm magnets. The detector consists of lead scintillator paddles read out by PMTs. Fig. 2.7 shows the RXNP detector installed on the face of the central arm detector.

Figure 2.7: A picture of one of the quadrants of the RXNP detector installed on the face of the central arm magnet. The black pipe near the top of the picture is the beam pipe.

Centrality Definition and Determination

The centrality of a collision is defined as a percent of the total inelastic cross-section. The percentage is defined such that it roughly corresponds to the impact parameter of the collision. As such a 0% centrality collision is a direct, head on collision with an impact parameter of $0fm$. A larger centrality relates to a larger impact parameter. The number of participating nucleons (N_{part}) depends on the impact parameter (and the radius of the colliding nuclei). A very peripheral event will have the gold nuclei barely touch and so there is only a few participating nucleons.

The total multiplicity of particles measured also depends on N_{part}. This can be used to characterize the centrality of an event. The centrality is determined experimentally by measuring the charge sum deposited in the BBCs. Previous years measured the centrality via the correlation of energy deposition in the BBCs and ZDCs. A method using only the BBC was developed for the 2007 data set and beyond. This method hinges on the assumption that the total charge deposited in each BBC is linearly proportional to the number of participants, N_{part}. It has been demonstrated that, under this linearity condition, the charge sum follows a negative binomial distribution, as does the measured particle multiplicity. Fig. 2.8 shows a histogram of the BBC charge sum and the division into centrality bins. The boundaries of n% centrality (x_n) are determined by Eqn. 2.4. In Eqn. 2.4, Q_{all}^{BBC} is the total charge sum in the BBC and A_{eff}^{BBC} is the efficiency of the BBC.

$$x_n = \sum_{i=0}^{n} i \cdot \left(\frac{Q_{all}^{BBC}}{A_{eff}^{BBC}} \right) \tag{2.4}$$

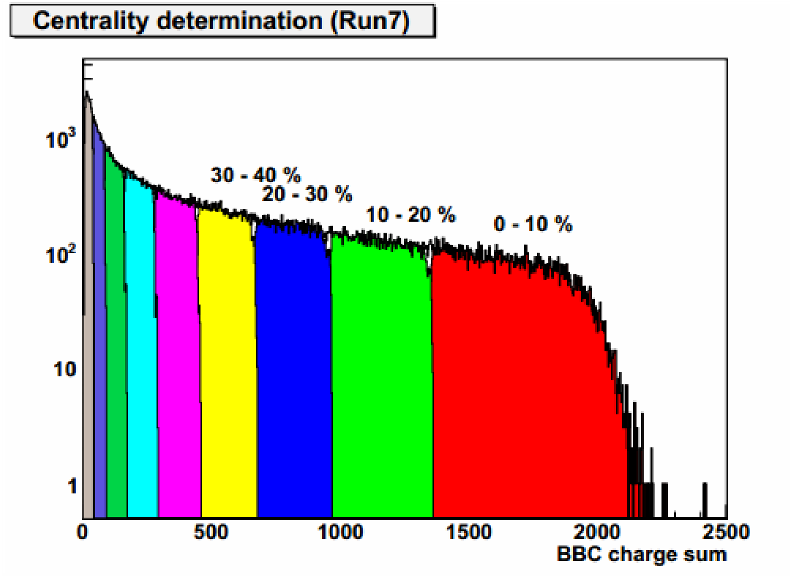

Figure 2.8: A histogram of the BBC charge sum used for the determination of centrality. The division into centrality bins is shown by the colors.

Collision Vertex Determination

The event vertex of a collision in the z-direction (along the beam axis) is determined using the BBCs. The timing difference between particles hitting the north and south detector determines the z-vertex, see Eqn. 2.5. In the equation, c is the speed of light and $t_S(t_N)$ is the time at which the south(north)

BBC fired.

$$z_{vertex} = c \cdot (t_S - t_N)/2 \tag{2.5}$$

With the excellent timing resolution of the BBCs, a z-vertex resolution of a few centimeters is achieved. The z-vertex of a collision is an important piece of information. The spread of collisions delivered to us by RHIC is not narrow in z. Ideally one would want the collision to occur in the very center of the PHENIX detector. For most analyses a cut of $\pm 30cm$ is placed on the events. For the analysis discussed in this thesis, a tighter cut of $\pm 10cm$ is made. The reason will be explained in detail in Sec. 3.1.

Reaction Plane Determination

The reaction plane of an event is defined from the impact parameter of the nuclei and the beam direction, see Fig. 1.11. This can be measured experimentally from the anisotropy of the particle distribution of forward going particles. As discussed in Sec. 1.2.3, the particle distribution can be Fourier decomposed. Each harmonic of the distribution has its own plane in which it is oriented. These planes may or may not be correlated to each other depending on the order. In general for the nth harmonic, the event plane is defined as

$$\Psi_n = \frac{1}{n} \tan^{-1}\left(\frac{Y_n}{X_n}\right) \tag{2.6}$$

where

$$Y_n = \sum_i \sin(n\phi_i), X_n = \sum_i \cos(n\phi_i) \tag{2.7}$$

and the sum is over i particles. The 'n' in Eqn. 2.7 refers to the n^{th} order harmonic and ϕ is the angle of emission of a particle in the plane transverse to the beam. The reaction plane referred to by this analysis is the second order (n = 2) event plane.

2.3.2 Charged Particle Tracking System

Central Arm Magnets

A magnetic field is required in order to measure the momentum of charged particles. This is achieved for the central arm tracking by the central arm magnets [36]. There are also north and south muon magnets, but they are not relevant for this particular analysis and will not be discussed further. The magnet is an axial field magnet, consisting of two pairs of concentric coils. These coils can be run separately, allowing them to be run together (++ field) or in an opposite configuration (+- field). For the dataset analyzed in this thesis, the +- field configuration was used. This is because it was desired to have zero (or as little as possible) field in the region of the HBD (see the HBD subsection later in this section) to have straight tracks for the tracking. Even in the ++ field configuration, the magnets are designed so that the field strength is minimal where the tracking detectors reside. This is because straight tracks through the detectors are the easiest to observe and reliably track in a high multiplicity environment with the wire chambers used in PHENIX. The field integral at full strength is 0.78 Tesla-meters. The magnets are very large, standing 9 meters tall and weigh almost 500 tons.

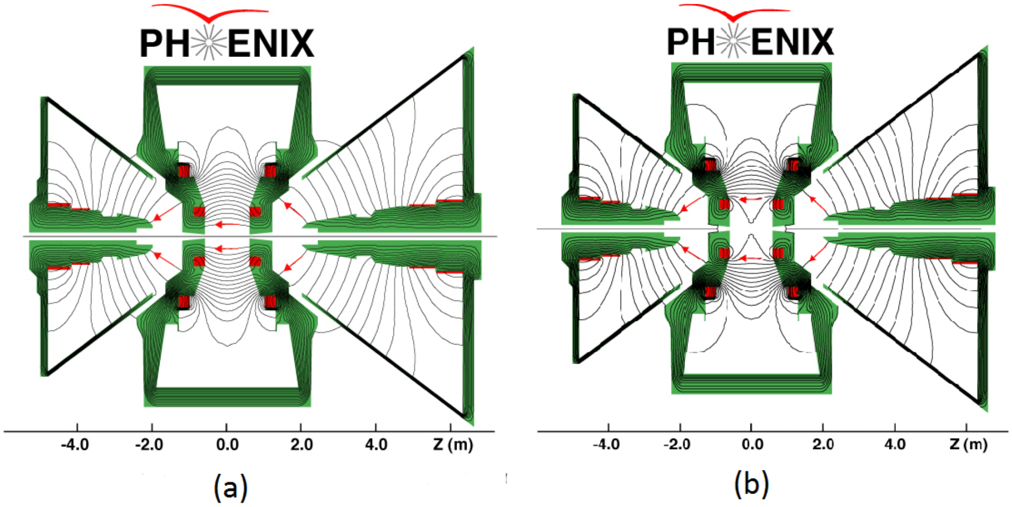

Figure 2.9: Magnetic field calculations from a Garfield simulation for a) the ++ configuration and b) the +- configuration.

Fig. 2.9 shows the field lines in each field configuration from a Garfield simulation.

The Drift Chamber

The drift chamber [37] is the main tracking detector for PHENIX. It sits at a radial distance of 2.02m to 2.46m from the interaction point. It is 1.8m long in the z direction and each arm covers 90^0 in azimuthal angle, ϕ. The drift chamber assists in determining the quality of track candidates, as well as determining the azimuthal angle, charge sign, transverse momentum and allows for pointing of a charged track to various subsystems. The basic construction of the frame is shown in Fig. 2.10.

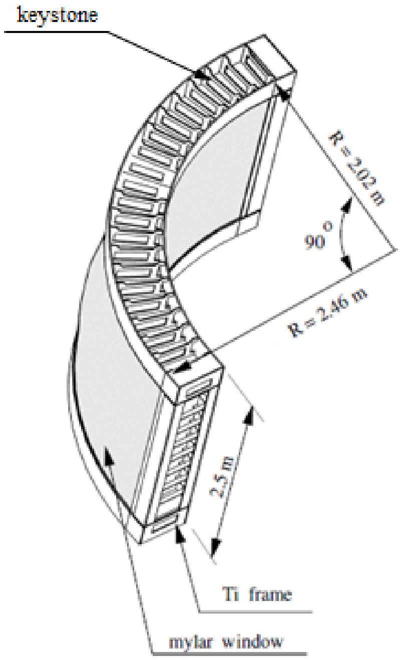

Figure 2.10: A schematic of the frame of one arm of the drift chamber. The dimensions are also given.

Each drift chamber is composed of 20 identical keystones (seen in Fig. 2.10). Each keystone has six radial layers of wire nets, labeled the X1, X2, U1, U2, V1, V2. This can be seen in Figs. 2.11 and 2.12.

The drift chamber is a multiwire chamber filled with a 50-50 mixture of Argon and Ethane gas, specifically chosen for stability of the drift velocity over small variations of the electric field strength around where the detector is operated (approximately 1 kV/cm, resulting in a drift velocity on the order of 50μm/ns). The drift chamber tracks charged particles by measuring the ionization from the track passing through the gas inside the detector. A static electric field is applied in the detector. Thus there will be two clouds of ionization charges drifting in opposite directions from the field. The drift chamber uses the ionization electrons as the signal since they have a larger drift velocity. A gain on the order of 10^4 is obtained, given the gas mixture and field set inside the chambers. The time it takes for ionizing particles to produce a signal is measured. The distance of the origin of the ionization

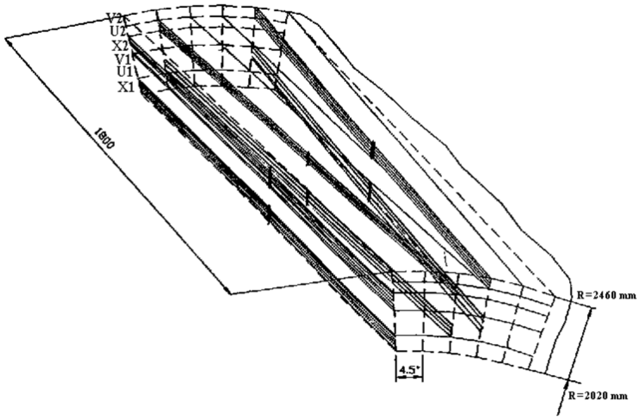

Figure 2.11: The layered wire net layout of a keystone.

signal to the sense wire can then be calculated from this time and the known drift velocity. This is how hits in position space are measured. Tracks can then be reconstructed from these hits.

The wire nets introduced above are made up of many different wires with different functions. The layout of a single wire net inside of a keystone (or sector) is shown in Fig. 2.12. The keystone can be split up into planes, as indicated on the left side of Fig. 2.12. The planes alternate as anode (dashed lines) and cathode (dotted lines) planes. The cathode planes consist of cathode wires, which create the electric field with the anode wires. The anode plane is a little more complicated, having 5 different types of wires (shown in the zoom-in insert in the figure). There are termination wires at the edge of the net to keep the field uniform and reduce boundary effects. Gate wires limit the drift region width, and potential wires help to separate the region between wires and control gas gain. There are also back wires that block signal from one side of the wire, eliminating the left-right ambiguity of the track reconstruction (since you only know a drift distance, not a direction of drift). Finally there are sense (anode) wires, to which the signal drifts. In this configuration, the drift region between wires is 3mm.

There are some differences between the X and the U/V wire nets. For one there are 12 anode wires in the X layers, but only 4 in each of the U and V layers. Another difference is that the U and V layer wires are tilted at an angle compared to the X wires, as illustrated on the right of Fig. 2.12. This allows us to see in stereo and glean some tracking information in z.

The drift chamber described above has a single wire efficiency on the order of $90 - 95\%$.

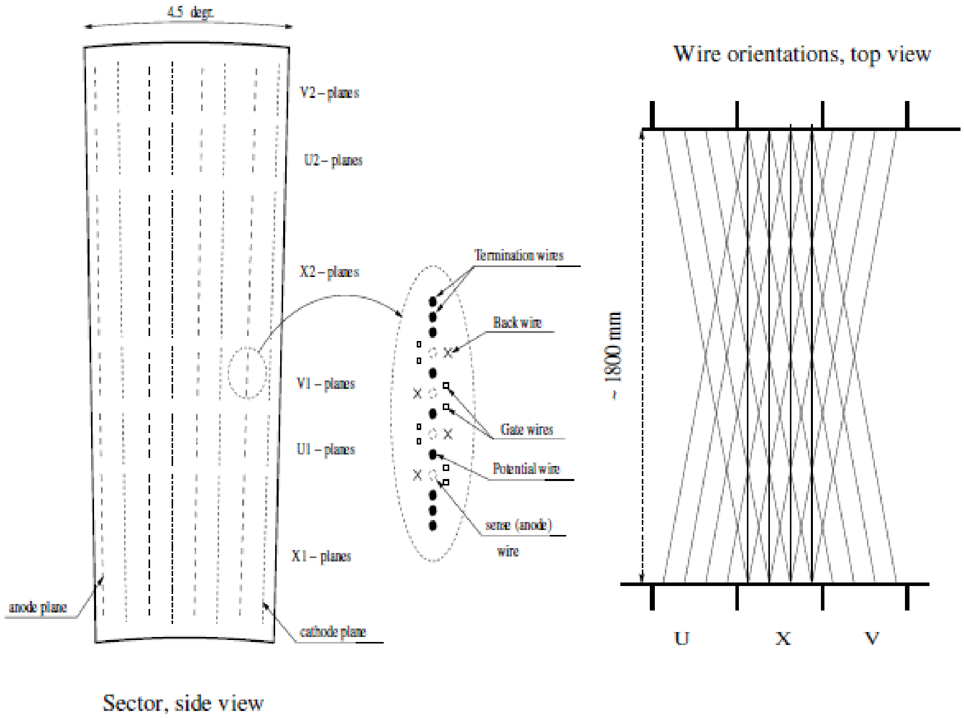

Figure 2.12: The wire layout of a keystone. The X1, X2, U1, U2, V1, V2 planes are indicated in the side view of the keystone on the left. The dashed lines represent the anode plane and the dotted lines represent the cathode plane. A zoom in of single anode plane wire net is shown in the center of the figure. The right side of the figure shows the orientation of the wire layers from the top view.

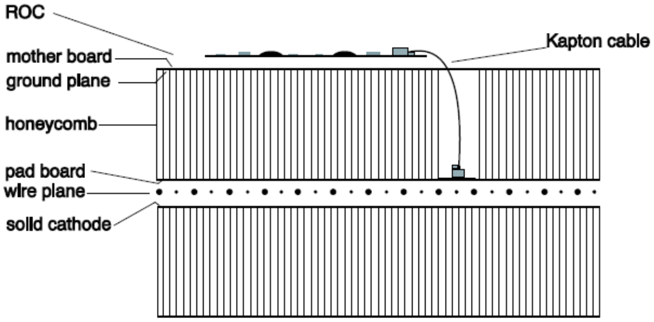

Figure 2.13: A view of a vertical cut through the pad chamber

Pad Chamber

The Pad Chambers, PC, [37] [38] [39] are essential to accurate particle tracking in PHENIX. The PCs allow for additional track quality constraints and determines the z-position of a track. They also allow for charged hadron rejection for various analysis with the Emcal and the RICH. There are three layers of PCs. PC1 resides right after the drift chamber. PC2 is located immediately after the RICH detector (in the west arm only). PC3 is directly in front of the Emcal, see Fig. 2.4.

The basic construction of the pad chamber can be seen in Fig 2.13. The pad chambers consist of a single plane of anode and field wires in a gas volume, surrounded from above and below by cathode planes. The bottom cathode is made of solid copper. The top cathode plane is a bit more complicated, as it is segmented into pixels for the pad readout. The signals from the pixels are transmitted and amplified and discriminated outside of the gas volume by the Read Out Cards (ROCs).

Reconstruction of Charged Tracks in the Central Arms

Fig. 2.14 shows a diagram of a track going through the central arms. The track bends in the magnetic field until the field stops at the start of the tracking systems. Each track is assumed to have come from the event vertex. The figure also illustrates several important coordinates used to define the direction of a track. They are the following:

- ϕ: The azimuthal angle of the intersection point of the track with a reference circle of 220cm.

- ϕ_0: The azimuthal angle of a track at the vertex, determined by tracing the particle back through the field.

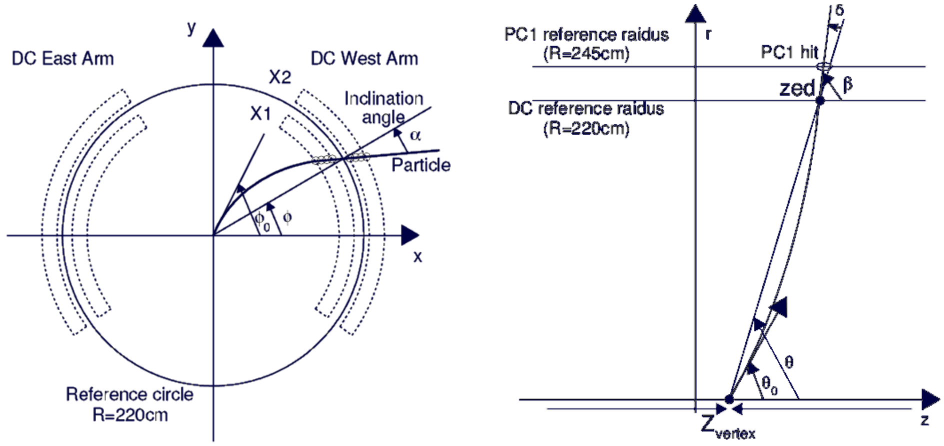

Figure 2.14: A diagram illustrating a track passing through the central arms and the relevant coordinates of the track. The left image shows the track in the x-y plane. The boxes labeled X1 and X2 represent the X1 and X2 layers of the drift chamber. The right image shows a track in the r-z plane.

- α: The angle between the track projection and a straight line track going through the same intersection point at the reference circle in the x-y plane. The magnitude is proportional to the momentum and the sign proportional to the charge of the particle.
- θ: The polar angle of a straight line track through the track intersection point at the 220cm reference circle.
- θ_0: The polar angle of the track at the vertex.
- zed: The z coordinate of the track projection to the 220cm reference circle.
- β: The inclination angle of the track to the z axis at the intersection point.
- δ: The angle between the track projection and the straight line track going through the same intersection point in the r-z plane.

The pattern recognition to associate hits with tracks utilizes a combinatorial Hough transform. Pairs of hits from the X1 and X2 layers are formed and mapped to the 2D space of ϕ and α, as defined above. Particles move straight through the drift chamber, as they reside in a field free region, and so all hit pairs of a given track will have the same ϕ and α. Local maxima are observed when hit pairs are histogramed in the space, see Fig. 2.15. The pairs forming the local maxima are the hits within a track and are associated with the initial track candidate. An iterative track fitting procedure is performed to associate hits with tracks. Once a hit is associated with a track, it is removed from the list of hits and will no longer contribute to another track.

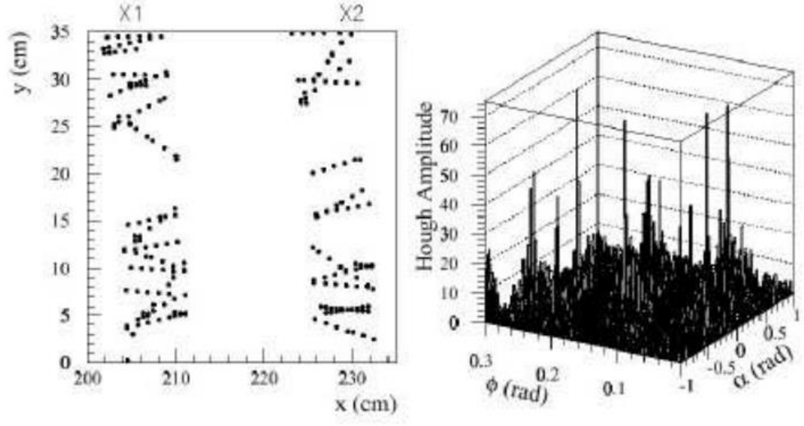

Figure 2.15: Left: A plot showing hits from a simulation of a central Au+Au collision in a region of the drift chamber. Right: A plot showing an example of the 2D space used for the Hough transform for the pattern recognition. The local maxima represent the tracks.

The UV layers of the DC and PC1 is used to constrain the track in the r-z plane for full 3D track reconstruction. First the straight line track in the r-ϕ plane is extended to PC1. If an unambiguous PC1 hit association can be made within 2cm of the track projection, then the track in the r-z plane is fixed by the BBC vertex and the PC1 hit in z. Additionally an unambiguous hit in the UV layer of the DC is also searched for in a window of 5cm around the track projection. Tracks with this additional constraint are considered of higher track quality.

The track quality for each track is implemented through a 6-bit variable, Q_{track}. It is defined in the equation below:

$$Q_{track} = A \times 2^0 + B \times 2^1 + C \times 2^2 + D \times 2^3 + E \times 2^4 + F \times 2^5 \tag{2.8}$$

A, B, C, D, E, and F in the above equation are quality bits and are either 1 for passing a condition or 0 otherwise. The conditions are as follows:

- A: the X1 plane is used
- B: the X2 plane is used
- C: there are hits in the UV plane
- D: there are unique hits in the UV plane
- E: there are hits in PC1
- F: there are unique hits in PC1

Note that both A and B are never simultaneously 0 since every track is required to have at least 8 X1 and X2 hits. In this analysis, tracks of quality 63, 51, or 31 are analyzed. 63 is the highest quality and means the track was reconstructed with hits in the X1 and X2 planes and also have a unique hit in both PC1 and the UV plane. A quality of 31 requires that the track has a unique UV hit and an unambiguous hit in PC1, along with the required X1 and X2 hits. A quality of 51 requires a unique PC1 hit, but no associated UV hit with the X1 and X2 hits. [40]

Momentum Determination

The bend angle α is proportional to the transverse momentum, p_T, of a track:

$$\alpha \approx \frac{K}{p_T} \tag{2.9}$$

In the above equation, K is related to the magnetic field integral along the trajectory of the particle. In principle one can use Eqn. 2.9 to calculate p_T, if one accurately knows K. But the magnetic field at PHENIX is complicated and an analytic parameterization of the track trajectory through the field is not possible. Thus we implement a non-linear grid interpolation technique [40]. The grid provides the field integral $f(p, r, \theta_0, z)$ as a function of the total track momentum (p), the radius (r) from the vertex, the polar angle (θ_0) of the track and the z coordinate of the collision vertex (z). The grid is generated by propagating particles through the magnetic field map and numerically integrating f for each grid point. The field integral varies linearly with ϕ for a given r. ϕ is given by the original angle of emission, ϕ_0, plus the kick due to the magnetic field. This is shown in Eqn. 2.10.

$$\phi = \phi_0 + q\frac{f(p, r, \theta_0, z)}{p} \tag{2.10}$$

The field integral $f(p, r, \theta_0, z)$ is extracted from the grid for each hit associated to the track through the use of look-up tables. Then a fit in ϕ vs. f is performed and the quantities ϕ_0 and q/p for the track are extracted. Then the extracted p and ϕ_0 values are fed back into Eqn. 2.10 in an iterative procedure. A similar procedure is performed in the r-z plane to find the θ_0 angle.

The momentum resolution for reconstructed charged tracks with momenta above 200 MeV/c is given by:

$$\frac{\sigma_p}{p} = 0.7\% \oplus 1\% p(GeV/c) \tag{2.11}$$

In Eqn. 2.11, the first term is due to multiple scattering and the second is due to the intrinsic drift chamber resolution, determined mainly by the number of hit points and the spacing between wires. [40]

2.3.3 Electron ID Detectors

Ring Imaging Cherenkov Detector

The Ring Imaging Cherenkov detector, RICH, [41] is the main detector used for electron identification. It consists of a chamber filled with radiator gas. Electrons that pass through the gas emit Cherenkov radiation that can be detected by PMTs. The detector is designed to perform its physics goals while making the detector as light as possible, keeping electrons and positrons from photon conversions to a minimum, achieved by placing the PMTs outside of the detector volume. A cutaway of the RICH is shown in Fig. 2.16.

Each chamber has a gas volume of $40m^3$. The entrance window has an area of $8.9m^2$, and the exit window has an area of $21.6m^2$. Each detector consists of 48 composite mirror panels. The panels form two intersecting spherical planes, resulting in a total reflecting area of $20m^2$. The mirrors focus the Cherenkov light onto two arrays of 1280 Hamamatsu H3171S UV photomultiplier tubes. Particles passing through the detector see a minimum thickness of gas of 87cm and a maximum of about 150cm. The gas used is CO_2.

One of the key necessary features of the detector is that it must be able to distinguish between electrons and charged pions. Pions start to radiate inside the gas at 4.65 GeV/c. On average, electrons moving at the speed of light will radiate about 12 photons per ring for a 1.2 m path length. The ring diameter is about 11.8 cm (remember the Cherenkov angle, θ, is given by $\cos\theta = \frac{1}{n\beta}$, with n the index of refraction of the gas and β the fraction of the velocity of

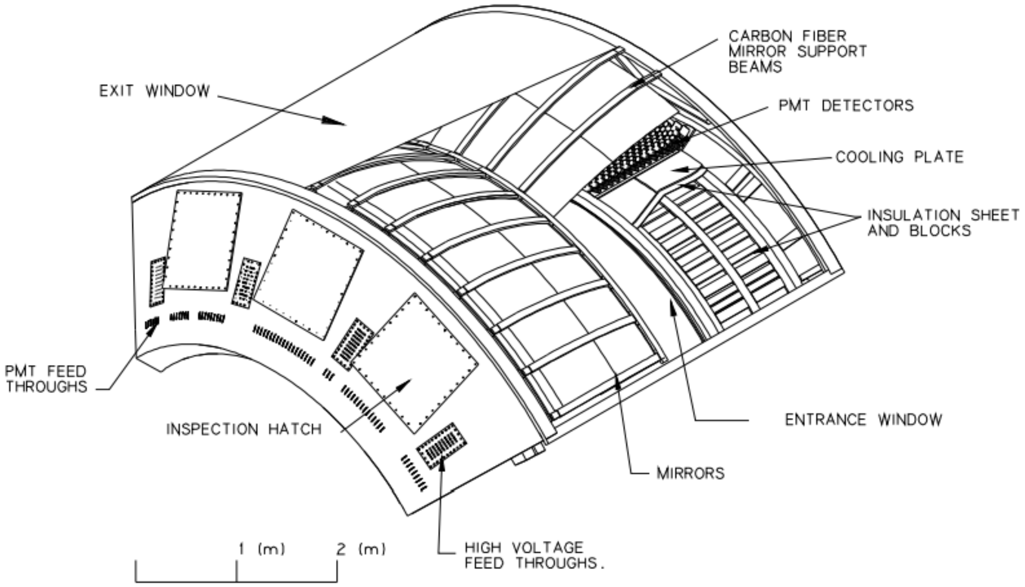

Figure 2.16: A schematic of the construction of the RICH detector.

light the particle carries).

Charged tracks found using the tracking system are associated with hit PMTs in the RICH during the reconstruction process. The track is projected to the RICH PMT plane. Then hit PMTs are found that are around the track projection. The number of hits found is quantified by the n_0 variable. n_0 is defined as the number of hit PMTs within a ring around the track projection with an inner radius of 3.4cm and an outer radius of 8.4cm. This search ring is chosen based on the known ring diameter and the position resolution of the PMTs, defined by the PMT size (about 2.5cm).

Hadron Blind Detector

The Hadron Blind Detector (HB [42] operates as a Cherenkov detector. CF_4 is used for the radiating gas inside the 50 cm long cavity. The readout consists of a triple GEM stack, with a CsI photocathode on the top layer and a pad readout on the bottom layer. The HBD sits in the central arms of PHENIX. It is installed just after the beam pipe at radius of about 5 cm and extends to a radius of about 60 cm. It is 65.5 cm in length along the beam axis. The HBD has an acceptance of 135° in ϕ and a pseudo-rapidity coverage of $|\eta| < 0.45$. Fig. 2.17 shows the construction of the HBD.

2007 is the first run that the HBD was installed. This is an engineering run, in which the detector did not function as planned. The west half of the HBD had to be removed mid-run because of malfunctioning, leaving just the east half for the rest of the Run (but this is exploited within this analysis and offers some cross-check of the photon identification outlined in Sec. 3). This analysis uses the HBD strictly as a converter and the focus is on conversions that occur in the backplane of the HBD, which has a conversion length of about 2-3%. The detailed discussion of the detector is left to the reference [42] since the detector was not used in the analysis (other than as a converter).

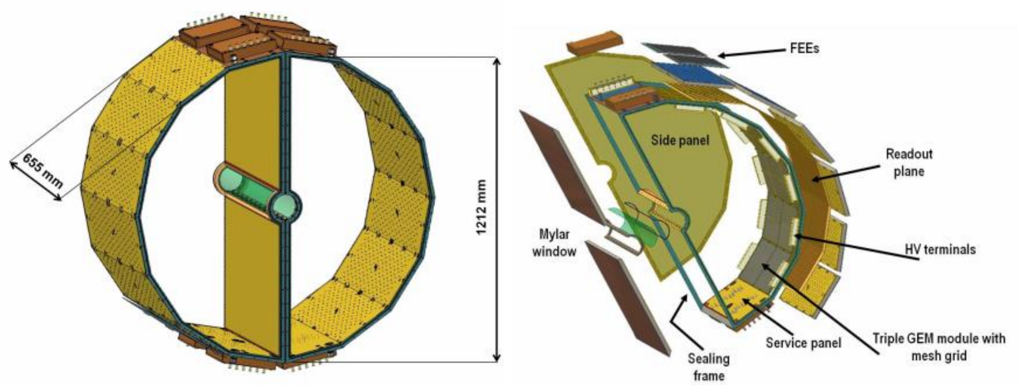

Figure 2.17: A diagram of the HBD assembly. The left panel shows both halves installed around the beam pipe. The right panel shows the construction of one side of the HBD.

2.3.4 Electromagnetic Calorimeter

The subsystem at the greatest radial distance from the interaction point within the central arms is the electromagnetic calorimeter, EMCal [43] (at a radius of about 5m). The EMCal is designed to measure the position and energy of photons and electrons. The mechanical design of the EMCal is described first.

The EMCal is split up into eight sectors, with four sectors in each arm. The east arm has two different types of calorimeters, lead glass (PbGl) and lead scintillator (PbSc). Both types have slightly different efficiencies and tower segmentation. This allows for a comparison of EMCal measurements with two distinct types of calorimeters. Both types of sectors have good energy and position resolution, but each have their own strengths and weaknesses in their design. The main strength of the PbSc sectors is the timing and linearity of response to charged particles. The main strength of the PbGl sectors is the energy resolution and a finer granularity.

Lead-Scintillator (PbSc) Sectors

The PbSc sectors are installed fully in the West arm and in the two top sectors of the East arm. The basic construction of this sampling calorimeter starts with one tower. A tower consists of 66 sampling cells of alternating tiles of lead and scintillator. The cells are optically connected by 36 wavelength shifting fibers read out to 30mm FEU115M phototubes attached to the back of the towers for light collection. These fibers penetrate longitudinally into the tower. There are 15,552 of these individual towers in the detector covering about $48m^2$ in area. A module is built of four of these towers. Each tower in a module is optically isolated. Fig. 2.18 shows a diagram of a single module. 36 of these modules are then bound together to form a rigid structure called a supermodule. Eighteen supermodules form a single sector, held together in its own rigid 2 x 4 m^2 steel frame. A monitoring system is implemented for calibration and gain monitoring of each tower and involves a laser depositing known pulses of energy into the towers.

The nominal energy resolution of the PbSc calorimeter is $8.1\%/\sqrt{E}(GeV) \oplus 2.1\%$ with an instrinsic timing resolution better than 200 ps for electromagnetic showers. The stochastic term of value 8.1% is due to the sampling of the showers and is very close to that determined from GEANT simulations. The constant term of value 2.1% is dominated by intrinsic nonuniformities due to tower boundaries, hot spots at fiber positions, and fluctuations in the shower depth.

The position resolution is given by

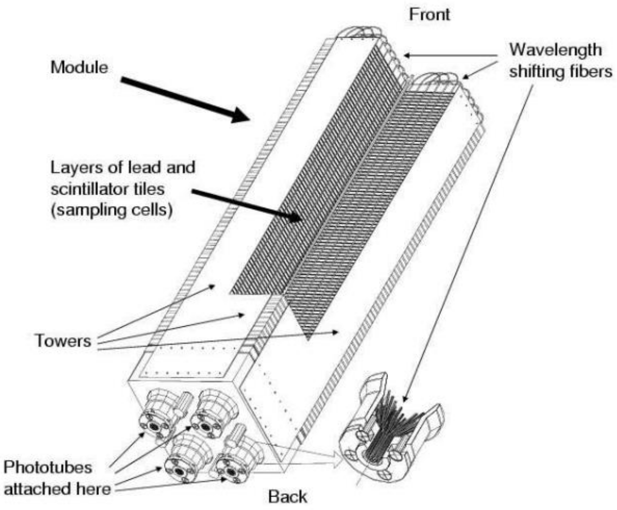

Figure 2.18: A diagram showing the construction of a PbSc module.

$$\sigma_x(E,\theta) = \sigma_0(E) \oplus \Delta \times sin(\theta) \tag{2.12}$$

with $\sigma_0(E) = 1.55 \oplus \frac{5.7}{\sqrt{E}}(mm)$ as the position resolution for a normal incidence angle (θ). E is in units of GeV and Δ is approximately the radiation length.

Lead-Glass (PbGl) Sectors

The lead glass (PbGl) calorimeter is installed as the two lower sectors in the East arm. In contrast the the sampling PbSc detector, the PbGl is a Cherenkov detector. The PbGl sectors are also built up from the module/supermodule structure. Each PbGl sector is made from 192 supermodules, in a formation of 16 X 24, see Fig. 2.19. Each supermodule is built from 24 modules and is 6 x 4 modules in length and width. A single module is 40mm x 40mm x 400mm in size. There are a total of 9216 PbGl elements in the detector. Each module is read out with an FEU-84 photomultiplier.

A calibration and monitoring system comprising of LEDs is utilized. Each supermodule is equipped with its own set of LEDs as shown in Fig. 2.19. All 24 modules in the supermodule see the light from the LEDs.

The nominal energy resolution of the PbGl calorimeter is $6\%/\sqrt{E}(GeV)$ with an intrisic timing resolution better than 300 ps for electromagnetic showers that are above the MIP energy. The measured position resolution can be described by

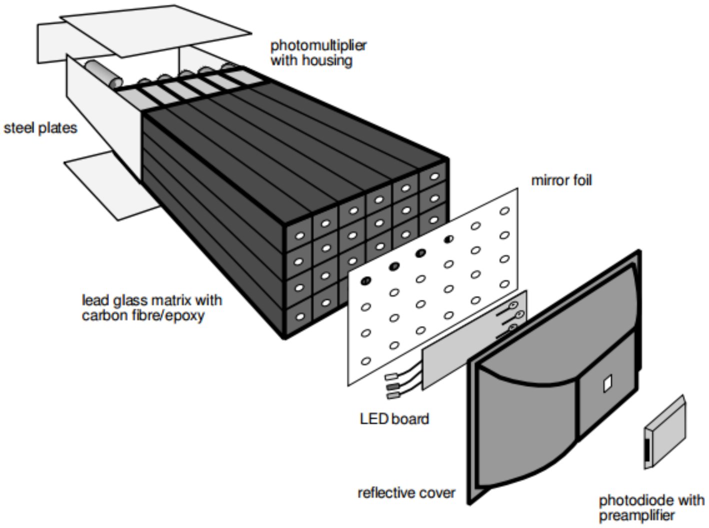

Figure 2.19: A diagram illustrating the construction of a PbGl supermodule.

$$\sigma_x(E) = \frac{8.4mm}{\sqrt{E(GeV)}} \oplus 0.2mm \tag{2.13}$$

Clustering Algorithm

An incoming particle typically deposits its energy in more than one tower. Thus electromagnetic showers are reconstructed as clusters in the calorimeter [40]. The clustering algorithm needs to accommodate the high multiplicity environment in a Au+Au collision. The algorithm starts by applying a minimum threshold of 10MeV on each tower to reduce noise. Adjacent towers passing this minimum energy requirement are grouped into isolated clusters. Next a local maximum is found within each cluster. The total energy within a 3x3 region of towers (electromagnetic showers are typically contained in an area of 3x3 towers) around the cluster must be above 80MeV to be further considered. Energy deposited within a region of 5x5 around the local maxima is considered to be the peak area. If a tower is shared by one or more local maxima, then the tower energy is split according to the shower profile determined from GEANT simulations and beam tests. This allows the peak areas to be split up according to what is expected from the physics of the electromagnetic interaction with the detector. The cluster is further refined by redefining the cluster area as a core cluster, which includes only towers that satisfy the threshold condition $E_i^{pred} > 0.02E_{total}^{meas}$. In the threshold condition,

E_i^{pred} is the predicted energy deposited from the shower shape profile in the i^{th} tower and E_{total}^{meas} is the total energy in the peak area. The core energy is then determined by the sum energy of the towers meeting these conditions. A further correction due to incident angle dependent energy loss is applied and determined from Monte Carlo simulations.

The hit position of the cluster is determined from the center of gravity of the amplitudes of each tower in the cluster. The true position of impact is actually not the same as the center of gravity, due to the fact that the shower profile can be deformed depending on the incident angle. The mapping of the center of gravity to the true hit position as a function of incident angle is determined from beam tests and is used to get the corrected hit position. [40]

2.3.5 Data Acquisition System (DAQ)

The PHENIX detector is designed to take data at a very high rate. Essential to high rate data collection is a fast Data Acquisition System (DAQ). The RHIC machine delivers Au+Au interactions at a rate of about 10kHz, with a high multiplicity Au+Au event taking up about 200kB of space. The DAQ is designed to accommodate this high rate of input, with a data archiving rate of over 400 MB/s, and high level triggers (see Sec. 2.3.6). The DAQ is also designed to be able to accommodate future increases in the delivered luminosity of the beams.

The DAQ is able to handle high interaction rates by employing a system that is parallel, pipelined, and buffered. Each DAQ component is able to take in, process and read out data in parallel. The DAQ system is built around the concept of granule and partition. A granule is the smallest component of the DAQ and consists of the timing control and data acquisition for each subsystem. A partition is a collection of granules. The granules within a partition share busy and accept signals. A block diagram of the DAQ is shown in Fig. 2.20.

The Master Timing Module (MTM), Granule Timing Module (GTM) and Global Level-1 Triggering system (GL1) are the controllers of the DAQ. The MTM receives the 9.4MHz clock from RHIC and passes it to the GTM and GL1. The GTM then delivers the clock, control commands, and event accept signals to the Front End Module (FEM) of each subsystem. The FEM of each subsystem digitizes the analog response of the detector. The GTM can fine tune the clock in steps of $\sim 50ps$ to accommodate the timing differences between the FEMs. The GL1 combines LVL1 signals from various detectors to produce the first LVL1 trigger decision. The LVL1 decision generation of whether or not to take an event takes about 30 bunch crossings. In the meantime, analog event data are stored in switched capacitor arrays called

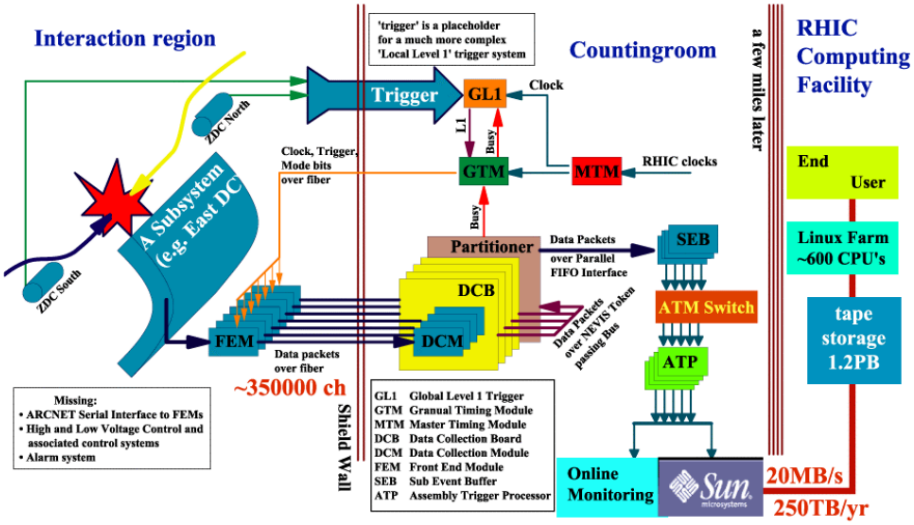

Figure 2.20: A schematic of the DAQ

Analog Memory Units (AMU). The FEM starts to digitize the data once the accept signal is received. The Data Collection Module (DCM) collects the data from each FEM through optical fiber cables. The DCM provides data buffering, zero suppression, error checking and data formatting. The DCM then compresses the data and sends it to the Event Builder (EvB). The EvB assembles each event from the signals from each granule. The event is then written to disk and used for online monitoring and LVL2 software trigger generation. [44]

2.3.6 Event Triggers

The event rate is generally higher than the DAQ can handle. And so a triggering system is necessary to make the most of the delivered luminosity. The triggering systems are designed and optimized to reject uninteresting events and trigger on potentially interesting events. This will also reduce the amount of data that needs to be stored on disk. There are two levels of triggering used at PHENIX, Level 1 (LVL1) and Level 2 (LVL2). This analysis uses the LVL1 and so only that will be discussed below.

The Level 1 trigger system consists of the Local Level-1 (LL1) and the

Global Level-1 (GL1). The LL1 communicates with each detector associated with the trigger and processes the different triggering algorithms. The LL1 sends the results to the GL1 and (as discussed in Sec. 2.3.5) generates the LVL1 accept or reject signal. Once a LVL1 accept signal is received, the system is blocked from receiving a second LVL1 accept signal for some number of bunch crossings. This allows some of the slower detectors to fully collect their signals within the event.

One of the event triggers utilized at PHENIX is the Minimum Bias (MB) trigger. As the name suggests, this trigger is has the smallest bias possible for PHENIX. This is the only trigger used for this analysis and so is the only one to be described. The Minimum Bias trigger uses information derived from the BBC (BBCLL1). The trigger requires that at least one phototube is fired in each BBC (north and south) and that the collision vertex in z is within 38 cm from the nominal interaction vertex.

Chapter 3

Photon Identification Via External Conversions

This Chapter discusses the photon identification. Photons are identified via their external conversion in detector material into e^+e^- pairs. Measuring dilepton pairs is cleaner than measuring photons directly in the EMCal at low p_T. Pairs originating from external conversions must be distinguished from pairs produced in physics processes, such as Dalitz decays. A technique has been developed to cleanly identify conversion pairs by exploiting the misreconstruction of the (off vertex) conversion pair.

PHENIX tracks its charged particles outside of the magnetic field. The field stops just before the drift chamber so that the tracks go straight through the chamber, as well as the rest of the detector. Thus it is necessary to assume a point of origin in order to fix the path of the track. It is natural to assume that all the particles originate from the event vertex, so this is what is done. For most particles this is a correct assumption, but for pairs originating from external conversions, this is not true. The focus is on conversions that occur in the backplane of the HBD. This is where the GEM stacks and read-out boards reside and so is fairly thick, about $2-3\%$ of a radiation length, see [42] for the full breakdown of radiation length in the detector. The backplane of the HBD sits at a radius of about $60cm$ from the interaction point. Electrons originating from $\sim 60cm$ will be misreconstructed under the incorrect assumption of an origin at the event vertex. This misreconstruction is exploited for photon identification, as well as corrected.

The result of the misreconstruction of the electrons and positrons of the pair is that they acquire an artificial opening angle, see Fig. 3.1 for a cartoon. A photon conversion should have zero opening angle (the real photon was massless after all). This artificial opening angle translates to an apparent invariant mass of the pair. The greater the amount of misreconstruction, the larger the apparent mass. The invariant mass can be calculated for a dielectron pair as:

$$
\begin{align}
M^2 &= (E_+ + E_-)^2 - \|\vec{p}_+ + \vec{p}_-\|^2 \tag{3.1} \\
M^2 &= E_+^2 + E_-^2 + 2E_+E_- - (\vec{p}_+^2 + \vec{p}_-^2 + 2\vec{p}_+ \bullet \vec{p}_-) \tag{3.2} \\
M^2 &= p_+^2 + p_-^2 + 2p_+p_- - p_+^2 - p_-^2 - 2p_+p_- cos\theta \tag{3.3} \\
M^2 &= 2p_+p_-(1 - cos\theta) \tag{3.4}
\end{align}
$$

, where M is the invariant mass of the pair, $E_{+/-}$ is the energy of the positron/electron, $\vec{p}_{+/-}$ is the 3-momentum of the positron/electron, $p_{+/-}$ is the magnitude of the 3-momentum and θ is the angle between the electron and positron. The electron mass is ignored in going from line 2 to line 3, the mass is small enough compared to the momentum that this is justifiable ($M_e \approx 0.511 MeV/c^2$ compared to lowest pair transverse momentum of $400 MeV/c^2$). Note that the standard convention of the field is used, where c is set to 1, and so is generally dropped from the units.

The amount of misreconstruction depends on the radius of conversion. The track will be traced through the entire field map during reconstruction, even though it has passed through significantly less. First a more detailed look at the effect just described is presented. Later in the chapter, the correction of the misreconstruction by reparameterizing the reconstructed momenta under an alternate track model assumption is discussed.

3.1 Simulations of External Conversion Sources

Extensive simulations were done to study the nature of conversion pairs in the +- field configuration used during Run 7. Photon events were produced with a flat p_T distribution up to 20 GeV. 200,000 events were generated with 50 photons in each event and the information was written to OSCAR files. These OSCAR files were then fed into PISA with the Run 7 setup. PISA (PHENIX Integrated Simulation Application) is the GEANT implementation of the PHENIX detector. PISA describes the particle interactions with the detectors, both for signal processing, and interactions with inactive material in the aperture (conversions, multiple scattering, etc.). PISA handled all of the conversions and this was sent through the full reconstruction chain to produce files with similar data structure to real recorded events.

A radiogram of the conversion sources from the simulation is shown in Fig. 3.2. The contributions of conversions from different radii are separated. On the left of the figure, the vertex in the x-y plane is shown. The HBD

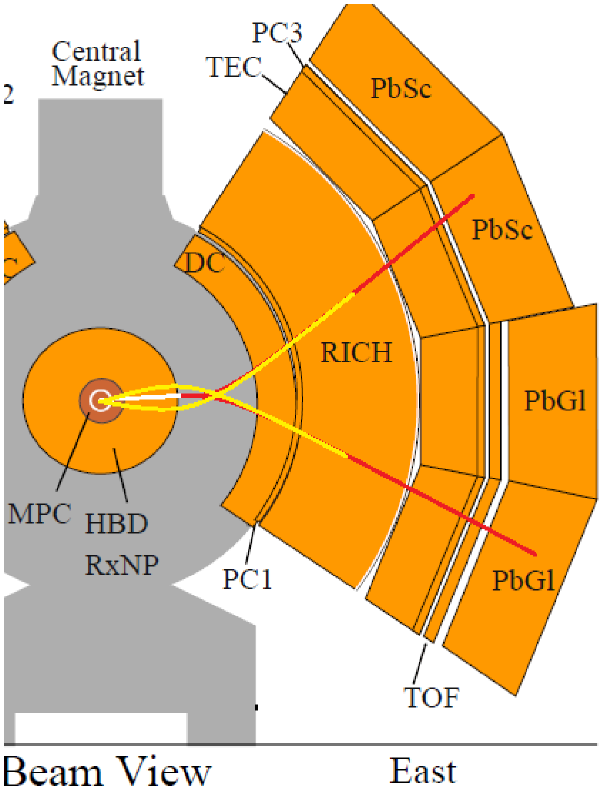

Figure 3.1: A cartoon illustrating the effect of the assumption of the track origin. The red lines represent the true path of the electron and positron track through the detector. They originate from the backplane of the HBD. Note that there is no initial opening angle, only opening of the tracks further down due to the field. The yellow lines represent the track projections incorrectly assuming the particles came from the event vertex. An artificial opening is seen. The effect is exaggerated for clarity.

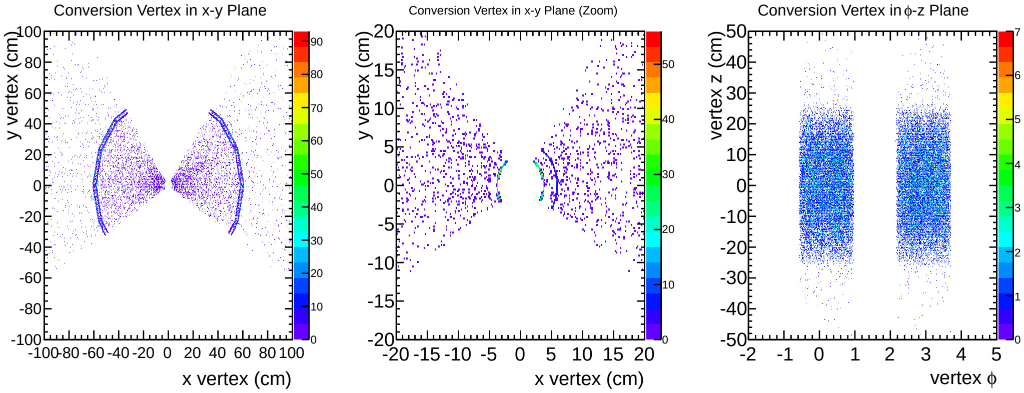

Figure 3.2: On the left, a radiogram of the conversion point in the x-y plane. The middle plot is a zoom of the left hand plot. The right plot is the conversion point in z and ϕ.

backplane is clearly seen at a radius of about $60cm$. It also should be noted that a significant amount of conversions are also expected in the heavy CF_4 radiator gas inside the HBD ($0.564\%X_0$). The middle plot is a zoom in so that the beam pipe and HBD entrance windows are visible. The right plot shows the vertex in ϕ and z.

Fig. 3.3 shows the invariant mass (calculated from reconstructed momenta) distribution of conversion pairs from the above described simulations. As can be seen, the conversions that originate in the HBD backplane (shown in the black open circles) acquire an artificial mass of about 12 MeV. Conversion pairs from the beam pipe (open red squares) and the CF_4 radiator gas in the HBD (open blue triangles) both acquire masses near zero, indicating that the misreconstruction of these pairs is very small (since these sources are closer to the event vertex). The relative yields of the pairs from the various sources is set by material types and thicknesses as put into PISA, and so should accurately represent the material budget in reality.

The dependence of the event vertex on the HBD conversion mass peak has also been studied, see Fig. 3.4

As can be seen from Fig. 3.4, the event vertex greatly modifies the shape of the invariant mass peak (only shown for HBD backplane conversions in the figure). Because of this, only events with a z-vertex within $10cm$ of the nominal vertex are used in the analysis. The complicated structure of the +- field is the cause of this. The field is the most uniform closest to the nominal center of the detector.

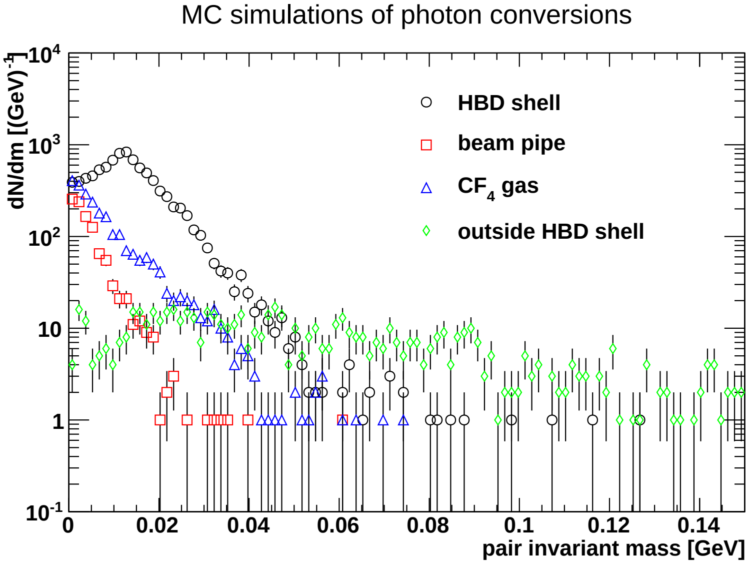

Figure 3.3: The invariant mass distribution of conversion pairs from different radii. The colors represent conversions at a particular radius as represented in the legend. The open symbols represent the mass of pairs reconstructed under the normal PHENIX reconstruction.

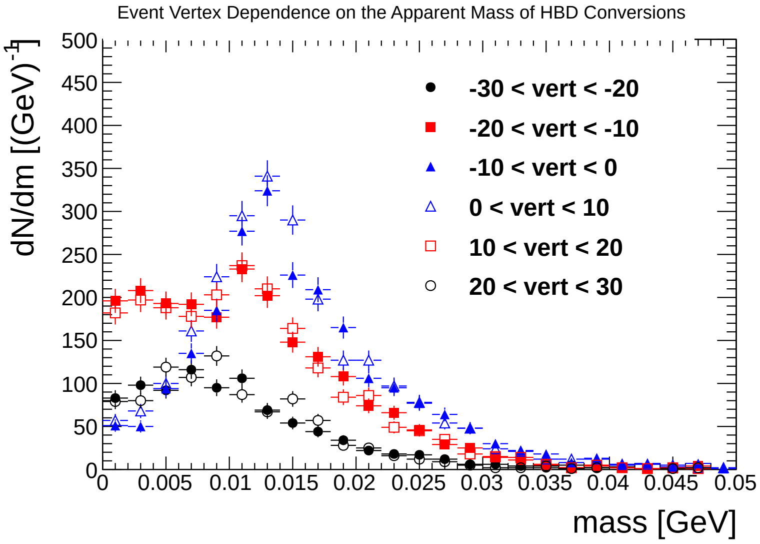

Figure 3.4: The invariant mass peak of photon conversions in the HBD backplane in different z-vertex bins. The peak is greatly smeared for $|z - vertex| > 10cm$.

3.2 The Alternate Track Model

Photon conversions have been rejected in previous PHENIX analyses by cutting on a variable called ϕ_V. ϕ_V is the relative angle between the opening plane of the pair and the magnetic field. Dielectrons from photon conversions will always open up in a plane perpendicular to the magnetic field (they have no intrinsic opening angle and are only opened by the field). But actual decays, such as Dalitz decays ($\pi^0 \to \gamma e^+ e^-$) will open up randomly with respect to the magnetic field. In this way dielectron pairs from photon conversions can be distinguished from dielectron pairs in uninteresting decays by cutting on the orientation of the opening plane of the pair to the magnetic field. This variable works well in the typical ++ magnetic field configuration of PHENIX, but the weaker field in the +- configuration used in Run 7 significantly reduces the discriminating power of the ϕ_V cut.

A conversion recalibrator has been developed to increase the ability to select conversion pairs from the HBD backplane, increasing the photon sample purity. A pure photon sample is essential to the analysis. The conversion recalibrator is designed to correctly reconstruct conversion pairs originating in the HBD backplane by implementing an Alternate Track Model (ATM) where the particles are assumed to come from the HBD backplane rather that the event vertex. The alternate track model is realized by studying Monte Carlo simulations and is simply a reparameterization of the reconstructed momenta with the alternate vertex assumption.

Electrons and positrons have been generated flat in p_T from $0 - 6GeV$. The event vertex is uniformly distributed with $-10 < z < 10cm$. All particles come out radially from the event vertex, but originate from a radius of $60cm$ (the approximate radius of the HBD backplane). These particles are then sent through PISA and the full PHENIX reconstruction chain. A relation between the basic reconstructed values ϕ, z, and α and the true (thrown) ϕ_0, θ, and p_T is observed (for a reminder of the definition of these variables see Sec. 2.3.2). Since all the particles originate at the HBD, the true values are also the values at the HBD. A simple mapping has been found to relate the quantities. The mapping equations are shown in Eqns. 3.5 - 3.7. The supporting plots that show how the mapping equations are obtained are shown in Figs. 3.5 - 3.7.

$$\begin{aligned} p_{T,HBD} &= m/\alpha + b \qquad (3.5) \\ m &= 2.72 \times 10^{-6}|z|^2 - 7.11 \times 10^{-6}|z| + 0.0679 \\ b &= 9.422 \times 10^{-6}|z| + 0.0042 \end{aligned}$$

$$\begin{aligned}\phi_{HBD} = \phi_{DC} - (C_0 + C_1\alpha + C_2\alpha^2 + C_3\alpha^3) \\ C_0 = -0.00191 \\ C_1 = -0.7076 \\ C_2 = -0.03171 \\ C_3 = -0.163\end{aligned} \tag{3.6}$$

$$\begin{aligned}\cos(\theta_{HBD}) = m(z - vertex_{BBC}) + b \\ m = 0.004425 \\ b = -5.15 \times 10^{-5}\end{aligned} \tag{3.7}$$

The effectiveness of the conversion recalibrator can be seen from the residual plots in Fig. 3.8. In each of the plots along the bottom row, the point represents the mean of the residual between the normal reconstruction and the true MC value in solid blue and between the ATM reconstruction and the true MC in solid black points. The error bars on the points represent the RMS of the residual distribution. The residuals are plotted as a function of zed. The far left plot is for p_T, the middle for ϕ_0, and the right plot for θ_0. As can be seen from the plots, the p_T of the conversion track is no longer misreconstructed, as the mean of the residual goes from 0.1 for the normal reconstruction to 0. for the ATM. The RMS is not significantly reduced. The ϕ_0 angle of the track is also improved under the ATM, as can be seen in the reduction of the RMS of the residual distributions. The θ_0 angle is not significantly improved, most likely because the limit of the pad chamber resolution has been hit.

Using the recalibrated angles and p_T, the vector components of the momentum can be recalculated and the ATM invariant mass can be calculated. The recalibrator is applied to all tracks and supplies more information to separate conversion pairs from other sources of pairs. The application of the recalibrator to the simulations described in Sec. 3.1 can be seen in Fig. 3.9. The figure shows the invariant mass distribution plotted for both a normally reconstructed mass, M_{cgl}, (open points) and the ATM mass, M_{atm}, (solid points) for photon conversions at different radii.

As can be seen, the recalibrator has the desired effect in simulation. The conversions from the backplane of the HBD under normal reconstruction acquire a mass of about $12 MeV$, but under the recalibration the mass tends towards zero. This goes exactly as expected, since the pair originate from a real (and massless) photon. Now under the recalibration, all other particles

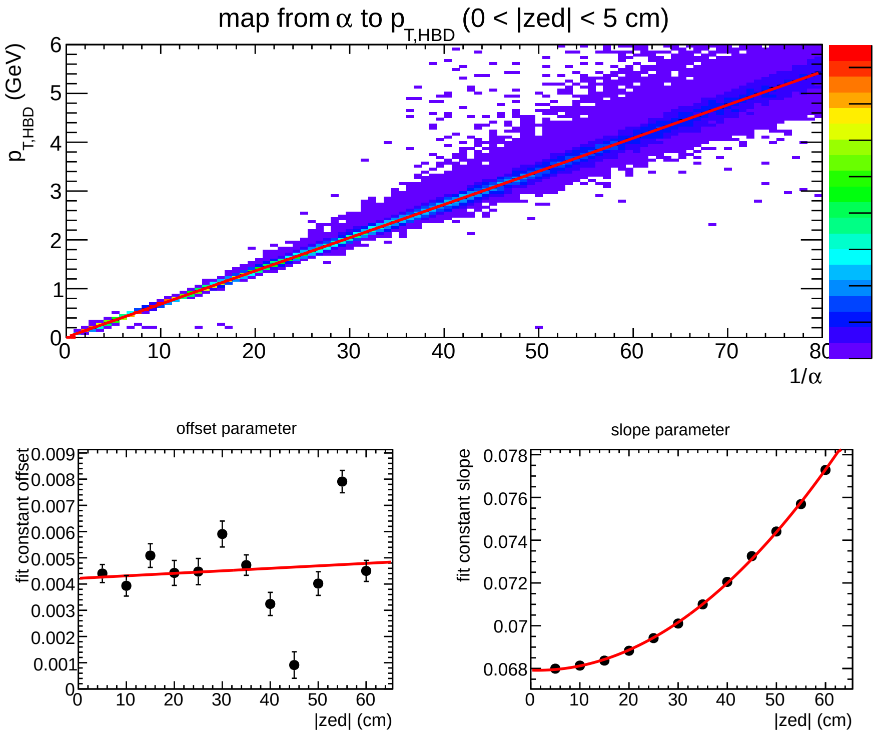

Figure 3.5: A plot of $p_{T,HBD}$ vs. $1/\alpha$ used to extract the mapping function between the two, shown in the top plot of the figure for $|z| < 5cm$ bin. The plot is fit with a line in each zed bin. Shown at the bottom of the figure is the zed dependence of the fit parameters. The mapping extracted from these plots is shown in Eqn. 3.5.

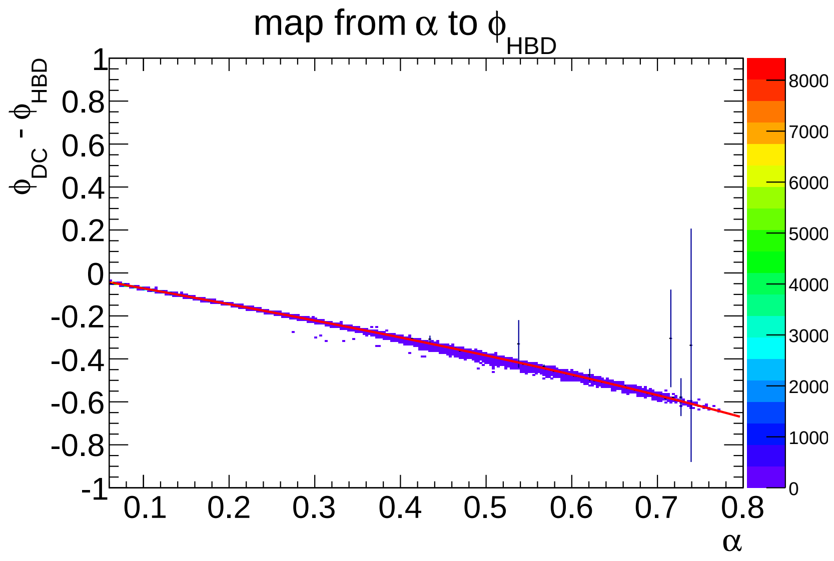

Figure 3.6: A plot of $\phi_{DC} - \phi_{HBD}$ vs. α to extract the ATM ϕ_0. The plot is fit with a third order polynomial. The mapping found is shown in Eqn. 3.6.

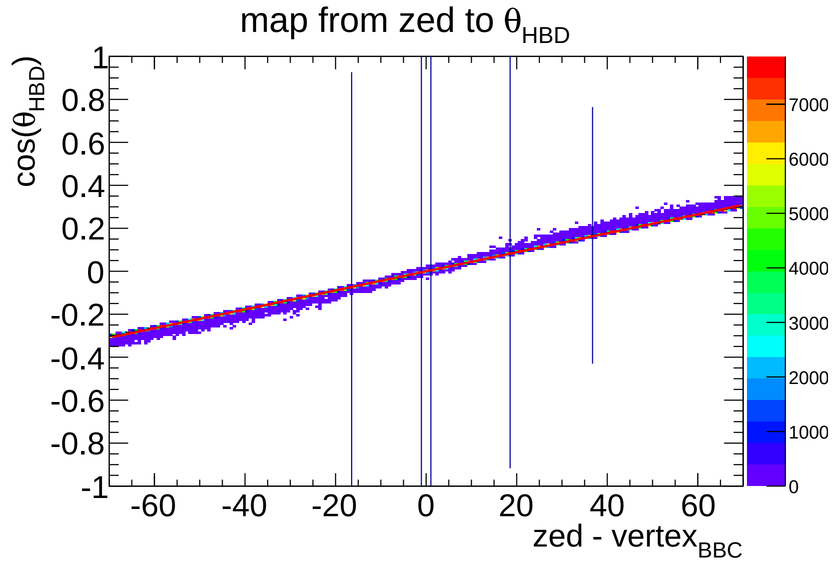

Figure 3.7: A plot of $cos(\theta_{HBD})$ vs. zed-$vertex_{BBC}$ used to extract the ATM θ. The plot is fit with a first order polynomial. The mapping obtained is shown in Eqn. 3.7.

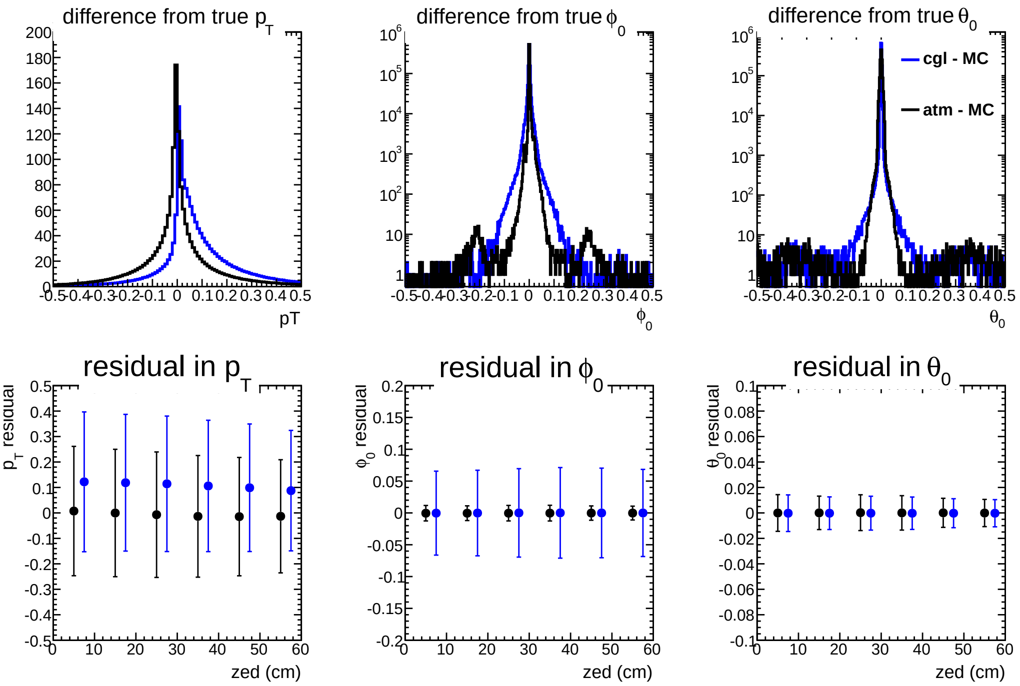

Figure 3.8: This figure shows the effectiveness of the ATM procedure through residuals. Shown on the top of the figure are the residual distributions between normal reconstruction and true MC values (shown in blue) and between the ATM values and the true MC values (shown in black). The bottom plots show this residual as a function of zed. The central points indicate the mean of the distributions, with the error bars indicating the RMS of the residual distribution.

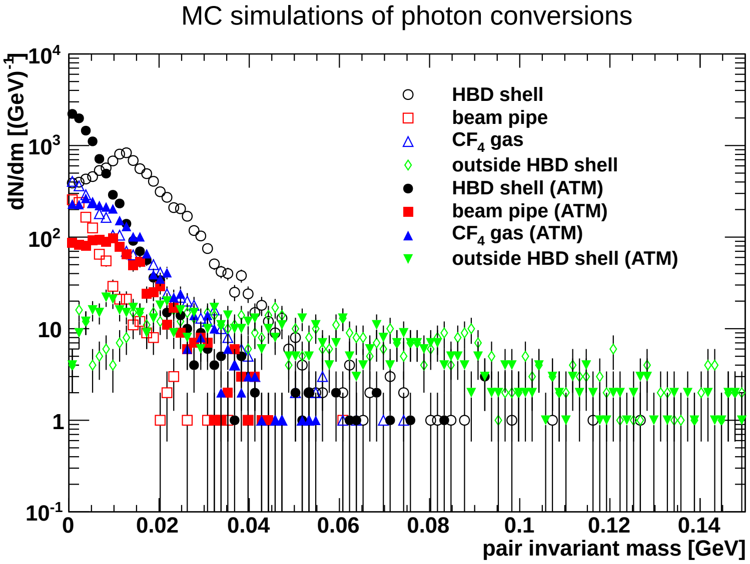

Figure 3.9: The invariant mass distribution of conversion pairs from different radii. The colors represent conversions at a particular radius as represented in the legend. The open symbols represent the mass of pairs reconstructed under the normal PHENIX reconstruction. The closed symbols represent the mass of pairs calculated under the alternate track model.

that actually do come from the event vertex are misreconstructed. This pushes the Dalitz peak up in mass to about $12MeV$. Both of these invariant mass values hold valuable information in correctly identifying conversion pairs from a specific location and so a cut is made on both masses. The exact cuts used are detailed in the next Section 3.3.

3.3 Photon ID Cuts

The specific cuts used are chosen by looking at a 2-dimensional histogram of M_{cgl} vs M_{atm}. As discussed in Sec. 3.1, conversion pairs originating from the HBD backplane acquire an apparent mass of $12MeV$ under the normal track model assumption. And under the alternate track model assumption, where it is assumed that the particle has come from a radius of $60cm$, these same conversion pairs have a mass of about zero (as they correctly should). The effect is the opposite for all pairs that come from the event vertex. These pairs will get shifted up in mass. And so we can cut on how the mass moves under the two track model assumptions. It is required that the pair invariant mass is $10MeV < M_{cgl} < 15MeV$ under the normal track model and $M_{e^+e^-}^{atm} < 4.5MeV$ under the alternate track model.

- $(10MeV < M_{cgl} < 15MeV)\&\&(M_{atm} < 4.5MeV)$

Fig. 3.10 shows the M_{atm} vs. M_{cgl} distribution in the data for dielectron pairs. The mass cuts chosen were chosen based on Fig. 3.10. A box is drawn around the HBD conversion peak (at a normal mass ≈12MeV and ATM mass ≈4MeV). The other peak seen in the figure is the Dalitz pair peak. Also note how the HBD conversion peak sits very high on top of the grass of the combinatorial background (which goes to zero as mass goes to zero).

3.4 Purity of the Photon Sample

The purity of the converted photon sample is studied both through Monte Carlo simulations and directly from the data. Contamination coming from combinatorial background, as well as pairs coming from Dalitz decays and photon conversions from other detector subsystems (or radii) is considered, although the later is not really a source of contamination, since these are also real converted photons. The same simulations described in Sec. 3.1 are utilized for the study of the fraction of photons from other sources that pass the photon identification pair mass cuts. The overall contamination is estimated to be 1%, which is taken as the systematic uncertainty on the inclusive photon yields.

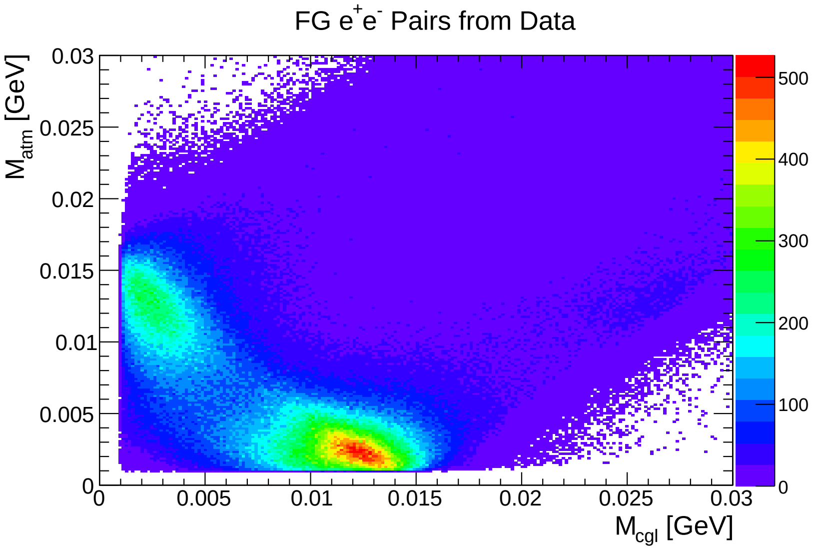

Figure 3.10: A 2-D histogram of the normally reconstructed pair mass vs the ATM calculated pair mass for all e^+e^- pairs in each event. The peak to the lower right is from conversion pairs. The upper peak on the left is from Dalitz pairs.

Fig. 3.11 shows that the conversion sources at each radius (beam pipe, CF_4 radiator gas inside the HBD, the backplane of the HBD, and everything past that) live in different places in the space of the cut. It should be noted that in Fig. 3.11, the relative yield of the conversions is realistically modeled for the different conversions sources within the GEANT simulation. Fig. 3.10 shows this space for all dielectron pairs in data and shows the separation between the Dalitz pairs and the HBD conversion pairs. The contamination from Dalitz pairs is estimated to be 1%. The cuts also reduce the combinatorial background (which is already small at this very low mass) to a less than 1% level, eliminating the need for its subtraction.

Therefore this method of identifying dielectron pairs from photon conversions in the backplane of the HBD is quite pure ($\sim$ 99%) in selecting only those photons, compared to background pairs. This is an improved analysis at low momentum compared to the typical real photon analysis of measuring photons in the Emcal directly, where the contamination from hadrons can be as large as 20% [30]. This allows us to measure photons with increased precision and smaller systematic uncertainties at low momentum compared to the Emcal analysis.

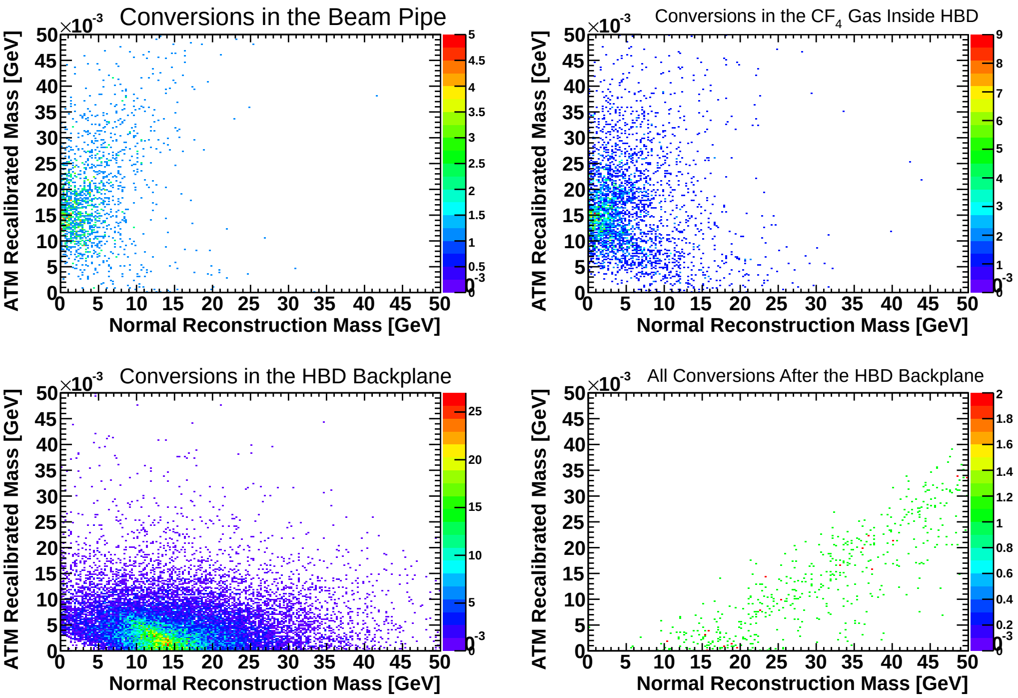
Conversions in the Beam Pipe

Conversions in the CF_4 Gas Inside HBD

Conversions in the HBD Backplane

All Conversions After the HBD Backplane

Figure 3.11: A series of scatter plots of conversions at different radii in the ATM mass vs. normal mass space. The top left plot shows conversions in the beampipe (radius ≈ 4cm). The top right plot shows conversions in the CF_4 radiator gas inside the HBD. The bottom left plot shows conversions in the HBD backplane. The bottom right plot shows all conversions outside of the HBD backplane.

Chapter 4

Analysis: Invariant Yield of Direct Photons

This chapter details the analysis of the invariant yield of direct photons in Au+Au collisions. The data set used is the Run 7 (or 2007 year) set and is based on 1.4×10^9 minimum bias events within $\pm 10cm$ of the nominal event vertex in z.

The invariant yield of direct photons can be calculated from the invariant yield of inclusive photons if the fraction of direct photons above the hadronic background (to be referred to as R_γ) is known, see Eqn. 4.3.

$$\gamma^{direct} = \gamma^{inclusive} - \gamma^{hadron} \tag{4.1}$$

$$\gamma^{direct} = \gamma^{inclusive} \left(1 - \gamma^{hadron} / \gamma^{inclusive}\right) \tag{4.2}$$

$$\gamma^{direct} = \gamma^{inclusive} \left(1 - 1/R_\gamma\right) \tag{4.3}$$

$$R_\gamma = \frac{\gamma^{inclusive}}{\gamma^{hadron}} \tag{4.4}$$

The invariant yield of direct photons can also be calculated from the hadron decay photon invariant yield, via Eqn. 4.5. In this thesis, the hadron decay photon invariant yield is calculated from a Monte Carlo decay generator with spectral shape and meson ratio inputs from data. This has the advantage of smaller systematic uncertainties, since the conversion pair efficiency and acceptance ($\varepsilon_{e^+e^-} a_{e^+e^-}$) and exact conversion probability is not needed. The two results can serve as a cross-check and the result with the smaller systematic uncertainties is chosen for the final result.

$$\gamma^{direct} = \gamma^{hadron}(R_\gamma - 1) \tag{4.5}$$

First a description of the run QA and good run selection is presented, followed by a discussion on the measurement of R_γ and a discussion on the measurement of the inclusive photon invariant yield (uncorrected), the pion tagged photon yield, and the framework for the calculation of the efficiency and acceptance corrections.

4.1 Run QA

This section describes the quality analysis of the data. Only good runs, meeting certain requirements, are analyzed. One such requirement is that there needs to be a minimum of 400,000 events in the run. A run shorter than this most likely had some problem and had to be terminated. Runs in which the centrality or reaction plane angle distribution is not flat are also thrown away. Many of these coincide with runs thrown away for having less than 400,000 events. Runs with special configurations have also been excluded from the analysis. This includes runs with the ++ field configuration, zero field runs and converter runs in which a brass converter was installed around the beam pipe for background electron studies for other analyses.

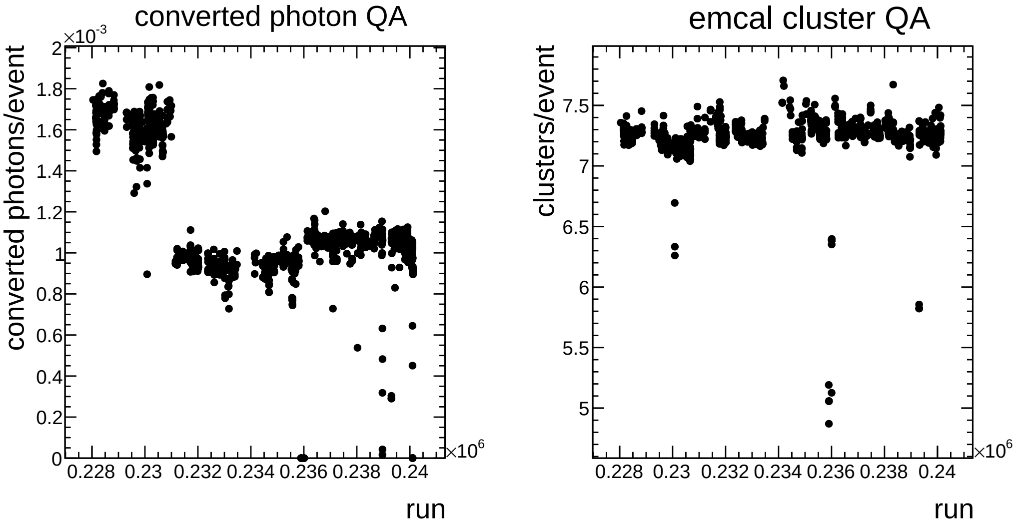

Figure 4.1: Run QA plots for the number of converted photons observed per event in each run (left) and the number of emcal photons observed per event in each run (right).

The number of converted photons and the number of emcal clusters were also checked for each run. This should flag runs which had some problem with a detector subsystem, as the yield may be lower (or higher) than the average of all runs. Fig. 4.1 shows the number of converted photons observed per event in each run on the left and the number of photons in the emcal observed per event for each run on the right. The handful of outlying runs are excluded from this analysis. The drop in the per event yield of converted photons seen after run 231000 is due to the removal of the west half of the HBD (cutting the per event yield in about half). Two separate run groups are considered, but it found to be unnecessary. As described in the next section, the converted photon efficiency drops out in the ratios used to measure the direct photon fraction, R_γ. This explicit cancellation is indeed observed in the data as shown in Fig. 5.2 of Sec. 5.1.

4.2 Direct Photon Fraction, R_γ

This section describes the measurement of the fraction of direct photons above photons from hadron decays. In this thesis, this is defined as $R_\gamma = \frac{\gamma^{incl}}{\gamma^{hadron}}$, where γ^{incl} refers to the yield of all emitted photons in the collision from any source (the inclusive yield) and γ^{hadron} refers to all photons that come from decays of unstable hadrons. A measurement of $R_\gamma > 1$ indicates that there is a direct photon signal to be studied. Experimentally, it is useful to measure a ratio because systematic uncertainties often cancel in the ratio. This is the case in this measurement, where R_γ is measured as a double ratio. Eqn. 4.6 quantifies the observable that is measured.

$$R_\gamma(p_T) = \frac{\gamma^{incl}(p_T)}{\gamma^{hadron}(p_T)} = \frac{\langle \varepsilon_\gamma(p_T) f(p_T)\rangle \cdot \left(\frac{N_\gamma^{incl}(p_T)}{N_\gamma^{\pi^0 tag}(p_T)}\right)_{Data}}{\left(\frac{N_\gamma^{hadron}(p_T)}{N_\gamma^{\pi^0}(p_T)}\right)_{Sim}} \tag{4.6}$$

$$N_\gamma^{incl}(p_T) = c \cdot \varepsilon_{e^+e^-}(p_T) a_{e^+e^-}(p_T) \cdot \gamma^{incl}(p_T) \tag{4.7}$$

$$N^{\pi^0 tag}(p_T) = c \cdot \varepsilon_{e^+e^-}(p_T) a_{e^+e^-}(p_T) \cdot \langle \varepsilon_\gamma(p_T) f(p_T)\rangle \cdot \gamma^{\pi^0}(p_T) \tag{4.8}$$

In the above set of equations, N_γ^{incl} is the number of inclusive photons observed in the PHENIX detector, $N_\gamma^{\pi^0 tag}$ is the number of photons that have been tagged as coming from a π^0 decay. This is done by pairing converted photons in the inclusive sample with clusters from photons measured in the Emcal, see Sec. 4.2.2 for more details. γ^{incl} and γ^{π^0} are the true number of inclusive and π^0 decay photons produced by nature. The remaining factors are corrections that account for the loss of both converted photons and pion tagging from acceptance and detector efficiency. As seen in Eqn. 4.7, to calculate the true inclusive photon yield, it is necessary to correct for the e^+e^- pair reconstruction efficiency ($\varepsilon_{e^+e^-}$) and acceptance ($a_{e^+e^-}$). There is also a factor that quantifies the probability that the photon will convert in material, c. These factors are also present in Eqn. 4.8 for the pion tagged photon sample, but there are additional corrections needed for the acceptance (f) and efficiency (ε_γ) for reconstructing the unconverted photon from a pion decay into the Emcal. Note that the p_T dependent factors are all a function of the converted photon p_T. The advantage of this method is seen when dividing Eqn. 4.7 by Eqn. 4.8 to form the numerator of the double ratio for R_γ in Eqn. 4.6. The electron pair efficiency and acceptance drops out, as well as the conversion probability, which are major sources of systematic uncertainty. The only remaining corrections concern the unconverted photon of pion decays and its response in the Emcal. It should be noted that the unconverted photon acceptance, denoted f, is a conditional acceptance. It is the probability of getting the unconverted photon of a pion decay into the acceptance, given that the converted photon has also been reconstructed (since that correction has been assumed, but drops out). The $\langle\rangle$ around $\varepsilon_\gamma f$ denotes that the correction is averaged over the p_T of the unconverted photon. The term $\frac{N_\gamma^{incl}}{N_\gamma^{\pi^0 tag}}$ in the numerator of Eqn. 4.6 comes directly from the data. All observed converted photons are counted (Sec. 4.2.1), some of which are tagged (statistically) as coming from a neutral pion decay (Sec. 4.2.2). The ratio of these two yields is formed.

The denominator term in Eqn. 4.6, comes from simulation. A photon decay cocktail is calculated to estimate the contributions of decay photons from hadrons other than the neutral pion. The ratio of all decay photons to the number of decay photons from π^0s is calculated from the cocktail. Again, the formation of the ratio serves to reduce systematic uncertainties, as the systematic uncertainty due to the parameterization of the pion spectral shape in the cocktail (roughly a 10% systematic) largely cancels when the ratio is formed. The details of this term are presented in Sec. 4.2.3.

The calculation of each term of Eqn. 4.6 is described in the following subsections.

4.2.1 Inclusive Photon Yield

Inclusive photon p_T spectra for each centrality bin are shown and discussed in this section. The measurement begins with single electron and positron tracks.

The basic electron id comes from responses in the RICH and Emcal detectors. The specific cuts used at the single electron level are listed below:

- $0.2 < p_T < 20.GeV$
- quality = 31 or quality = 51 or quality = 63
- $disp < 5.0$
- $n0 >= 3$
- $\chi^2/npe0 < 10$
- $e/p > 0.5$
- $ecore > 0.150GeV$

The first listed cut is on the transverse momentum of the track measured in the drift chamber. The acceptance is limited below 200MeV, tracks begin to curl up inside the magnetic field, rather than flying through the entire central arm.

The next item is a cut on the track quality, with quality defined in Sec. 2.3.2. Only good quality tracks are considered.

The disp cut is a cut on the displacement of the ring center in the RICH with the track projection to the RICH. It is required that this displacement is less than 5cm.

The cut on $n0$ is the main electron id cut. The n0 cut is a cut on the number of RICH PMTs fired within an annulus around the track projection with an inner radius of 3.4cm and an outer radius of 8.4cm. The ring radii are chosen based on the expected ring radius of the electrons of 5.9cm. The 2.5cm width around the nominal radius is from the position resolution of the PMTs, defined by the PMT size.

A second RICH eid cut is used. This cut is on the ratio of two variables, χ^2 and npe0. The χ^2 parameter is the RMS^2 of the positions of the hit PMTs weighted by the number of photoelectrons in the hit PMTs compared to the expected distribution from an electron track within a radius of 11cm around the track projection. This parameterizes the goodness of the hit distribution. It has units of cm^2. npe0 is the number of photoelectrons in the hit PMTs in the ring of inner radius 3.4cm and an outer radius of 8.4cm.

A third electron id cut is applied on the energy to momentum ratio of the track. Here the energy is measured in the Emcal, while the momentum is measured in the drift chamber. An electron will have an energy/momentum ratio very close to one, since the electron will deposit all its energy in the

Emcal. This is not true for heavier particles, such as hadrons, which have a different interaction with the Emcal and will only deposit some fraction of its momentum into the calorimeter.

Finally a minimum ecore, or energy deposition, into the Emcal is required to reduce noise.

A track passing these cuts is then considered an electron (or positron). The charge sign is determined with the drift chamber.

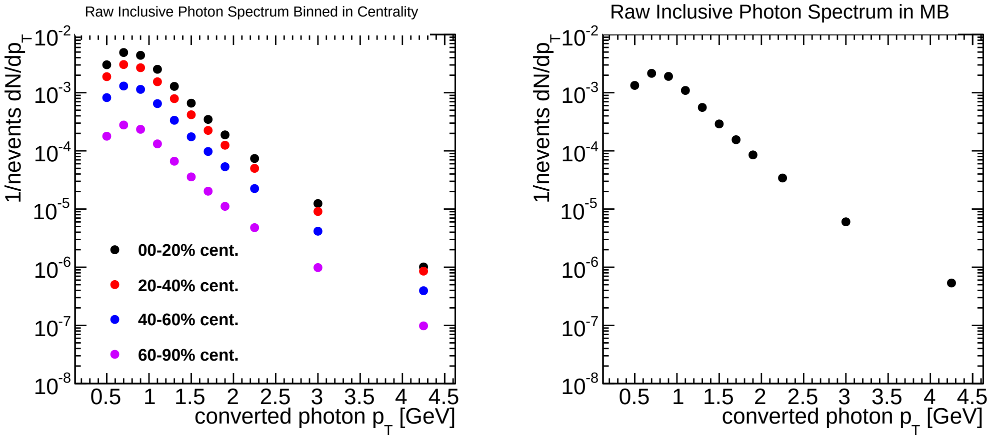

Figure 4.2: The raw per event inclusive photon p_T distribution. The left is for various centrality bins as described in the legend. The right plot shows the MB centrality selection.

All electron-positron pairs within an event passing the mass cuts described in Sec. 3.3 are counted as converted photons. The uncorrected dN/dp_T distribution is shown for all centrality selections in Fig. 4.2. The inclusive spectra for the $0-20\%$, $20-40\%$, $40-60\%$, and $60-90\%$ centrality bins are shown on the left side of the figure. The right plot shows the yield in the Minimum Bias centrality selection. Each spectrum is normalized by the total number of events analyzed. Poisson statistics is assumed and the statistical error on the inclusive spectrum is taken to be $\sqrt{N}$, where N is the number of counts in a p_T bin.

4.2.2 Pion Decay Tagged Photon Yield

The spectra of photons tagged as coming from π^0 decays for each centrality is shown in this section. Converted photons are tagged as coming from a π^0 decay by pairing the converted photons with photons that are detected directly in the Emcal. The identification of the unconverted photon of a hadron decay is done solely with the Emcal. Only one cut is used on the Emcal response to identify clusters that likely have come from a photon. The other cut is simply on the minimum energy of a cluster. To identify clusters from photons, it is required that the variable $\chi^2 < 3$. This variable is similar to the χ^2 variable in the RICH. It compares the measured shower profile in the towers and compares it to the expected shower of a photon determined from test beam studies. The cut used is a rather loose photon identification cut.

The remaining cut requires that the minimum energy of a cluster is greater than 600MeV. This is somewhat arbitrarily chosen as a consequence of the data production and what is available in produced data files. In principle one can push to lower energy, but the current data set production does not allow for that possibility. This analysis is largely systematics dominated and so pushing to lower energy will not improve the result significantly.

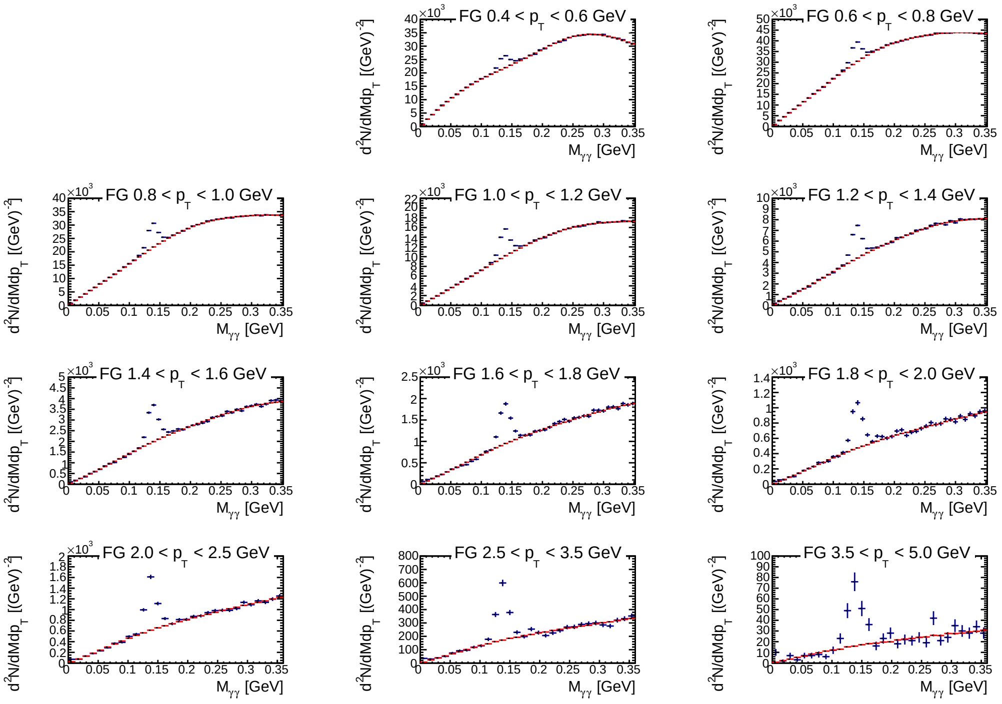

Figure 4.3: The converted photon-photon FG pair invariant mass distribution in black shown with the normalized combinatorial BG mass distribution in red for each converted photon p_T bin in the MB centrality selection.

The standard method of pion reconstruction is performed where all pairs of photons within an event are made and histogrammed as a function of the pair invariant mass. This is done in bins of converted photon p_T so as to count the number of inclusive photons that come from a neutral pion decay. Combinatorial background is subtracted by using a mixed event technique. Within this technique, converted photons from one event are paired with photons in the Emcal from completely different events, so that there cannot possibly be a correlation, the distributions obtained are purely combinatorial. The different events used for the pairings are required to be close in centrality and event vertex to reduce differences in multiplicity between the events. The foreground pairs (pairs from within the same event) are denoted FG. The combinatorial background pairs from different events are denoted BG. The FG and normalized BG pair invariant mass distributions for each converted photon p_T bin is shown in Fig. 4.3. The normalization is found by looking at the ratio of FG to BG in a mass window around the pion peak where the correlated background is expected to be small, see Fig. 4.4. The best BG subtraction results from fitting the FG/BG ratio with a second order polynomial. This indicates that there may be some additional correlation in the FG. A constant, first and second order polynomial were all included in the analysis and the deviation in the yield is taken to be an estimate of the systematic uncertainty on the pion yield extraction, see Sec. 4.2.5 for a discussion. The plots are for MB centrality selection.

Fig. 4.5 shows the FG - normalized BG distributions in MB events. A clean pion peak is observed. Fig. 4.6 shows the uncorrected dN/dp_T distribution for the pion decay tagged photons for various centrality bins (left) in MB centrality (right), obtained by integrating the peaks in Fig. 4.5.

4.2.3 The Hadron Decay Photon Cocktail

This section describes how the denominator of the double ratio in Eqn. 4.6 is calculated. As can be seen from Eqn. 4.6, only the pion component to the inclusive photon yield is directly measured within this analysis. Neutral pions account for roughly 80% of all decay photons observed. The other sources of decay photons are taken into account with a hadron decay photon cocktail based on real data measurements.

The term cocktail will be used frequently and is used to indicate that we mix many ingredients together to get a final spectrum. The ingredients to the hadron cocktail are the following decays:

- $\pi^0 \to \gamma + \gamma$ (BR = 0.98)
- $\eta \to \gamma + \gamma$ (BR = 0.39)
- $\eta \to \pi^+ + \pi^- + \gamma$ (BR = 0.046)

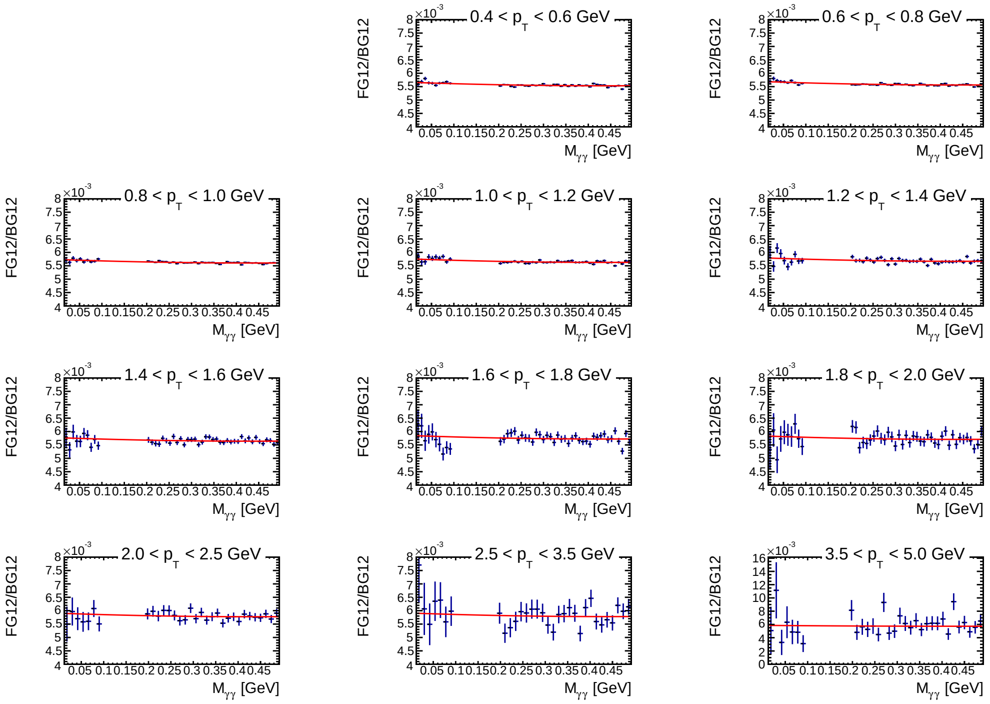

Figure 4.4: The converted photon-photon FG pair distribution in mass divided by the combinatorial BG distribution. The region of the pion peak is excluded. The ratio is fit with a second order polynomial (shown in red) to obtain the normalization used in Fig. 4.3.

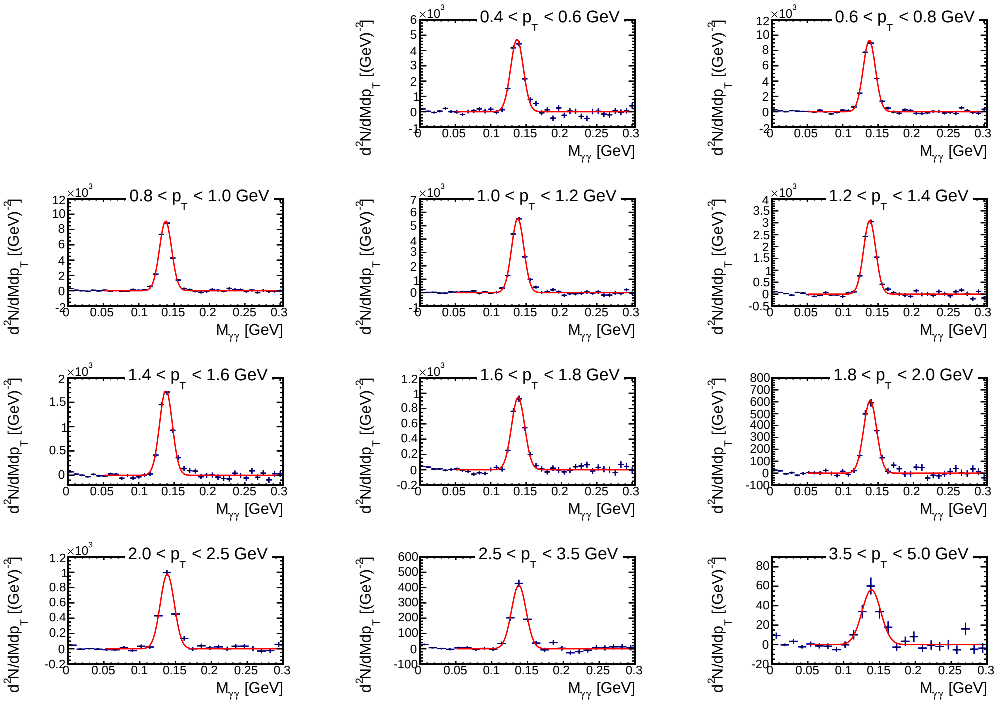

Figure 4.5: The FG - normalized BG mass distribution for each p_T bin in MB. The π^0 signal is extracted by integrating the peak.

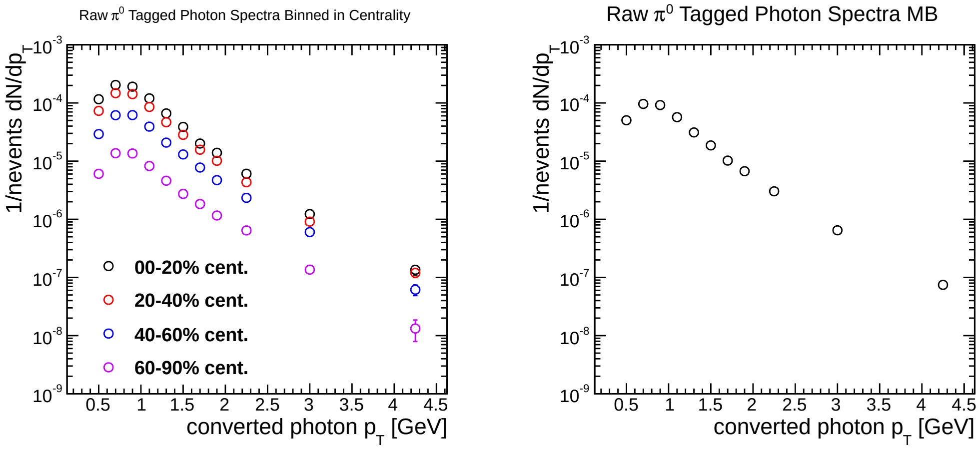

Figure 4.6: The raw yield of inclusive photons tagged as coming from a π^0 decay as a function of p_T. The left plot shows the yield in various centrality bins as described in the legend. The right plot shows the yield in the minimum bias centrality selection.

- $\eta' \rightarrow \gamma + \gamma$ (BR = 0.0218)
- $\eta' \rightarrow \pi^+ + \pi^- + \gamma$ (BR = 0.293)
- $\eta' \rightarrow \omega + \gamma$ (BR = 0.0275)
- $\omega \rightarrow \pi^0 + \gamma$ (BR = 0.0828)

These are the dominant decay processes (all the processes with a branching ratio greater than 1%). Decays that produce only π^0s as decay products (such as $\eta \rightarrow \pi^0 + \pi^0 + \pi^0$) are not included in the cocktail, since the pion measurement from which the simulation is based already includes these pions and double counting would occur if included. The one exception to this are off-vertex produced pions from K_s^0 decays. These contributions have been estimated and subtracted from the pion spectrum in [26] on which the pion spectral shape parameterization is based. This contribution has been previously studied and is estimated to be small (on the order of 3% for $p_T > 1GeV$) and is covered by the quoted systematic uncertainties on the hadronic decay photon cocktail.

The Exodus decay generator is used to calculate the cocktail as in [28]. The p_T shape of the π^0 is parameterized from a fit to published data with a modified Hagedorn function (see Eqn. 4.9) and is taken directly from [28]. All the other included hadron shapes are assumed from m_T scaling, where p_T in Eqn. 4.9 is replaced by $m_T = \sqrt{m^2 + p_T^2}$ for each hadron species. The parameters extracted from the fits to data for the pion p_T shape for each centrality bin are shown in Table 4.1. Fig. 4.7 shows the pion data used for the fit (left) as well as the ratio of the data points to the fit. There is an observed discrepancy between the Run 2 and the Run 4 π^0 measurements in the range of 2 - 8 GeV. This is unfortunate, but is the state of the measurements, therefore this discrepancy is folded in to the systematic uncertainties on the pion spectral shape that gets propagated to the direct photon invariant yield.

$$E\frac{d^3\sigma}{dp3} = A(e^{-(ap_{\mathrm{T}}+bp_{\mathrm{T}}^2)} + p_{\mathrm{T}}/p_0)^{-n} \tag{4.9}$$

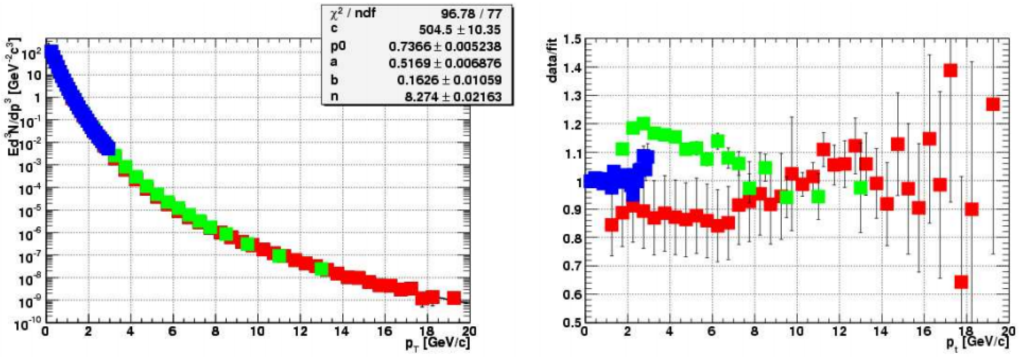

Figure 4.7: This figure shows the results of the fit to the existing pion data used to parameterize the pion spectral shape input into the cocktail calculation. The left panel shows the invariant yield data. The right panel shows the ratio of the data points to the fit. Blue data points come from charged pion spectra [45], green and red data points are from neutral pion spectra from Run2 [46] and Run 4 [25], respectively. The results shown are for the minimum bias centrality selection.

The other input needed for the cocktail is the individual weighting of the yield of each species. All meson species are weighted relative to the pions, and so the meson to pion ratio for each species is taken from measured data [47] [48] [49]. These values are all summarized in Table 4.2. The spectra are normalized at $p_T = 5GeV/c$.

Fig. 4.8 shows the hadron decay photon cocktail as a function of p_T for the Min. Bias centrality selection (bottom right panel). Each meson species contribution is shown by a different color as indicated in the legend. The

cent [%]	c [(GeV/c)$^{-2}$]	a [(GeV/c)$^{-1}$]	b [(GeV/c)$^{-2}$]	p_0 [GeV/c]	n	$\frac{dN_{\pi^0}}{dy}$
MB	504.5	0.5169	0.1626	0.7366	8.274	95.7
0-10	1331.0	0.5654	0.1945	0.7429	8.361	280.9
10-20	1001.0	0.5260	0.1628	0.7511	8.348	200.6
20-30	750.7	0.4900	0.1506	0.7478	8.299	140.5
30-40	535.3	0.4534	0.1325	0.7525	8.333	93.8
40-50	364.5	0.4333	0.1221	0.7385	8.261	59.2
50-60	231.2	0.4220	0.1027	0.7258	8.220	35.0
60-70	118.1	0.4416	0.0559	0.7230	8.163	17.9
70-80	69.2	0.2850	0.0347	0.7787	8.532	8.8
80-92	51.1	0.2470	0.0619	0.7101	8.453	5.0

Table 4.1: Fit parameters for the neutral pion invariant p_T distributions according to Eqn. 4.9. In addition, the last column gives the integrated neutral pion yield corresponding to the parametrization.

Meson	Relative Yield to Pions
π^0	1
η	0.46 ± 0.06 [47]
η'	0.25 ± 0.075 [48]
ω	0.9 ± 0.06 [49]

Table 4.2: Hadron rapidity densities used in our hadron decay generator. For the ω and ϕ, data from this analysis were used together with data from the quoted references.

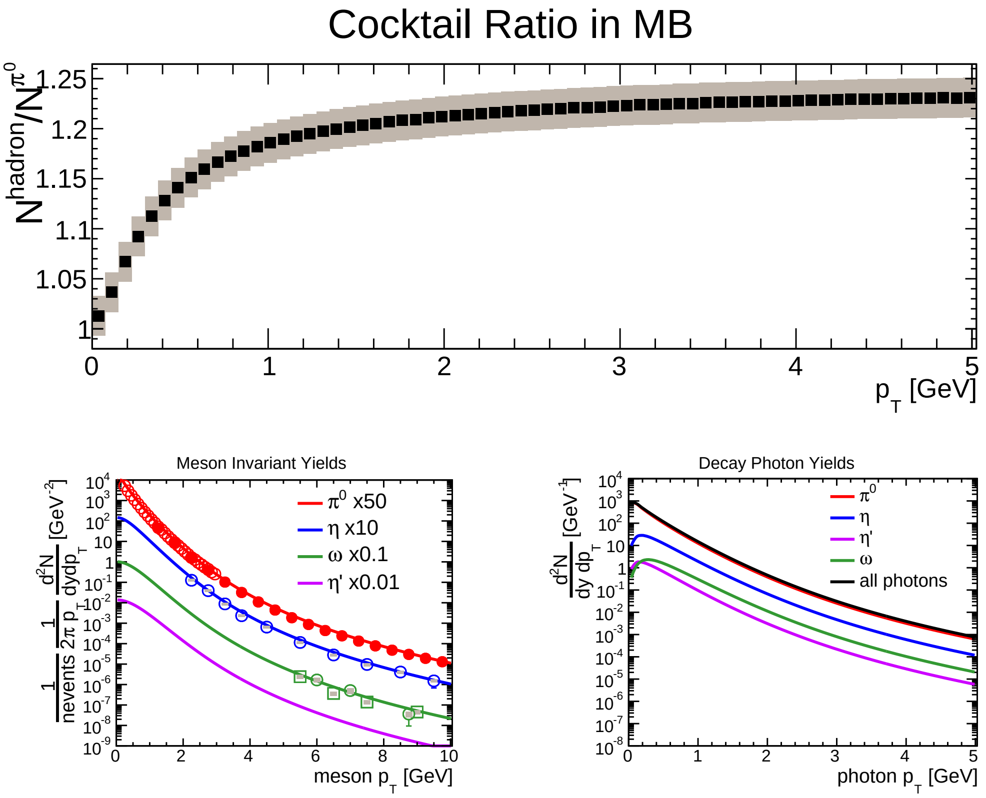

Figure 4.8: Top Panel: The cocktail ratio of the total number of decay photons to the decay photons from pions. The shaded region indicates the systematic uncertainty on the ratio. Bottom Left Panel: The invariant yield of each meson included in the cocktail. Each color represents a different species as indicated in the legend. The cocktail is represented by the lines. The points are published PHENIX data [45] [26] [50] [51]. Bottom Right Panel: The per event yield of decay photons from the mesons.

bottom left panel of Fig. 4.8 shows the parent invariant yields for each meson species input into the cocktail, represented by the colored lines. The points represent PHENIX published data points from the references shown in the caption. The top panel shows the ratio of the total decay photons to the decay photons from neutral pion decays. This is the quantity of interest to calculate R_γ and is the denominator of the double ratio in Eqn. 4.6. The gray shaded region shows the systematic uncertainty on the ratio, see the discussion on the systematic uncertainty in a later subsection.

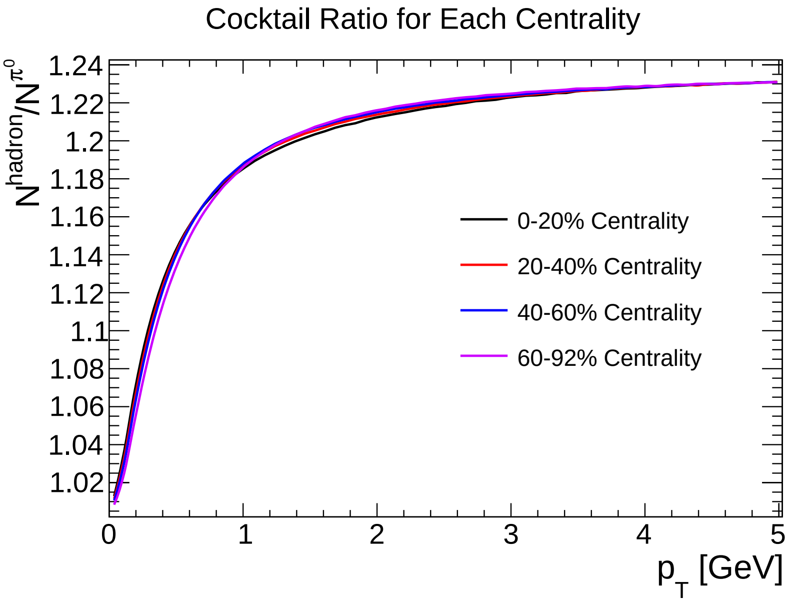

Figure 4.9: The number of total decay photons divided by the number of neutral pion decay photons (the cocktail ratio) for each centrality, as shown by the colored lines.

The cocktail ratio for each centrality bin is shown in Fig. 4.9. There is very little dependence of centrality on the ratio. This makes sense for two reasons. For one, the input η/π^0 ratio is the same for all centralities. The published data [47] shows that this ratio seems to be universal for different collisions species. Secondly, the shape of each meson is based on the input pion spectrum and obtained from m_T scaling. Therefore one would expect that most of the shape differences cancel in the ratio. This is indeed what is observed in Fig. 4.9. As mentioned already, this cancellation of systematic uncertainties is the very reason that the ratio is the measured quantity.

4.2.4 Corrections from Monte Carlo Simulations

A full Monte Carlo simulation is done to calculate the efficiency and acceptance corrections. The simulated tracks are then embedded into real Au+Au events to take into account occupancy effects from the high multiplicity Au+Au collisions. The simulation starts with neutral pions. The Exodus decay simulator mentioned in the previous subsection is used to produce single neutral pion events. These pions are decayed into two photons. Then one of the photons is forced to convert at a radius of 60 cm. The electron and positron emitted from the conversion process fly out in the same exact direction as the parent photon. The momentum of the electron is randomly chosen, with the momentum of the positron then determined from momentum conservation and the parent photon energy. The momentum of the parent pions is thrown flat in p_T. A weight is then applied during the analysis to incorporate a realistic momentum distribution. The weight is the Hagedorn function described in Sec. 4.2.3 with parameters from Table 4.1.

Next these pion decay events are sent through a GEANT simulation (PISA) to take into account the expected response of the detectors. All the detector subsystems, with active and inactive detector areas, are put into the PISA simulation. The output of the PISA simulation is a datafile in the same form as the raw PHENIX data file, having raw detector responses encoded in it. The GEANT simulation handles multiple scattering of charged tracks through material, Bremsstrahlung, and external photon conversions. The next step is then to run the PHENIX reconstruction software on the PISA output. The last step is embedding these files into real data events. Since the only important corrections deal with the Emcal corrections, the embedding is run only for the Emcal detector. This involves having an algorithm to uncluster the clusters from the data and the simulated files, merge the energy depositions from the two files, and then run the clusterizer again. The full embedding simulation takes into account acceptance, efficiency, and occupancy corrections (for the Emcal clusters).

Cross Checks of Single Particle Cuts

Many cross-checks are performed to ensure the accuracy of the simulation in its depiction of reality. These cross-checks come in the form of comparing simulated and real data pion reconstruction and response to cuts. First, the single electron cuts are checked by comparing the distributions of n_0, disp, $\chi^2/npe0$, and E/p for electrons and positrons in Figs. 4.10 and 4.11 respectively in simulation and data. A reasonable match is observed. Efficiency losses due to the cuts will drop out when the double ratio is formed to calculate R_γ, so little differences do not matter.

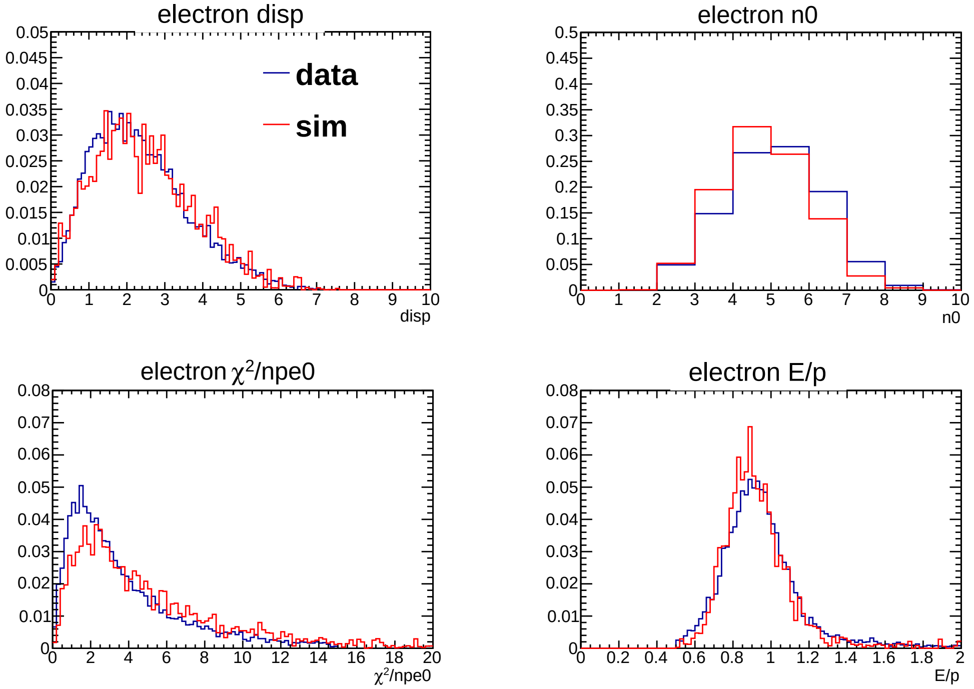

Figure 4.10: The comparison of the single electron cuts in simulation and data. All eid cuts are made except for the one we want to compare. The data distribution is in black and the simulation distribution in red.

Fig. 4.12 shows the comparison of the ϕ distribution of charged particles in simulation and data. ϕ regions of lower counts indicates some partially dead or inefficient area. There is a reasonable match between the simulation and the data. The systematic uncertainty on $a_{e^+e^-}$ is estimated as 10% based on Fig. 4.12 by calculating the percent difference between the yields averaged over the ϕ bins. This systematic uncertainty cancels for R_γ, but not for the calculation of the direct photon invariant yield (Sec. 4.3).

Comparisons of the χ^2 distributions for the identification of the unconverted photon in the Emcal in data and simulation are shown in Figs. 4.13 and 4.14 for the PbSc and PbGl sectors respectively. The comparison is made in each centrality bin of the analysis. The curves are normalized in the peak region. The match looks good within the peak region. There is hadron background present in the data, but absent in the simulation, which is why the data curve is higher than the simulation at higher χ^2 values. The reconstruction efficiency due to the cut is calculated from these plots by simply comparing

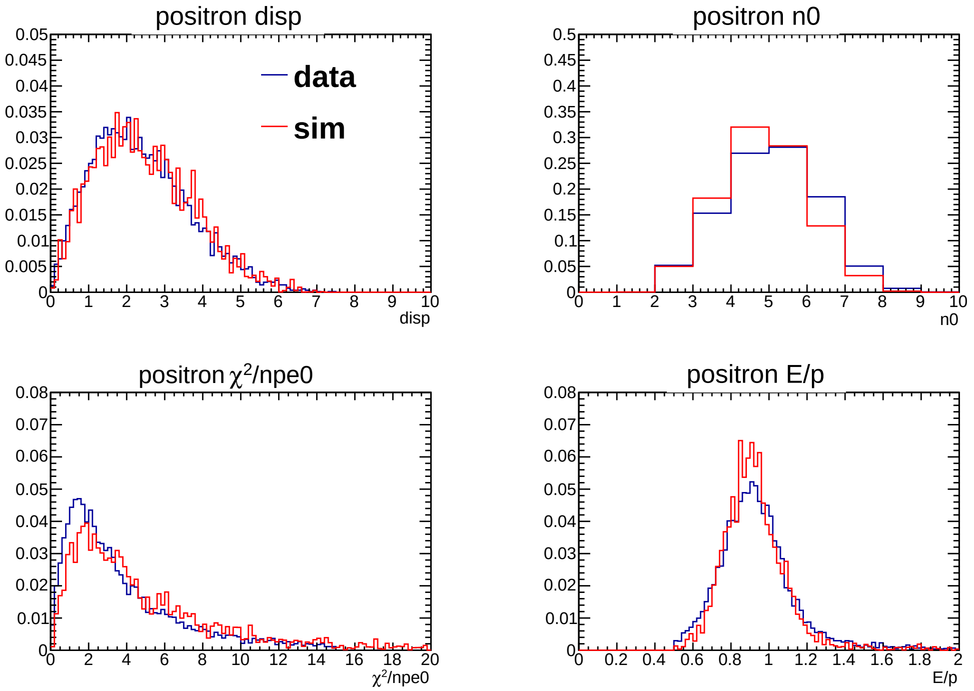

Figure 4.11: The comparison of the single positron cuts in simulation and data. All eid cuts are made except for the one we want to compare. The data distribution is in black and the simulation distribution in red.

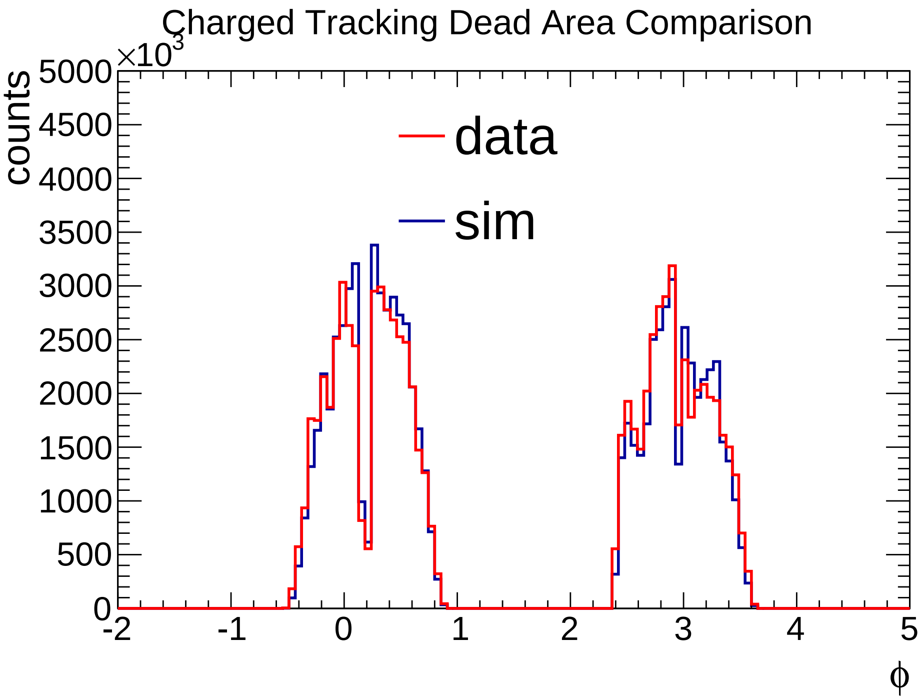

Figure 4.12: A comparison plot of the charged track dead maps in simulation and data expressed as the ϕ distribution of charged tracks. The yield is integrated over p_T.

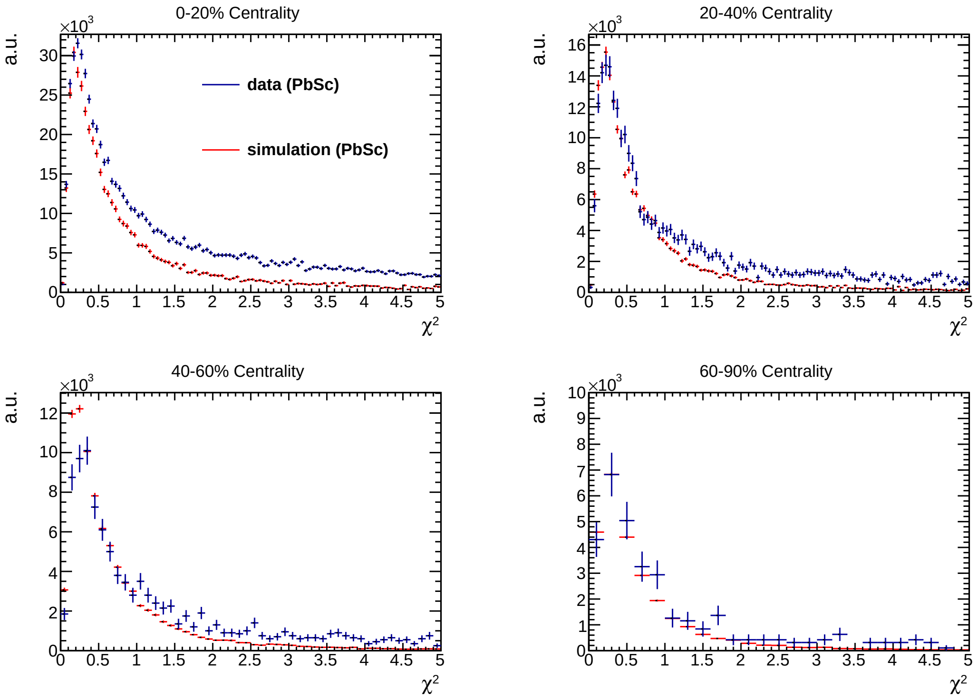

Figure 4.13: The comparison of the χ^2 distribution in the Emcal between data and simulation in each centrality bin for the PbSc sectors. The plot is over all photon energies and so is dominated by low energy photons.

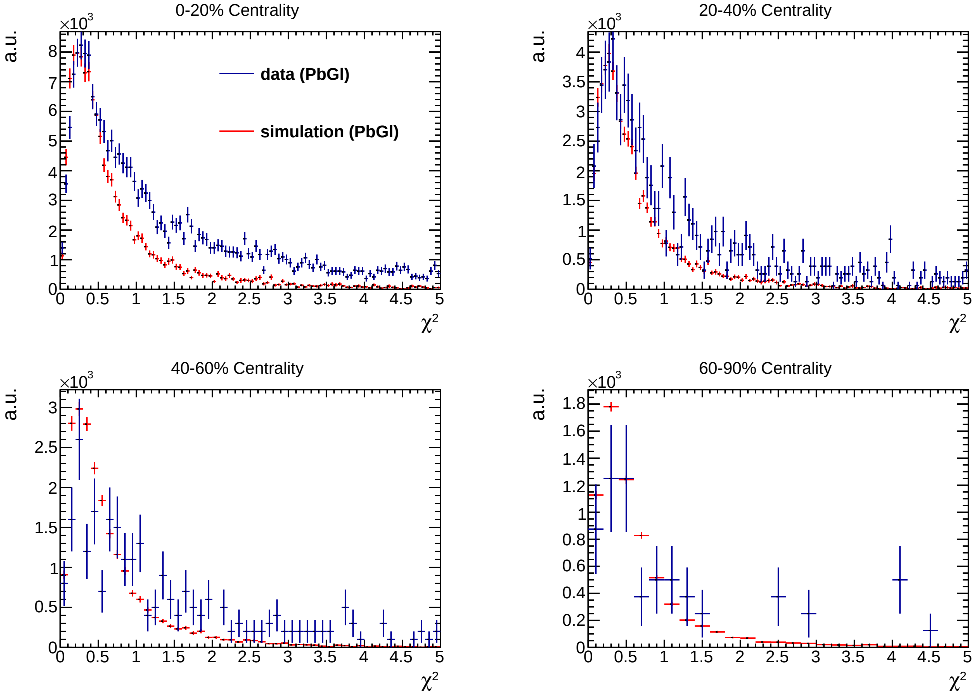

Figure 4.14: The comparison of the χ^2 distribution in the Emcal between data and simulation in each centrality bin for the PbGl sectors. The plot is over all photon energies and so is dominated by low energy photons.

the integral below the cut to the total integral. The calculated efficiencies from the simulation are shown in Fig. 4.15 for the PbSc and PbGl sectors. Each colored line in the figure represents a centrality bin.

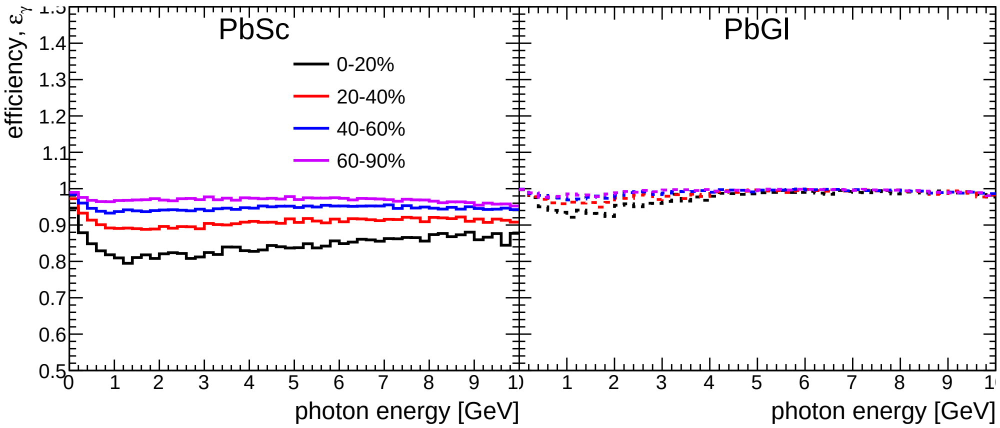

Figure 4.15: The efficiency of the photon reconstruction in the Emcal. The efficiency for the PbSc (PbGl) is shown on the left (right) plot of the figure. The colored lines represent each centrality bin as shown in the legend.

Cross Check with Published Neutral Pion Spectra

A further cross-check is made to ensure that the neutral pion is reconstructed properly in the converted photon/photon reconstruction channel and that the detector resolution in simulation matches the real detector resolution. Figs. 4.16 and 4.17 make the comparison of the π^0 peak position and width respectively in simulation and data for the four centrality bins in the analysis. A reasonable match in simulation and data is achieved after recalibrating the Emcal cluster energy in the simulation.

The same simulation is used to calculate a full correction $(a_{e^+e^-}\varepsilon_{e^+e^-}a_\gamma\varepsilon_\gamma)$ to the π^0 yield. The corrected π^0 invariant yield is then compared to published data [26] to ensure that the analysis gives reasonable results. The systematic uncertainties on this type of measurement are rather large, so this comparison is used only as a sanity and consistency check. The yield comparisons can be seen in Fig. 4.18 for each centrality bin. The top row in the figure compares the invariant yields directly. The bottom row shows the ratio of the invariant yields. In the figure, no conversion probability is assumed, the

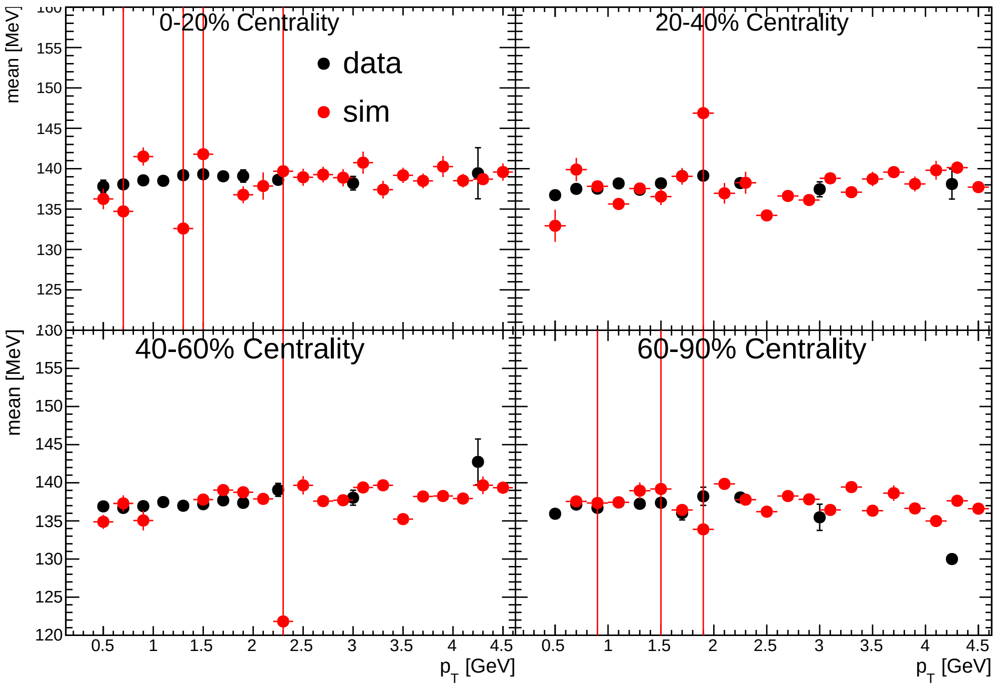

Figure 4.16: A comparison of the mean of the pion mass distribution in simulation and data as a function of p_T and shown in the four centrality bins.

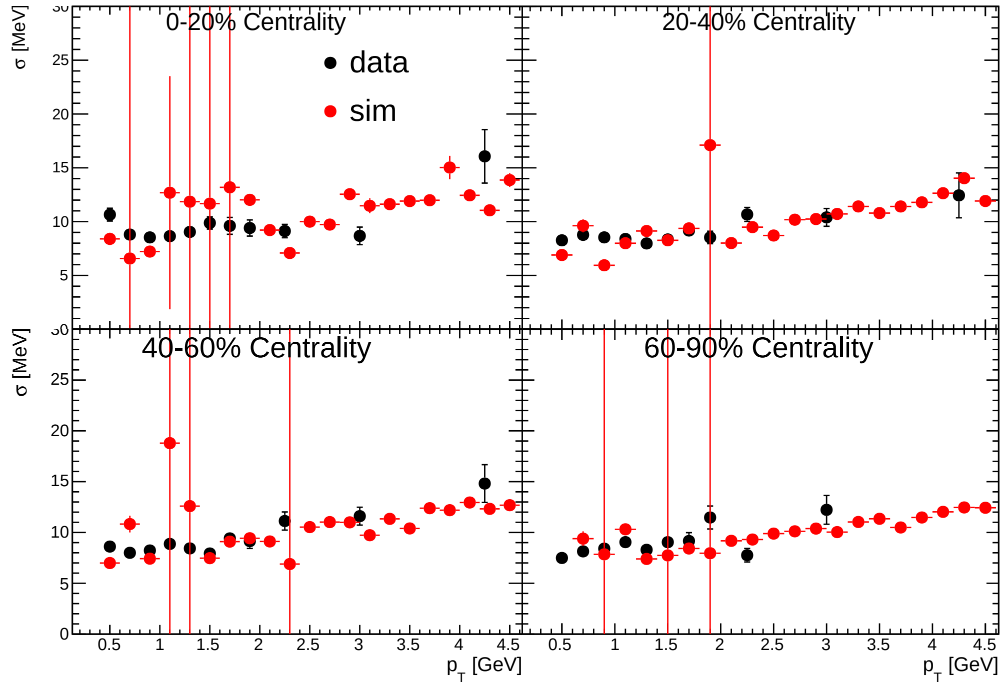

Figure 4.17: A comparison of the width of the pion mass distribution in simulation and data as a function of p_T and shown in the four centrality bins. The width is quantified by the σ of the Gaussian fit to the pion data.

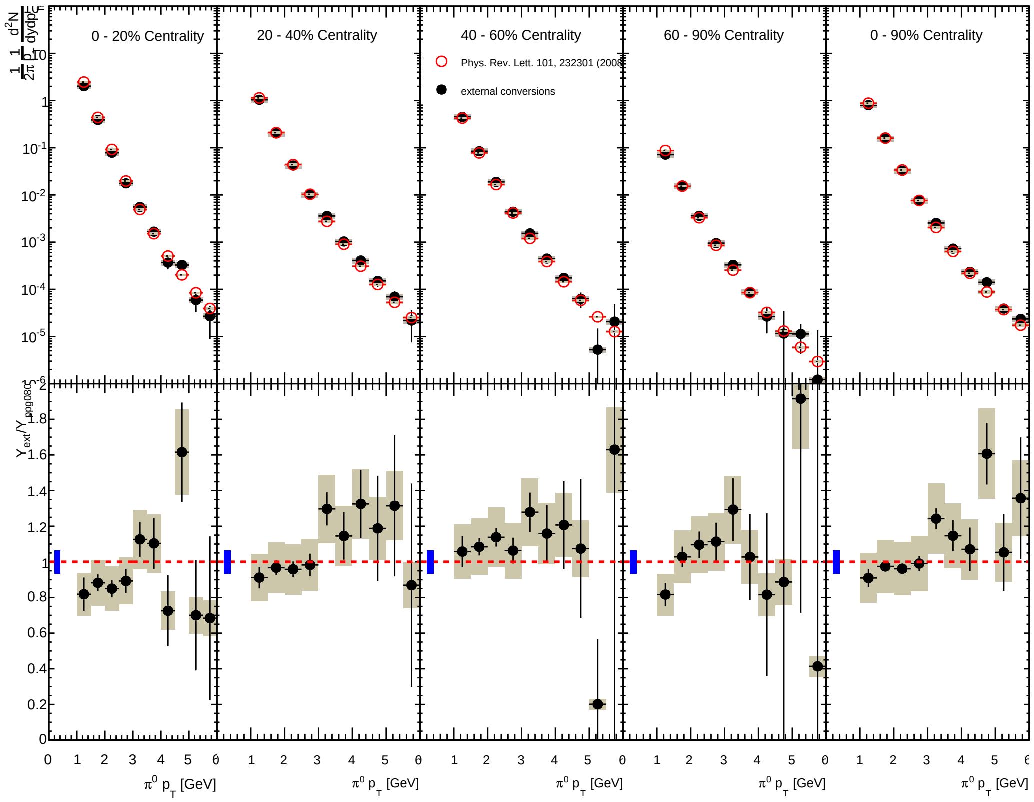

Figure 4.18: Top Row: The comparison of the invariant yield of neutral pions as a function of p_T for each centrality bin to published data [26]. Bottom Row: The ratio of the invariant yields. The blue band represents the overall scale uncertainty on the ratio from the extraction of the radiation length.

current π^0 result is normalized to the published data (the conversion probability is not needed for R_γ, but is needed to measure an invariant yield). The main concern here is with shape differences for this comparison. The radiation length, X/X_0, is extracted in each centrality bin. The extracted value in each centrality bin is shown in Table 4.3. Consistency between each centrality bin is observed. The average value and standard deviation are found to be $\langle X/X_0 \rangle = [3.21 \pm 0.21]\,\%$, in reasonable agreement with the material budget [42]. The global uncertainty from this extraction is expressed in Fig. 4.18 as the blue band. This number is used to normalize all of the results shown in Fig. 4.18. The π^0 invariant yield results are consistent within systematic uncertainties.

Centrality [%]	$X/X_0[\%]$
0 - 20	2.88 ± 0.85
20 - 40	3.19 ± 0.75
40 - 60	3.55 ± 0.90
60 - 90	3.23 ± 0.11
Min. Bias	3.22 ± 0.53

Table 4.3: A table showing the extracted radiation length sampled by normalizing the external conversion pion invariant yield to the published result [26]. The radiation length is extracted in each centrality bin.

The full correction for the pion yield in each centrality bin is shown in Fig. 4.19. A 9^{th} order polynomial is used to parameterize the correction. The correction is factorized into each component of the acceptance and efficiency from each cut. This is shown in Fig. 4.20 for the Minimum Bias centrality bin. Again, note that this correction does not include the conversion probability. A further correction is applied to account for occupancy effects in the charged particle tracks and RICH detectors. This has been evaluated in a separate charged track embedding simulation. The corresponding corrections are 0.6, 0.76, 0.84, 0.93, 0.68 for the 0-20%, 20-40%, 40-60%, 60-90%, and MB centrality bins respectively. The systematic uncertainty on the occupancy correction is estimated as 5%.

Pion Tagging Correction $\langle \varepsilon_\gamma f \rangle$

Now that the validity of the simulation has been demonstrated, the correction of interest to R_γ, $\langle \varepsilon_\gamma f \rangle$ is shown. The product of the efficiency and acceptance corrections is calculated from a single ratio, the ratio of all pion decay tagged converted photons to all converted photons reconstructed. The corrections for each centrality selection are shown in Fig. 4.21. A Fermi function can be used

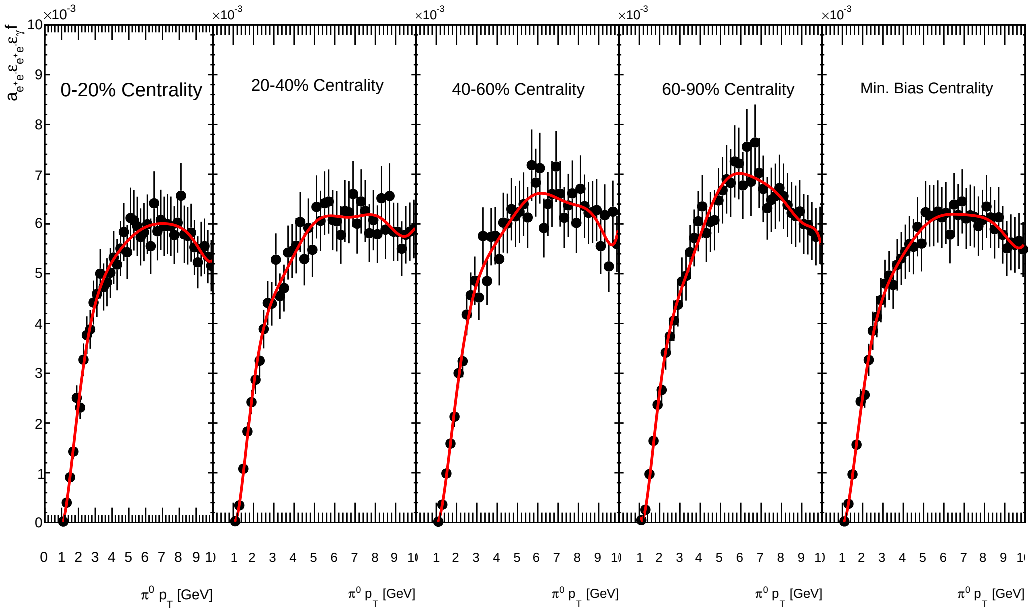

Figure 4.19: The full pion acceptance and efficiency correction, $a_{ee}\varepsilon_{ee}a_\gamma f$, as a function of p_T in each centrality bin.

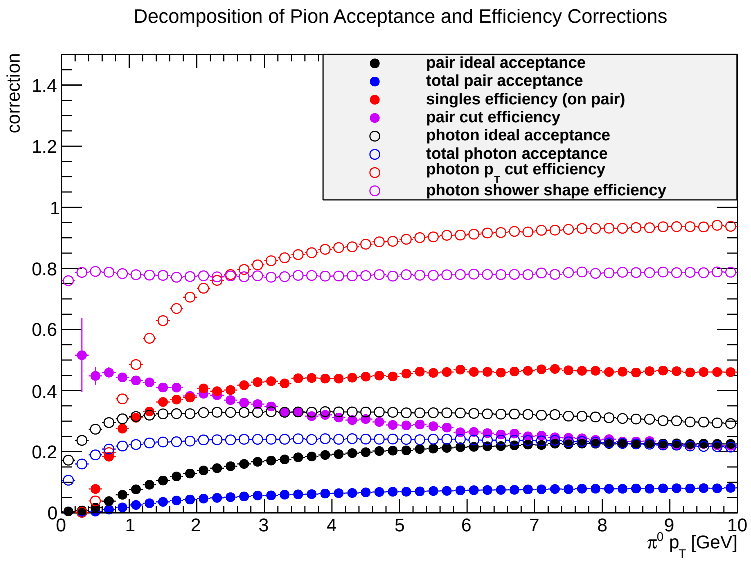

Figure 4.20: A break down of the efficiency of each cut on the π^0 counting, along with the acceptance factors. All the solid points pertain to the converted photon efficiency and acceptance. The open points pertain to the unconverted Emcal photon. In the legend, "inside PHENIX acceptance" means the acceptance within the PHENIX central arms (not including dead areas). "total acceptance" additionally includes losses due to detector dead areas.

to parameterize and thus smooth out fluctuations in the points (red curves in the figure).

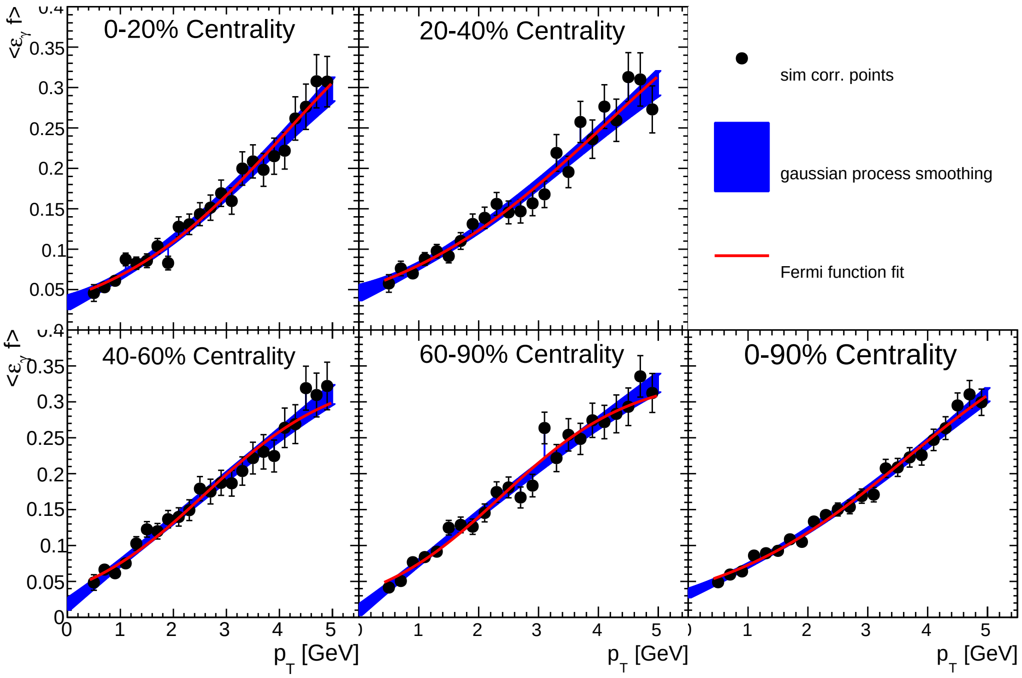

Figure 4.21: The pion tagging efficiency and acceptance correction, εf, for each centrality bin. Both the Fermi function fit and Gaussian Process (GP) regression analysis parameterizing the correction is shown. The GP procedure is ultimately chosen to smooth the correction.

Another method of parameterization is ultimately used, which does not require the assumption of a particular shape (it is actually less of a parameterization method, and more of an interpolation or regression method). This method does a better job describing the simulation points at low momentum and reduces the systematic uncertainties compared to the Fermi function parameterization. The method used for the parameterization is the Gaussian Process (GP). The procedure in [52] is followed. The smoothing from the GP analysis is shown by the shaded blue line in Fig. 4.21. The GP essentially fills in points (to an arbitrary level of fineness) in between the actual data points supplied to the regression. Because the whole analysis is based on Gaussian distributions, the error on each interpolated point can be calculated and is shown by the blue shading in Fig. 4.21.

Care was taken in the photon counting (for the second, non-HBD conversion, leg of the pion decay) to additionally include photons that externally convert close enough to the Emcal that the e^+e^- from the conversion hit the Emcal in the same spot and thus are reconstructed as a single photon. These types of photons are denoted late conversions. The counting was considered separately to study the effect. Fig. 4.22 shows the π^0 mass distribution for pions reconstructed with an unconverted second leg photon compared with pions reconstructed with a late conversion for the second leg photon. A pion peak can still be seen with the late conversions. Fig. 4.23 shows the radial distribution of photon conversions in the simulation. Also shown in the figure is the distribution for late conversions. As can be seen, conversions with a radius greater than 250cm generally have the dielectrons forming a single cluster in the Emcal.

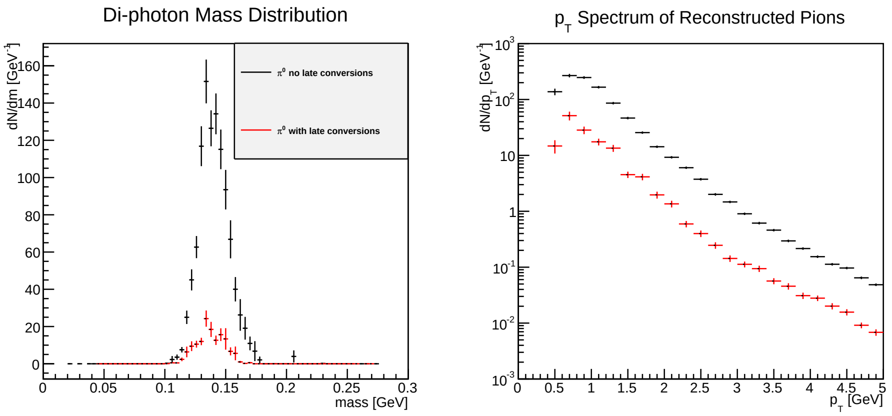

Figure 4.22: Left: The mass distributions of reconstructed pions within the simulation. The black points represent pions reconstructed with the second photon measured directly in the Emcal. The red points represent pions reconstructed with the second photon converted before the Emcal. Right: The p_T distributions for each case.

4.2.5 Systematic Uncertainties

An overview of the PHENIX convention for quoting systematic uncertainties is first presented. There are three types of uncertainties considered, Types A, B, and C. Type A uncertainties are defined as uncertainties that are uncorrelated point to point. This means that each point can move independently by their uncertainty. The type A uncertainties are added in quadrature with the statistical errors. These are plotted as lines associated with the points.

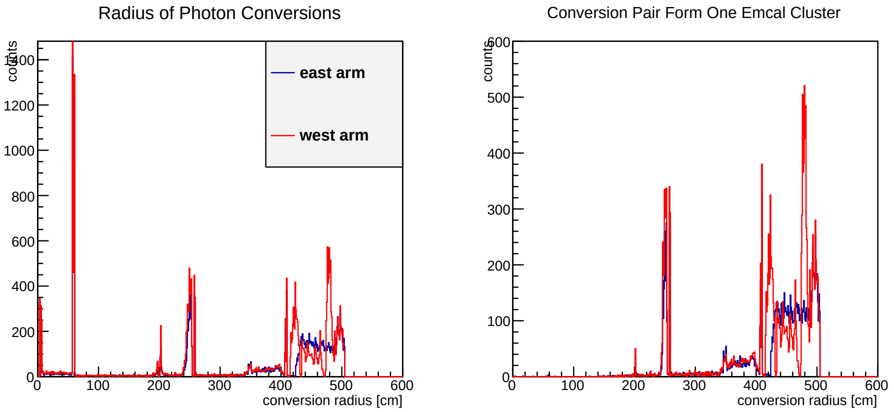

Figure 4.23: Left: A histogram of the radius of conversion of photons in material in PHENIX. The two arms are separated by color as the material budget is different for the two arms. Right: A histogram of the radius of conversion of photons in material where the conversion pair forms a single cluster in the Emcal (so called late conversion). As can be seen, this occurs only if the conversion occurs at a radius greater than 250cm.

Type B uncertainties are correlated point to point in some way. These are commonly plotted as a shaded box around each point. Type C uncertainties are uncertainties on the overall scale and so will shift all the data points up or down by the same amount. These are typically plotted as a separate band on the plot. The PHENIX convention is followed in this thesis.

There are many sources of systematic uncertainty considered in this analysis. They are summarized in Table 4.4 below. The uncertainties are summarized in a plot in Fig. 4.24. Each source is discussed in more detail in this section. All the type B uncertainties originate from multiplicative factors to form R_γ and so all relative uncertainties are added in quadrature to get the total systematic on R_γ.

Error source 1: Systematic on π^0 yield extraction

One source of systematic uncertainty is on the extraction of the π^0 tagged photons and on the background subtraction. This is considered a type A systematic as the origin is largely based on the available statistics in the sample. The π^0 tagging method is discussed in Section 4.2.2. This systematic uncertainty is estimated by extracting the π^0 yield with different background normalizations. In addition, the yields are calculated by either directly counting the bins or integrating the Gaussian fit. Three different background normal-

Table 4.4: Systematic uncertainty on R_γ for min. bias centrality

Source	Systematic Error [%]	Type
π^0 Extraction	4	A
ε	1	B
f	1	B
Energy Scale	4	B
εf Parameterization	$\sim$2	B
Conversion Contamination	1	B
Conversion Correction	2	B
Simulation Ratio	2.5	B

ization functions are used. The FG/BG ratio is fit with a constant and a first order polynomial, in addition to the second polynomial used for the analysis. The deviation of each counting method to the standard used in the analysis (2^{nd} order polynomial normalization with counting the bins directly) is taken as the systematic error. This systematic error is added in quadrature to the statistical errors. The systematic uncertainty as a function of p_T is shown for each centrality in Fig. 4.25. Much of the deviation is due to statistics (at high p_T there is almost no background, the systematic uncertainty on the background subtraction cannot be large there). Therefore, a systematic uncertainty of 4% is taken independent of p_T and centrality, which includes roughly one standard deviation (68%) of the points inside the 4% band.

Error source 2: Systematic on the photon reconstruction efficiency in the Emcal, ε_γ

The uncertainty of the photon reconstruction efficiency in the Emcal, (ε_γ), is studied by looking at the correction calculated from simulation with various χ^2 cuts, showing how sensitive the correction is to the specific cut. Fig. 4.26 shows the single photon Emcal reconstruction efficiency for the various χ^2 cuts in the left panel for MB events. The colors represent each alternate cut as described in the legend. The right panel in the figure shows the ratios of each efficiency to the ratio with the nominal $\chi^2 < 3$. Other centralities are not shown, but have the same dependence. Only the PbSc is shown, because the majority of statistics is collected in the PbSc. The PbGl has an even higher efficiency, and so the systematic uncertainty should be even smaller than for the PbSc. The efficiency is not terribly dependent on the cut used. As can be seen a variation of about 1% is seen for a reasonable deviation from the cut. Therefore we estimate the systematic error due to the photon reconstruction

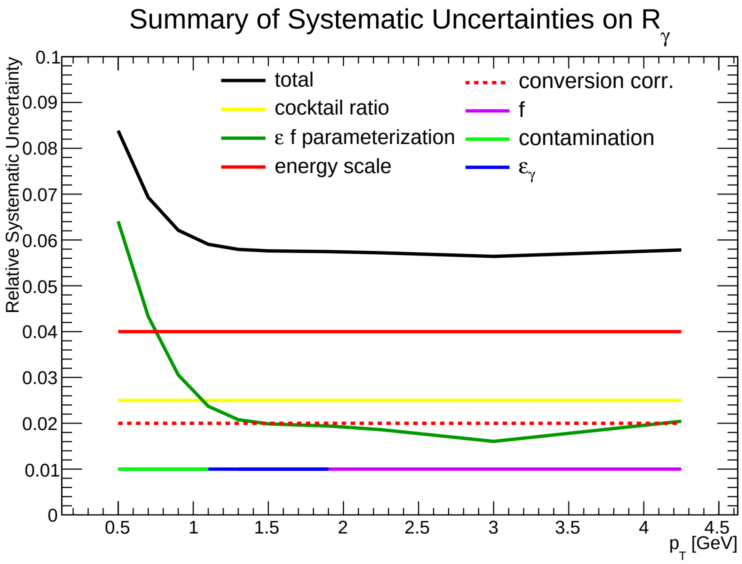

Figure 4.24: A summary plot of the type B systematic uncertainties on R_γ.

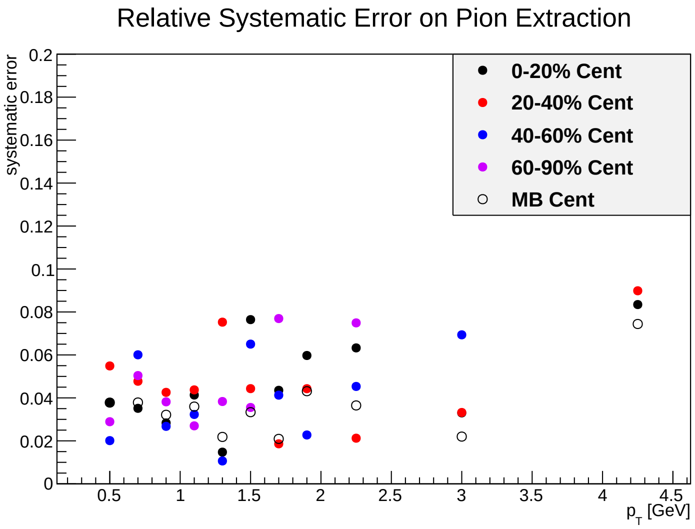

Figure 4.25: The type A systematic uncertainty associated with the extraction of the pion yield.

efficiency to be 1%.

The analysis is additionally redone with a tighter $\chi^2 < 2.5$ cut. The comparison is shown in Fig. 4.27 as a ratio of the calculated R_γ with each cut and further supports the small 1% uncertainty.

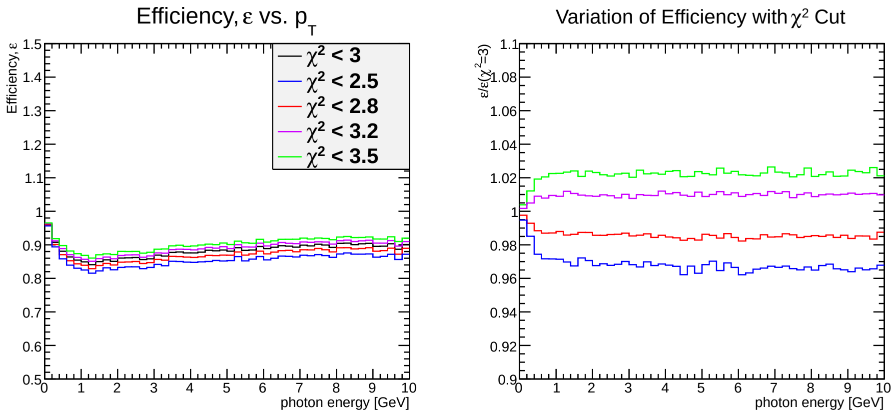

Figure 4.26: A study to estimate the systematic uncertainty of the photon reconstruction efficiency in the Emcal. The left plot shows the efficiency as a function of p_T for the PbSc sectors in MB events. for various cut values. The right plot shows the ratio of each efficiency from an alternate cut to the efficiency with the nominal cut of $\chi^2 < 3$.

Error source 3: Systematic on the conditional acceptance

There is a systematic uncertainty associated with the conditional acceptance (the f in $\varepsilon_\gamma f$ of Eqn. 4.6). The main contributor to this systematic uncertainty is the match of the deadmap in the Emcal between simulation and data. The match between simulation and data has been considered and quantified in Figs. 4.28 and Fig. 4.29. Fig. 4.28 shows the tower hit map in each Emcal sector in simulation (left) and data (right). The deadmap includes a mask on dead and hot towers as well as a fiducial on an area of 3x3 towers around the dead/hot channel to avoid loss/distortion of signal from a photon depositing part of its energy into a dead tower. Clusters with a center on these edge towers are rejected. Fig. 4.29 calculates the percent masked towers in each sector in simulation and data and plots the ratio. The average of the percent difference between the dead area in simulation and data over the sectors is used to estimate the systematic uncertainty on the conditional acceptance as 1.%. The dead maps average over all runs and so account for some of the run by run variation of the live area of the detector (combined with the quality

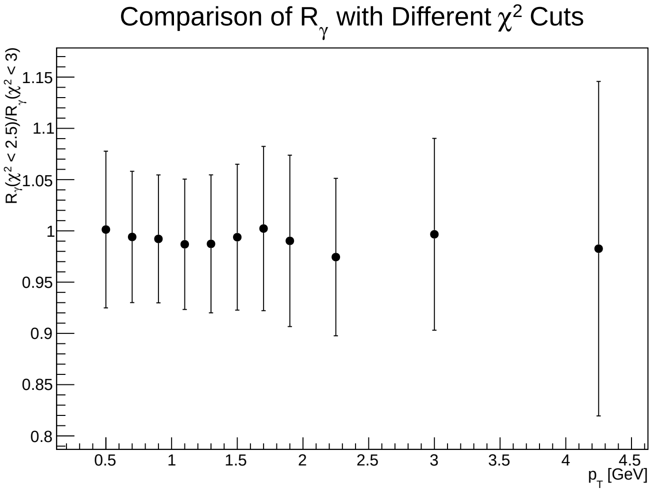

Figure 4.27: The ratio of R_γ calculated with a $\chi^2 < 2.5$ to $\chi^2 < 3$.. The results are nearly identical.

analysis of rejecting bad events discussed in Sec. 4.1).

Error source 4: Energy Scale

Another systematic uncertainty comes from the energy scale of the photons in the Emcal. This is related to the energy cut off of clusters accepted as photons. A mismatch in the energy scale between simulation and data will lead to the simulation having an incorrect pion tagging efficiency. As shown in Fig. 4.16, the π^0 peak differ by about $1.5 - 2\%$ in simulation and data. So 2% is taken as the energy scale difference. Then to see the effect on the correction, the correction was calculated by taking the lower energy cut off to be $600MeV \pm 2\%$. The corrections are then compared. This is shown in Fig. 4.30. From the spread of the points, the systematic uncertainty from the energy scale is taken to be 4%.

Error source 5: Systematic from the Smoothing of the Correction

Next the systematic uncertainty introduced from the smoothing of the correction is investigated. The true shape that $\varepsilon_\gamma f$ follows is not known. A Fermi function, $\langle \varepsilon_\gamma f \rangle = C \cdot \left(a + e^{bp_T}\right)$, can be chosen to smooth out the statistical fluctuations from the low statistics simulation. A Fermi function is commonly used parameterize efficiency curves. Several fits are performed to estimate the systematic uncertainty from the smoothing. A fit to the full simulation statistics is compared to a fit done with a half statistics sample. This is to test a

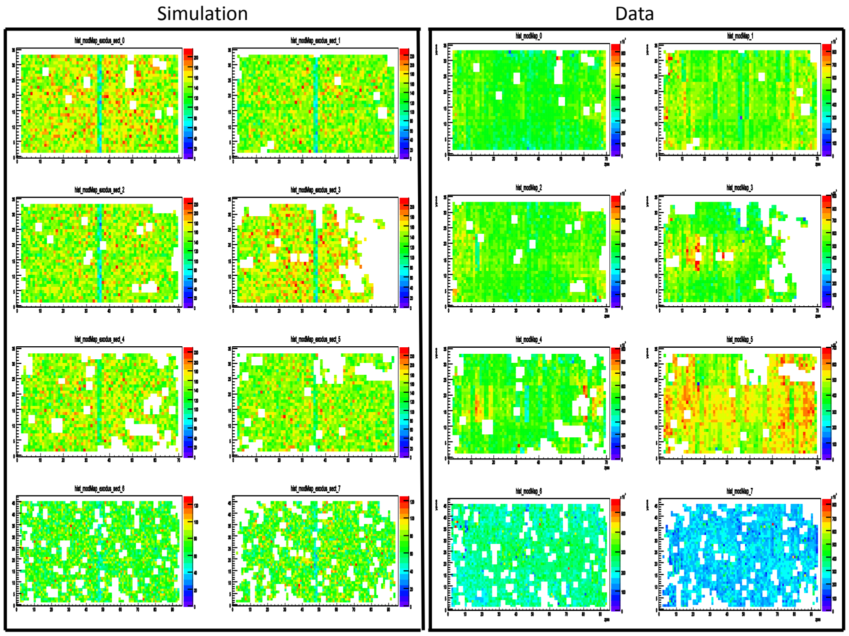

Figure 4.28: The comparison of the Emcal hit maps in simulation (left) and data (right).

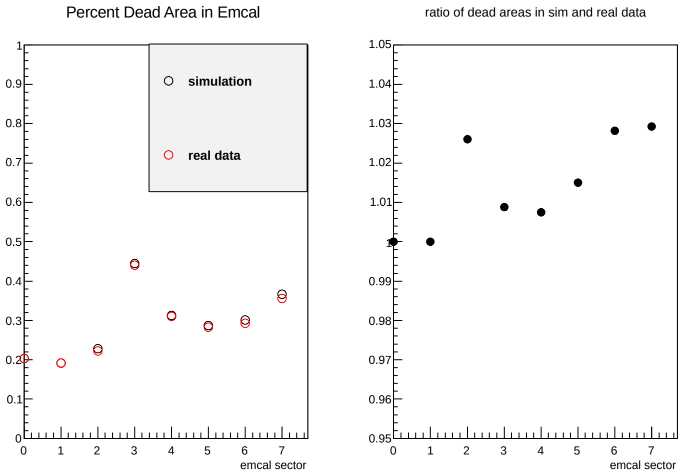

Figure 4.29: Left Plot: The percent masked area in each sector in simulation and data. Right Plot: The ratio of the percent dead area in simulation and data.

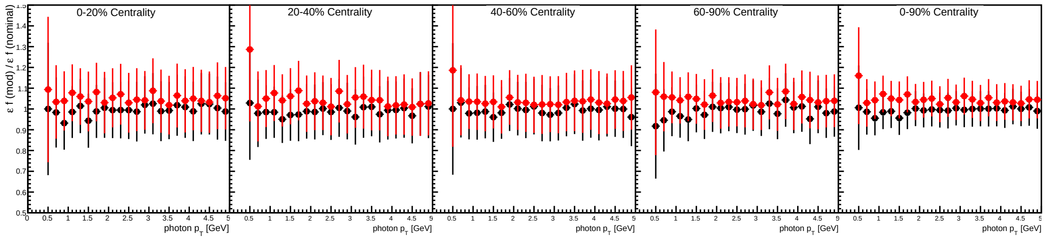

Figure 4.30: The systematic uncertainty of the energy scale mismatch in data and simulation shown in each centrality bin as a ratio of the correction with the energy cut off up and down by 2% to the correction with the nominal energy cut. A flat ratio of 4% is taken as the systematic uncertainty independent of p_T and centrality.

possible systematic difference to the parameterization because of simulation statistics. A second set of simulated events was also produced (with about half the statistics of the original simulation) to add to the total number of independent measurements. The systematic effects the statistics has on our parameterization is studied in this way.

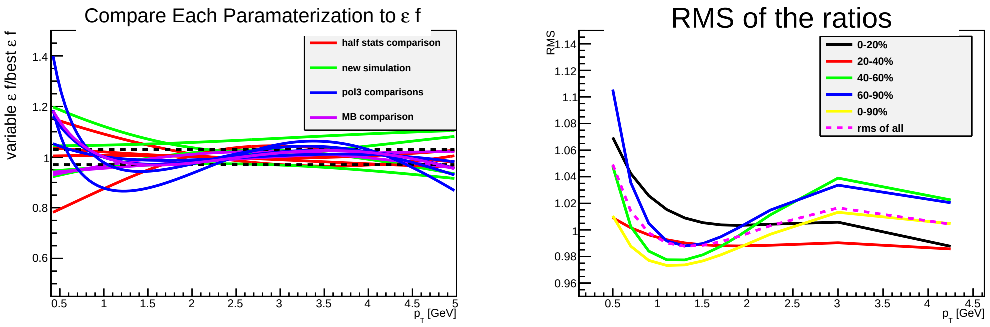

Figure 4.31: Left Panel: The ratio of the variable correction to the base line correction, testing the systematic uncertainty of the fit parameterization. Right Panel: The RMS of the ratios on the left.

In addition, a different parameterization function is applied, a third order polynomial. The results of each fit to the simulation data are shown in Fig. 4.31, expressed as the ratio of the varied condition parameterization to the base line, best statistics parameterization. All centralities are drawn together and are not distinguished by color, with the exception of the MB bin shown in violet. The systematic uncertainty should not be centrality dependent and so the spread among all centralities is considered and assigned as a centrality independent systematic uncertainty from the smoothing of the correction. The RMS spread of each of the fits at each data point to the baseline measurement is calculated (right plot in 4.31). It is observed that the uncertainty is dependent on the momentum (since the ends of the fits are the most unconstrained). The assigned systematic uncertainty is 6% for the first 400-600 MeV p_T bin, and roughly 2% for all other p_T bins.

The above method is cross-checked and replaced with an improved method of smoothing which does not assume a functional form. This is the Gaussian Process method discussed in Sec. 4.2.4. The Gaussian process method gives more reliable results at the extreme ends of the measured range. The comparison of the Fermi function fit and the Gaussian process smoothing is shown in Fig. 4.21 by the red line and the blue shaded curve respectively.

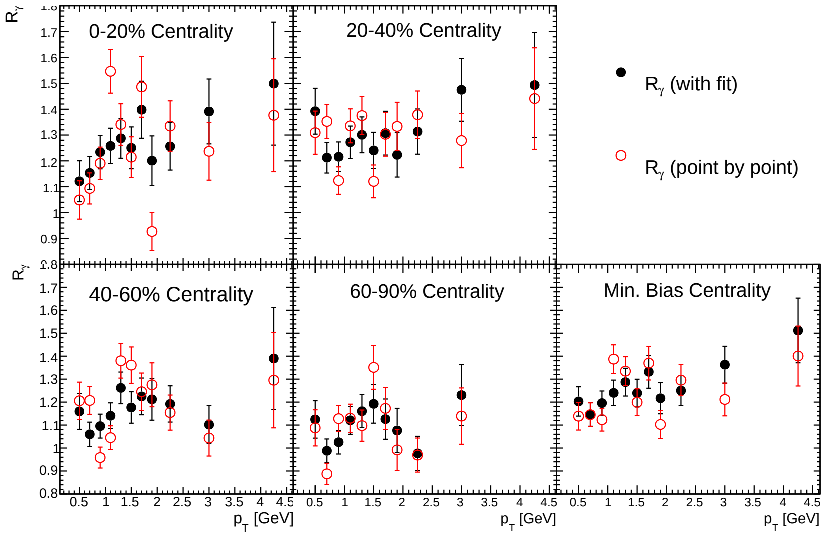

Figure 4.32: The comparison of R_γ calculated with the parameterization of the correction (black points) and applying the correction point by point (red points).

The difference between R_γ calculated with the Gaussian process smoothing and the correction applied point by point is also plotted. This is shown in Fig. 4.32. Of course the calculation using the point by point correction has large statistical fluctuations, but the point here is to look for any systematic shift in the result based on the use of the smoothing. The ratio of the two results for each centrality is shown in Fig. 4.33 and fit with a flat line. The typical fit for each centrality is a systematic shift of 3%. This is in line with our earlier estimate. The ratios are also fitted excluding the first two points, with the apparent systematic shift dropping to $1 - 1.5\%$. In the end, the blue error band on the gaussian process smoothing in Fig. 4.21 is taken as the systematic uncertainty on $\langle \varepsilon_\gamma f \rangle$ due to the smoothing of the correction, since it is consistent with all other tests.

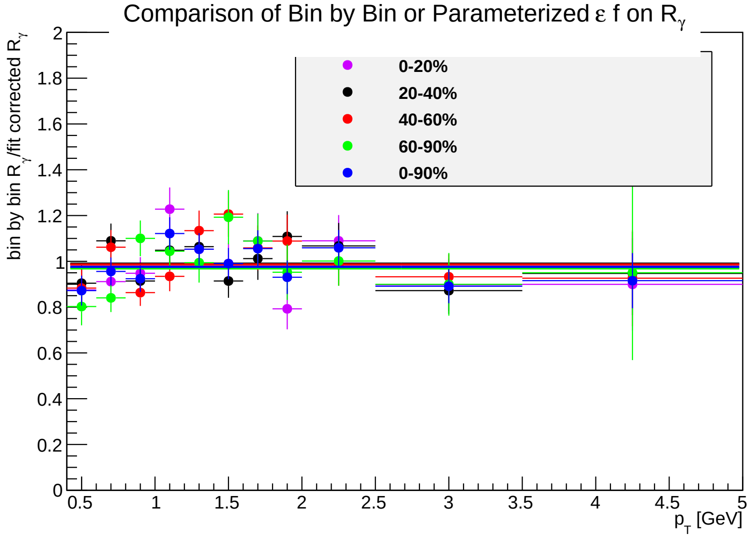

Figure 4.33: The ratios of the bin by bin corrected R_γ to the parameterized correction calculated R_γ for each centrality. Also shown is a straight line fit to each ratio.

Error source 6: Systematic from Contamination of Photon Sample

Here we consider the systematic uncertainty associated with contamination in our converted photon sample. Other sources of conversions can contaminate the conversions from the HBD shell. This is of little importance because the conditional acceptance correction is only very slightly dependent on the radius of conversion. The contamination is studied in a MC simulation. Photons are generated and fed into PISA. Fig. 3.11 shows the ATM mass vs. normal mass for different conversion radii. The relative yields from each conversion source is directly generated by PISA (i.e. a bunch of photons are thrown into PISA, and PISA converts as required). The point of the plot is to show that conversions not from the HBD backplane live in a different place than the HBD backplane conversions in the space of the cut. The contamination from other conversions is estimated to be 1% (mainly from the CF_4 radiator gas inside the

HBD, since it is closest to the backplane). This is actually an overestimate, because external conversions from another radius are still signal (but have a very slightly different conditional acceptance). The contamination from π^0 Dalitz decays is similar. The estimate for the systematic uncertainty on the purity of the converted photon sample is 1%. The combinatorial background is not explicitly subtracted, but it is very small in this extremely low mass region and is less than 1% after cuts.

In contrast to the Emcal only analysis [30] where there is a large contamination (about 20%) of hadrons (mostly neutrons) being identified as photons, the external conversion analysis virtually eliminates this source of contamination.

Error source 7: Conversion Correction

A systematic uncertainty is placed on the accuracy of the material budget in the simulation. An inaccurate budget in the simulation will cause the pion tagging correction to be miscalculated, due to a different loss of pion tagging than actually happens in real data from the loss of the second leg of the photon due to a conversion (i.e. both photons from a π^0 decay convert and thus are lost in this analysis). Additionally some of these photons actually can be reconstructed as a photon if the conversion happens close enough to the Emcal (as discussed in Sec. 4.2.4). This is evaluated from the full Monte Carlo simulation and is estimated as 2% on R_γ as in previous photon analyses.

Error source 8: Systematic on the Cocktail Ratio

There is an additional systematic uncertainty on the denominator of the R_γ double ratio of Eqn. 4.6, with multiple contributing sources to the uncertainty. One is the uncertainty in the input pion spectral shape used in the simulation. Another uncertainty stems from the uncertainty in the meson to pion ratios that are input into the simulation from measurements. Lastly we can consider an uncertainty on the m_T scaling assumption used to determine the spectral shape of the mesons heavier than the pion.

The uncertainty on the input pion spectral shape is estimated to be small and negligible (less than 1%). One calculation done to estimate this is using different spectral shape parameterizations. In addition to the modified Hagedorn used for the analysis (as discussed in Sec. 4.2.3), A Tsallis functional form has also been used to calculate the cocktail. These parameterizations have been taken from [53]. Fig. 4.34 shows the percent difference of the cocktail ratio from the two parameteizations for the 0-20% centrality selection. The case is the same for other centrality bins.

To additionally test the shape parameterization, the pion data points are

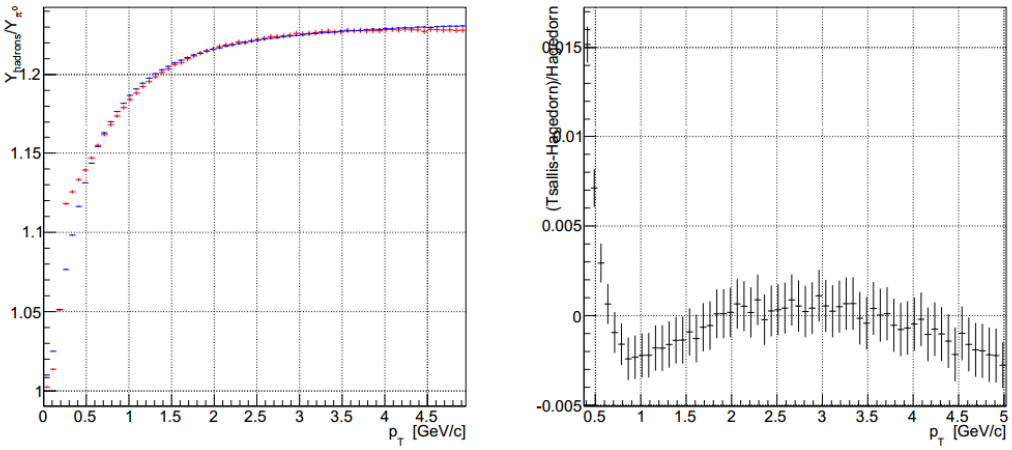

Figure 4.34: A comparison of the cocktail ratio with the input pion shape parameterized by a modified Hagedorn and a Tsallis function.

also shifted up and down by each points respective systematic uncertainty and the fits used for the pion shape in the cocktail are redone. The cocktail ratio is then recalculated with these alternate parameterizations, showing the same $< 1\%$ deviations if one used the alternate parameterizations.

Now consider the systematic uncertainty associated with the uncertainties from the meson to pion ratios. This is calculated by recalculating the cocktail ratio with the meson to pion ratios shifted fully up and down by each species respective measurement uncertainty quoted in the publications listed in Sec. 4.2.3. The relative uncertainty, expressed as the percent difference in the cocktails, is shown in Fig. 4.35. This uncertainty is dominated by the uncertainty of the η/π^0 ratio of $\sim 3\%$ [47].

Lastly any uncertainty in the m_T scaling assumption is considered, which is studied by comparing the measured η/π^0 [47] with the same ratio calculated from the parameterization used as input to the cocktail. Fig. 4.36 shows the η/π^0 ratio from parameterizations used as input to the cocktail compared to published data and Pythia. The agreement looks good. There is no data below 2 GeV to constrain/verify the calculation. An extreme assumption has been made to test the sensitivity of the shape of this ratio at low p_T, that the η/π^0 ratio is flat all the way down to 0GeV in p_T. The resulting cocktail ratio is shown in Fig. 4.37. The difference is less than 2% at high p_T as expected, but can be large (up to 7% for our lowest p_T bin). Since this represents an extreme assumption, this is a gross overestimate for the systematic uncertainty.

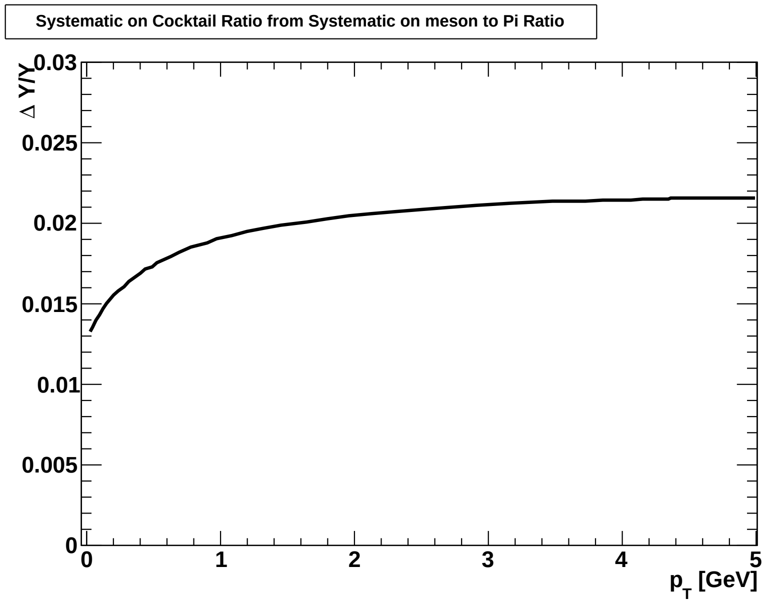

Figure 4.35: The systematic uncertainty on the cocktail ratio originating from the uncertainty on the meson to pion ratios input into the simulation.

Taking all of the above information into account, a systematic uncertainty on the cocktail ratio of 2.5% is assigned independent of p_T for each centrality bin.

4.3 Invariant Yield of Direct Photons

The invariant yield of direct photons is calculated from R_γ and the invariant yield of hadron decay photons calculated from the cocktail discussed in Sec. 4.2.3 and thus is calculated via Eqn. 4.5. The systematic uncertainties to this measurement are discussed in the following subsection, Sec. 4.3.1.

The direct photon invariant yield is also calculated via Eqn. 4.3 with R_γ and the corrected measured inclusive photon invariant yield as a cross-check. The discussion of the corrected inclusive photon invariant yield used for this calculation is also discussed later in this section, see Sec. 4.3.2.

4.3.1 Systematic Uncertainties

The systematic uncertainty on the direct photon invariant yield is dominated by the systematic uncertainty on the hadronic cocktail. The systematic on R_γ has already been discussed in detail in Sec. 4.2.5. The cocktail used has

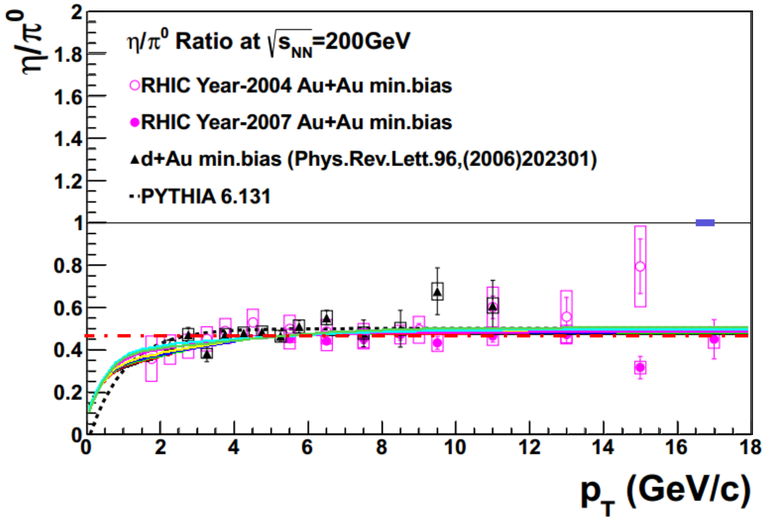

Figure 4.36: The comparison of the η/π^0 ratio from the cocktail (various colored lines for each (10%) centrality bin with published data from [47] as shown in the legend. The dotted black line represents the calculation from Pythia as described in [47]. Also shown is the flat line extrapolation of the ratio used in Fig. 4.37 in the dashed dotted red line.

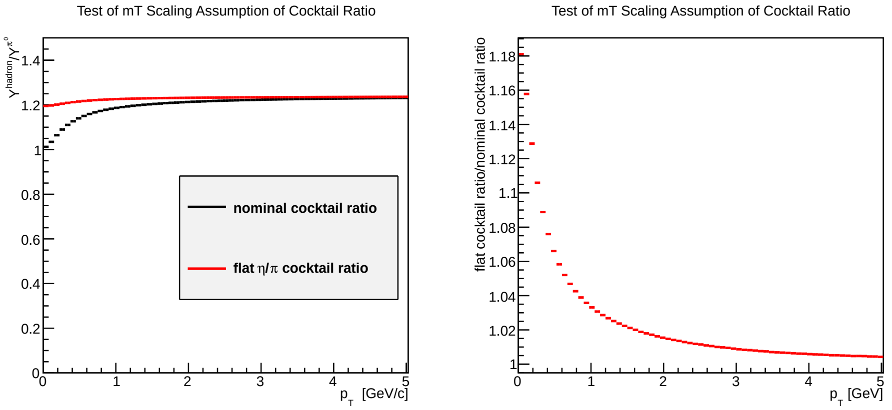

Figure 4.37: The effect of the η/π^0 ratio on the cocktail ratio is studied. The left plot shows the two cocktail ratios. The right plot shows the ratio of the cocktail ratios.

already been studied in [28]. The systematic uncertainty estimate from that analysis is taken for this thesis. The systematic uncertainties are shown in Fig. 4.38. Each source is added in quadrature to get the total uncertainty on the cocktail. Each component in the figure is detailed in the next subsections.

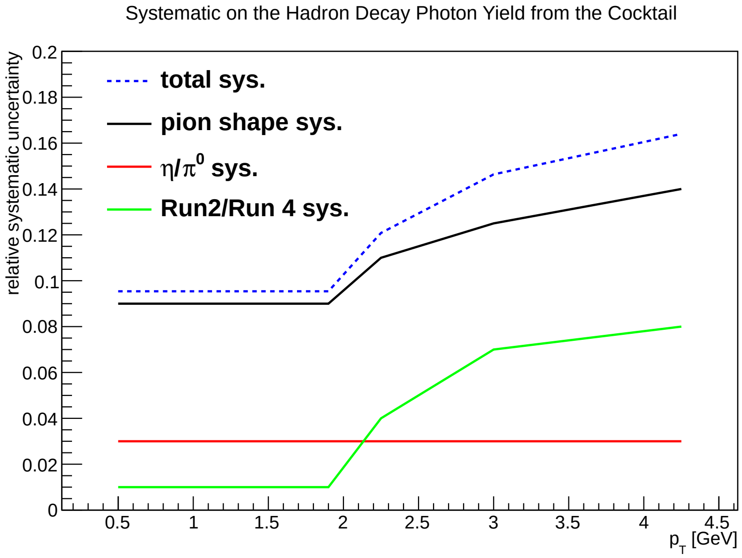

Figure 4.38: A summary plot of the systematic uncertainties on the cocktail in the minimum bias centrality selection. Each color is described in the legend and text.

Systematic from Uncertainty in Pion Shape

A systematic uncertainty is studied pertaining to the shape of the pion spectrum used as input to the cocktail. This is the dominant source of systematic uncertainty on the yield. This is represented by the black line in Fig. 4.38. This is calculated by refitting the pion data with the data points moved fully up or down by each points systematic uncertainty. These new parameters were then used to recalculate the cocktail. The difference in cocktail is taken to be the systematic uncertainty.

Systematic from Run 2/Run 4 Discrepancy

The input pion spectral shape is determined by using the charged pion results [45] along with the Run 2 [46] and Run 4 [25] neutral pion spectra. A systematic shift between the Run 2 and Run 4 π^0 invariant yields is observed, see Fig. 4.7. Any uncertainty from this discrepancy is accounted for in cocktail uncertainty by performing the fits with the charged pion data with only the Run 2 or Run 4 data and then recalculating the cocktail. The systematic due to this is shown by the green line in Fig. 4.38.

Meson to Pion Ratio Uncertainty

The meson to pion ratios used to normalize the meson yields have an associated uncertainty with them from the measurements. The uncertainty on the cocktail due to these uncertainties are estimated by rerunning the cocktail with different ratios bracketed by the uncertainty on the ratio measurement. This has the biggest effect with the η/π^0 ratio, since the η meson is the next largest source after the pion (but still a small portion of the total, roughly 10%). This is shown by the red line in Fig. 4.38. The other mesons in the cocktail contribute a small portion of the yield and so these uncertainties on the cocktail are less than 1% (and hence not drawn in Fig. 4.38).

4.3.2 The Corrected Inclusive Photon Invariant Yield

The correction to the inclusive photon invariant yield, $\varepsilon_{e^+e^-}a_{e^+e^-}$ is discussed in this section. The framework for the simulation used for the calculation of the correction has already been discussed in Sect. 4.2.4. Single converted photon simulations are performed under the simulation framework. The occupancy correction is accounted for separately, as was done in Sec. 4.2.4. The full correction folds in the acceptance and pair efficiency into one correction. The ratio of the number of reconstructed pairs to the total number thrown into the simulation gives the full correction. The correction (and thus the direct photon yield cross-check) is only performed in the MB centrality bin. The p_T weighting is determined by parameterizing the the decay photon spectrum from the cocktail of Sec. 4.2.3. This is not a true depiction of the spectral shape, since this parameterization does not include the direct photon yield (which as R_γ shows is roughly 20% above the decay photon yield), and may distort the correction slightly. The correction is shown in the left panel of Fig. 4.39. As is done in Sec. 4.2.4, the conversion probability is applied as a separate factor. The same value found from the pion analysis in 4.2.4 is taken, $\langle X/X_0\rangle = [3.21 \pm 0.21]\%$.

The correction is applied to the raw inclusive spectra in Fig. 4.2 to obtain the fully corrected per event invariant yield of inclusive photons, shown in the right panel of Fig. 4.39. The data points are tabulated in Table A.6.

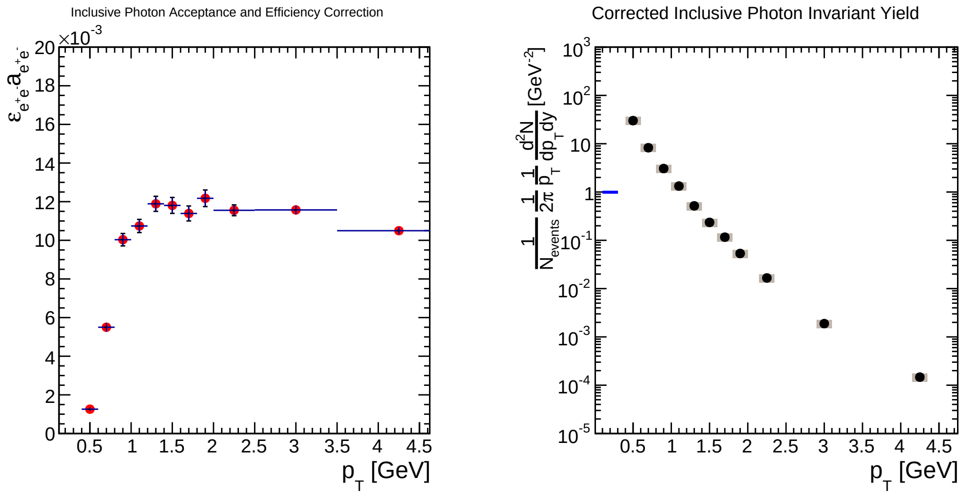
Inclusive Photon Acceptance and Efficiency Correction

Corrected Inclusive Photon Invariant Yield

Figure 4.39: Left: The acceptance and efficiency correction on the inclusive photon yield. Right: The corrected inclusive photon invariant yield. The blue box indicates an overall scale uncertainty due to the conversion probability of 6%. The data is tabulated in Table A.6. The result is shown for the minimum bias centrality selection.

Chapter 5

Results: Direct Photon Invariant Yield

5.1 Results: R_γ

R_γ is calculated from Eqn. 4.6 and discussed in Sec. 4.2. The raw yield ratios ($N^{incl}/N^{\pi^0 tag}$) that go into the numerator of the double ratio are shown in Fig. 5.1 for each centrality selection. The same ratio is shown for minimum bias collisions in Fig. 5.2, where the comparison of the ratio for the two considered run groups with the HBD fully and half installed is made. The ratios appear to be consistent within statistical uncertainties and so justifies the merging of the two run groups into a single run group, $\varepsilon_{e^+e^-} a_{e^+e^-}$ does indeed drop out in the ratio within the precision of the measurement. Figs. 5.3 and Fig. 5.4 shows R_γ in centrality bins and the minimum bias centrality selection respectively. The data points shown in Figs. 5.3 and 5.4 are listed in Tables A.1 - A.5. Fig. 5.5 shows the integrated R_γ for various p_T ranges as a function of centrality. A weighted average is taken, with the inclusive photon yield taken as the weight.

5.2 Results: Invariant Yield

As shown in Eqn. 4.5, the direct photon invariant yield can be calculated if R_γ and the hadron decay photon invariant yield is known. This is shown in Fig. 5.6 for the minimum bias centrality selection as well as in centrality bins in Fig. 5.7. The associated data tables can be found in Tables A.7-A.11.

Fig. 5.6 also shows the comparison to the published virtual photon analysis [27] on the right panel of the figure. Fig. 5.8 makes the comparison of the 0−20% and 20−40% centrality bin direct photon yield with the same published data.

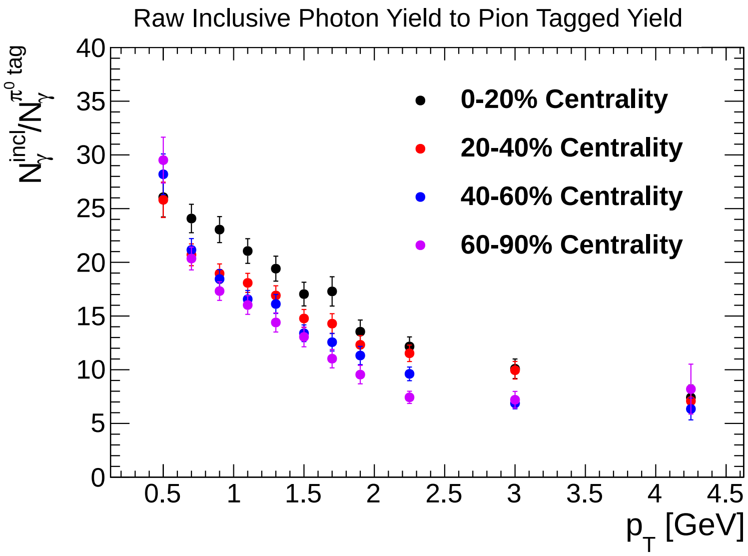
Raw Inclusive Photon Yield to Pion Tagged Yield

Figure 5.1: The ratio of the raw inclusive photon to the raw π^0 tagged photon yields for each centrality bin. This (along with $< \varepsilon_{\gamma} f$) forms the numerator of the double ratio of $R\gamma$.

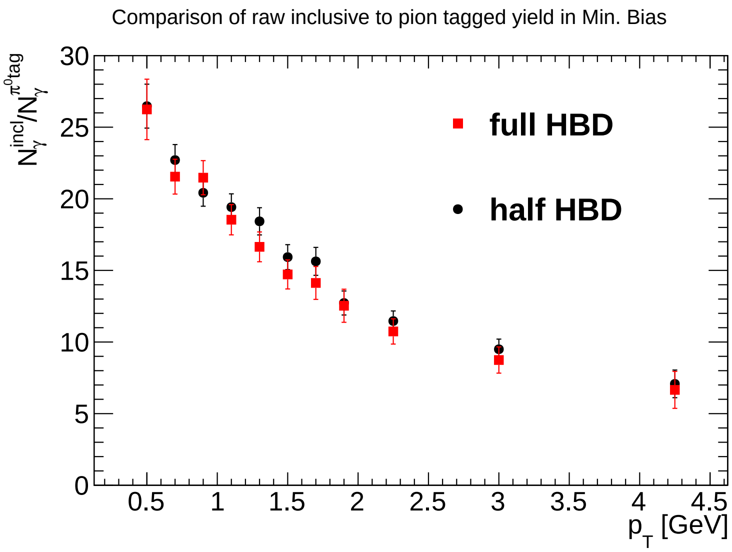
Comparison of raw inclusive to pion tagged yield in Min. Bias

Figure 5.2: A comparison of the raw inclusive to pion tagged photon yield ratio $\left(N_{\gamma}^{incl}/N_{\gamma}^{\pi^0 tag}\right)$ in the two considered run groups, with the fully installed and half installed HBD configuration.

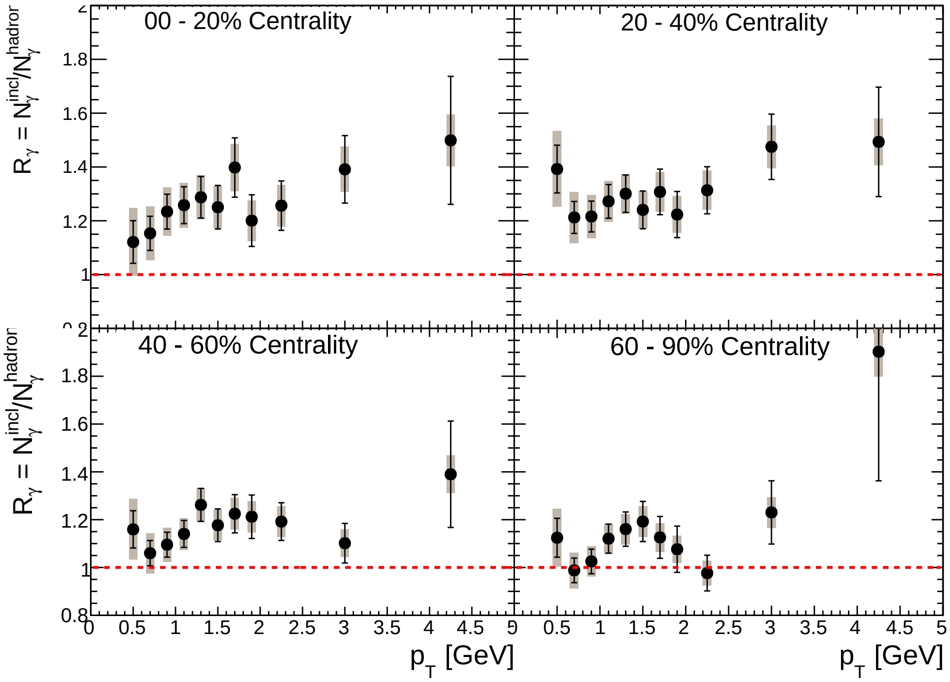

Figure 5.3: The direct photon fraction, R_γ in each centrality bin.

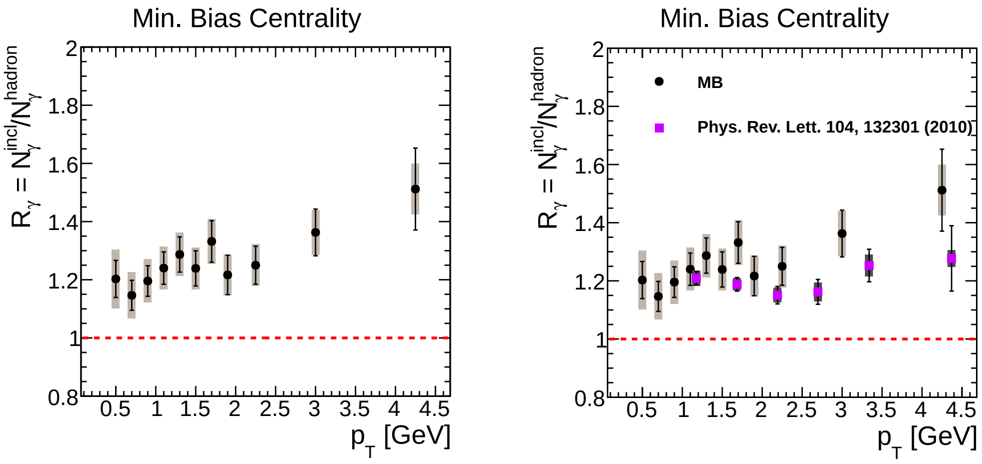

Figure 5.4: The left plot shows the direct photon fraction, R_γ as a function of p_T in the minimum bias centrality bin. The right plot compares this result with the published results [28].

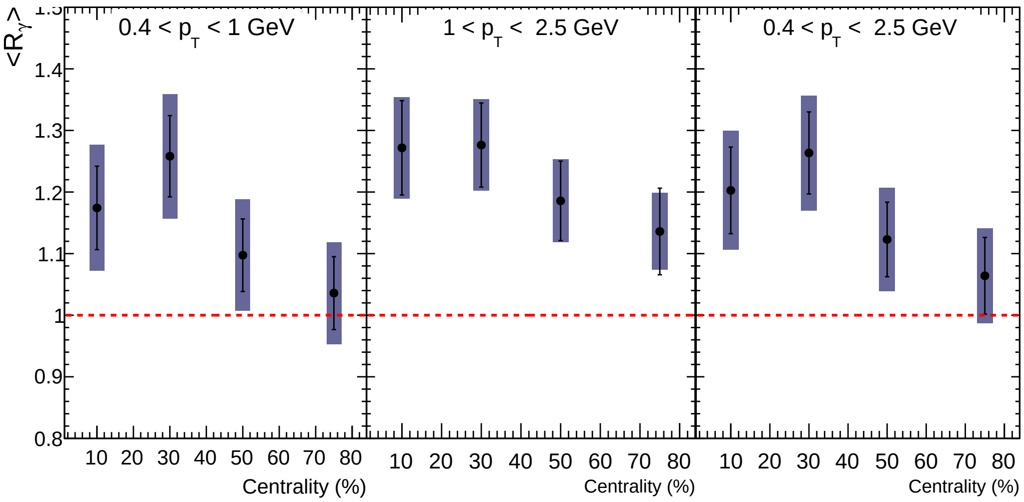

Figure 5.5: The direct photon fraction, R_γ, integrated in various p_T ranges as labeled in the plot title versus centrality.

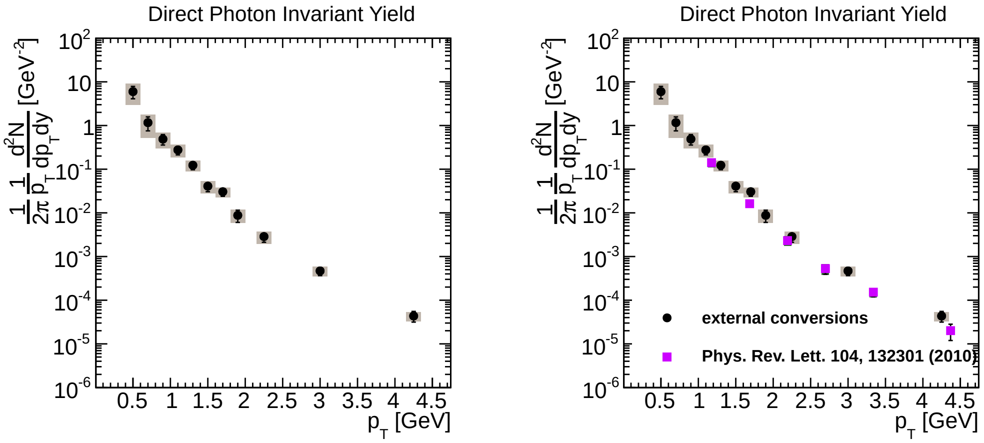

Figure 5.6: Left Panel: The direct photon invariant yield in the minimum bias centrality selection. Right Panel: The comparison of the direct photon invariant yield to previously published data [27].

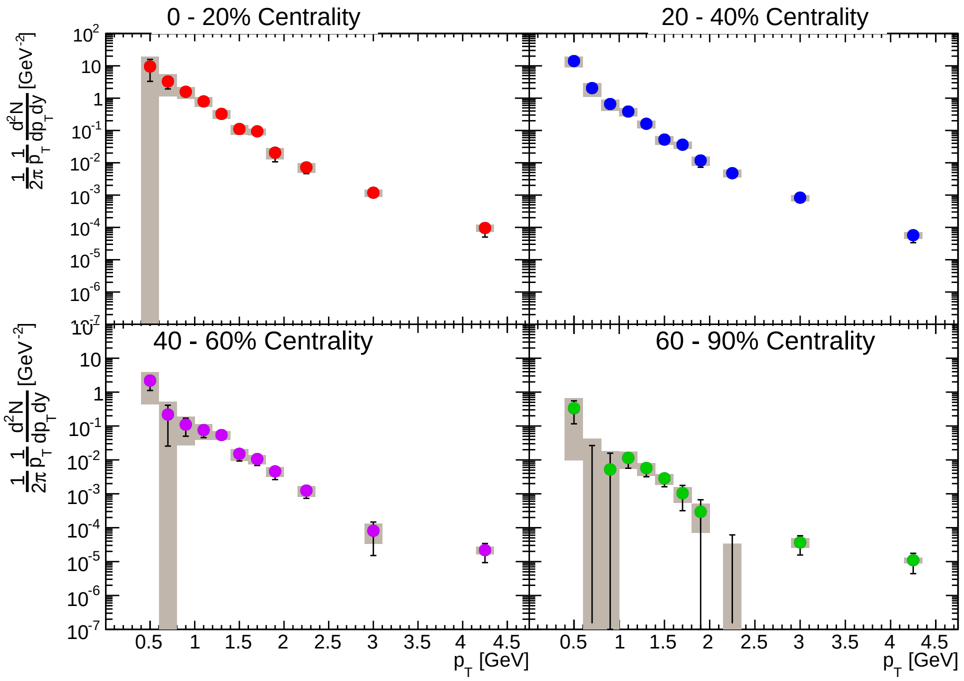

Figure 5.7: The direct photon invariant yield in each centrality bin as labeled in the figure.

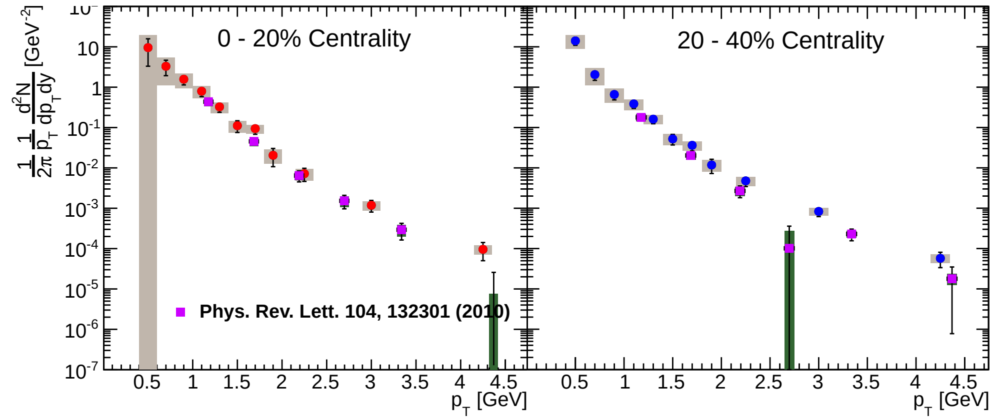

Figure 5.8: The comparison of the direct photon invariant yield to previously published results [27] for the 0-20% (left) and 20-40% (right) centrality bin.

As shown in Eqn. 4.3, the direct photon yield can also be calculated from R_γ and the measured inclusive photon yield. This measurement has large systematic uncertainties (since the pair acceptance and efficiency do not cancel as they do in the double ratio of R_γ). The comparison of the direct photon yield calculated from the corrected measured inclusive photon yield (Fig. 4.39), shown by the open red circles with the green uncertainty boxes, and the direct photon yield calculated from the hadron decay photon cocktail yield is shown in Fig. 5.9, shown by the closed black circles with the gray uncertainty box. The agreement is good and within uncertainties.

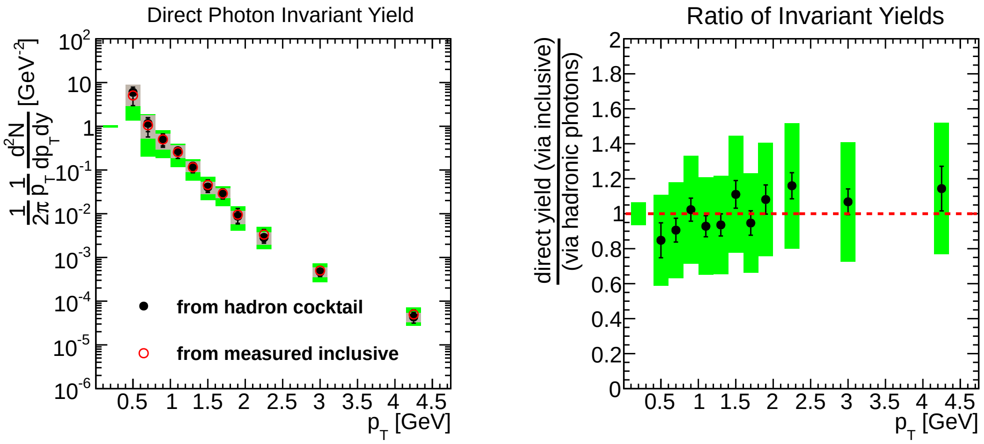

Figure 5.9: The comparison of the direct photon yields calculated with Eqn. 4.3 and Eqn. 4.5. Spectra are directly compared on the left, with the ratio of the spectra shown on the right. The green uncertainty box at low p_T represents the type C uncertainty due to the uncertainty in the conversion probability in the HBD shell.

Chapter 6

Analysis: v_2 of Direct Photons

Another interesting observation to come out of this analysis is the measurement of the elliptic flow of direct photons at low p_T. The inclusive photon v_2 and the fraction of direct photons, R_γ are measured within this thesis. If in addition the dominant source of background photons is known, then we can subtract these contributions from the inclusive photon v_2. With a little algebra, the direct photon v_2 can be calculated, knowing those three pieces of information (Eqn. 6.3).

$$v_2^{dir} = \frac{N_\gamma^{inc} v_2^{inc} - N_\gamma^{BG} v_2^{BG}}{N_\gamma^{inc} - N_\gamma^{BG}} \tag{6.1}$$

$$v_2^{dir} = \frac{N_\gamma^{inc}/N_\gamma^{BG} v_2^{inc} - v_2^{BG}}{N_\gamma^{inc}/N_\gamma^{BG} - 1} \tag{6.2}$$

$$v_2^{dir} = \frac{R_\gamma v_2^{inc} - v_2^{BG}}{R_\gamma - 1} \tag{6.3}$$

The next sections explain how each of these pieces is obtained. The identification of photons was discussed in Sec. 3. The measurement of R_γ has also been discussed in detail, Sec. 4.2. First, the extraction of the inclusive photon v_2 is discussed, followed by a discussion on the contributions to the background v_2. Finally, the calculation of the direct photon v_2 is discussed. The same good run list used in Sec. 4.1 for the invariant yield measurement is used for the v_2 analysis.

6.1 Reaction Plane Resolution

Experimentally, one can estimate the event plane based of the measured particle asymmetries observed in forward detectors. The estimated event plane is different than the true reaction plane. For meaningful results, experiments must correct for the difference due to the resolution of the reaction plane which results from fluctuations in the finite multiplicity of the measurement. The prescription laid out in [54] and [55] is followed. The observed v_2 extracted directly from the data is corrected by dividing by the resolution as given by Eqn. 6.4, with $\sigma_{res,2}$ defined in Eqn. 6.5.

$$v_2 = v_2^{obs} / \sigma_{res,2} \tag{6.4}$$

$$\sigma_{res,2} = \left\langle \cos\left[2\left(\Psi^{true} - \Psi^{meas.} \right) \right] \right\rangle \tag{6.5}$$

The difference between the reaction plane measured in the north and south detector, $\Delta\Psi = \Psi_N - \Psi_S$, is used to estimate the reaction plane resolution as follows. As stated, the azimuthally asymmetric particle production can be described by a Fourier decomposition and Fourier coefficients. The n^{th} order Fourier coefficient, Q_n, can be written as $Q_n = \sum_{j=1}^{M} w_j exp\left(in\phi_j\right)$ in the most general form. If one considers two subevents with nearly identical multiplicities (such as looking at hits only in the North or only in the South detector as done here), then one can denote the Fourier coefficient for the flow from each subevent as Q_n and Q'_n. There will be a correlation between the directions of Q_n and Q'_n in the presence of collective flow. The observable of interest here is the distribution of the relative angle between the Fourier coefficients from each subevent, denoted θ, and defined by $Q_n / \left|Q_n\right| = Q'_n / \left|Q'_n\right| exp(in\theta)$ (i.e. the two measurements are shifted by a phase).

In the current case, each subevent represents an independent measurement of the flow. The distribution of Q_n around the the average value $\langle Q_n \rangle$ is Gaussian by the central limit theorem (the event multiplicity is generally large). This means that the probability distribution of Q_n and Q'_n is the product of two Gaussian distributions. The distribution of θ can then be determined by integrating this probability distribution (and assuming $\langle Q_n \rangle$ and σ_{res} are identical for both subevents) and is shown in Eqn. 6.6.

$$\frac{dN}{d\Delta\Psi} = \frac{e^{-\chi^2}}{2} \left(\frac{2}{\pi}\left(1+\chi^2\right) + z\left[I_0(z) + L_0(z)\right] + \chi^2\left[I_1(z) + L_1(z)\right] \right) \tag{6.6}$$

In Eqn. 6.6, $z = \chi^2 \cos(\Delta\Psi)$ and L_ν and I_ν are the modified Struve and modified Bessel functions of ν^{th} order respectively. $\chi = \langle Q_n \rangle / \sigma_{res}$ is the resolution parameter extracted from fitting $\Delta\Psi$ distributions with the equation. The reaction plane resolution is calculated from χ via Eqn. 6.7. The $\Delta\Psi$ distributions in 10% wide centrality bins are fit with Eqn. 6.6 and shown in Fig. 6.1. The second order reaction plane resolution in the RXNP detector is shown as a function of centrality in Fig. 6.2. The fine binned resolution is rebinned to the binning of the analysis by weighting by the number of inclusive photons in each centrality bin.

$$\sigma_{res,2} = \frac{\sqrt{\pi}}{2} \chi e^{-\chi^2} \left[I_0\left(\frac{\chi^2}{2}\right) + I_1\left(\frac{\chi^2}{2}\right) \right] \tag{6.7}$$

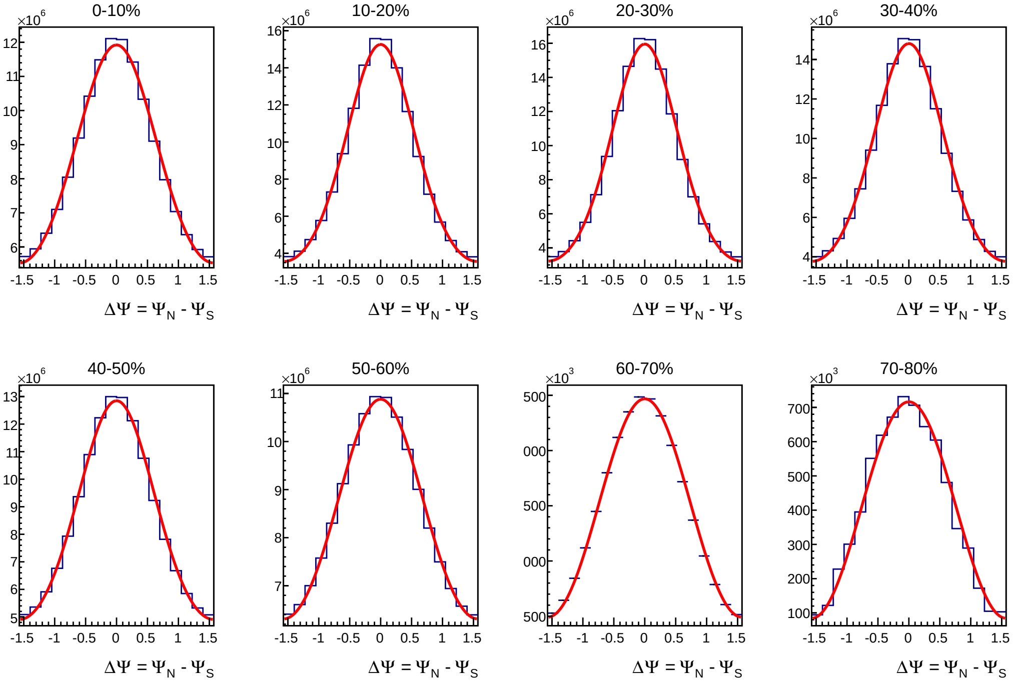

Figure 6.1: $\Delta\Psi$ distributions in centrality bins. The distributions are fit with Eqn. 6.6 to extract the resolution parameter χ.

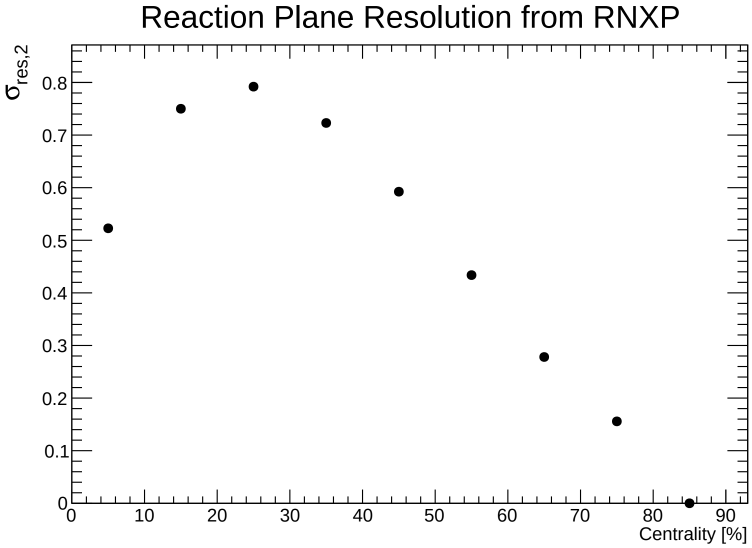

Figure 6.2: The second order reaction plane resolution with the RXNP detector as a function of centrality.

6.2 Inclusive Photon v_2

The inclusive photon v_2 is determined by measuring the modulation of the distribution of the angle of emission, ϕ, of photons with respect to the reaction plane of the collision. From the raw $\phi - \Psi$ distribution, the correlation function of the emitted particles to the reaction plane is produced. This correlation function is then Fourier decomposed. The sine terms are zero due to symmetry, leaving us with the cosine terms. The correlation function is fit with Eqn. 6.8 to extract the photon v_2. Higher order terms are neglected.

$$\frac{dN}{d\phi} = C\left[1 + 2v_2 \cdot \cos\left(2\left(\phi - \Psi\right)\right)\right] \tag{6.8}$$

The measured correlation functions in each p_T bin are shown in Fig. 6.3 for the minimum bias centrality bin. The red line shows the fit with Eqn. 6.8 for each p_T bin.

Two run groups have been considered for this Run 7 analysis, determined by a major change to the PHENIX detector configuration. After run 231000, the west half of the HBD was removed. The runs with and without this HBD half are analyzed separately so that they can be compared to each other and give confidence to the result. When the inclusive photon v_2 from each run group is compared, it is observed that the two results are consistent, see Fig.

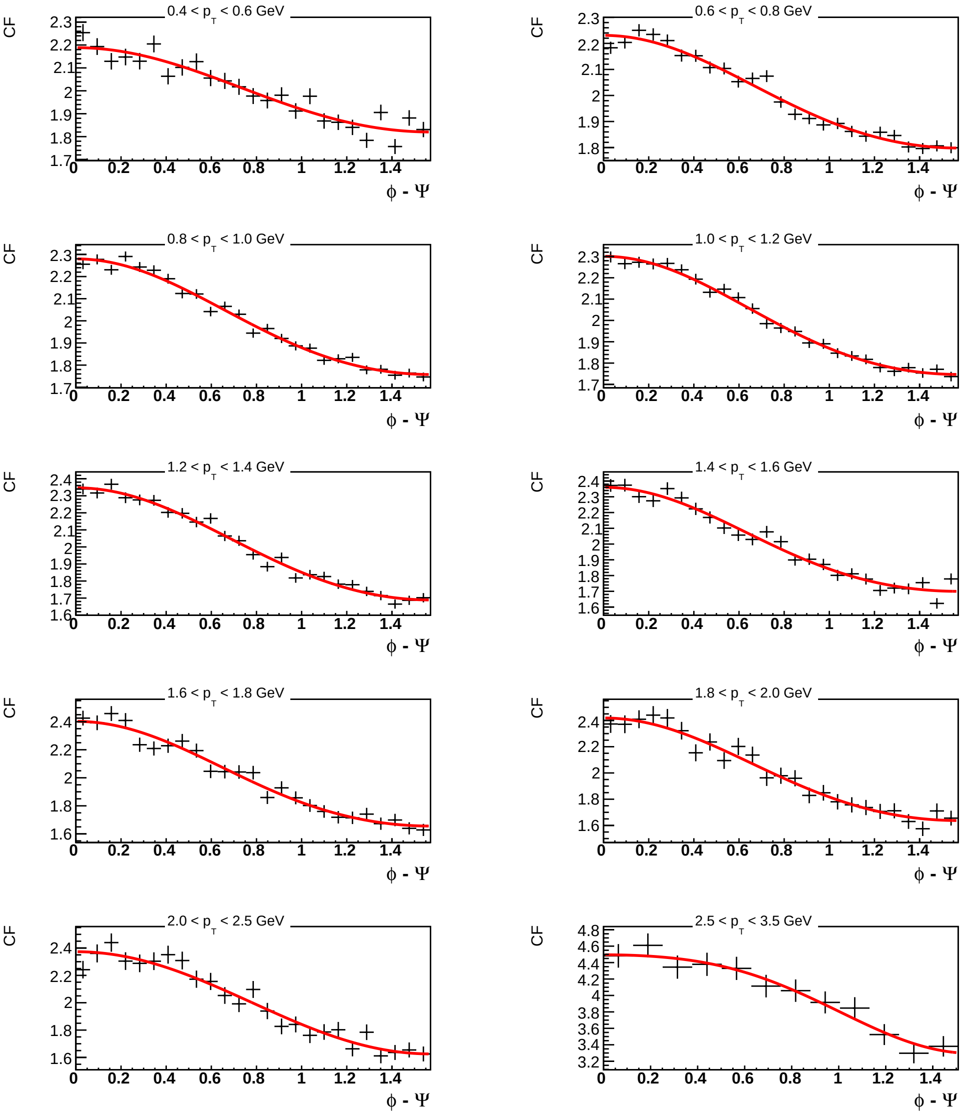

Figure 6.3: The correlation function of the $\phi - \Psi$ distribution for each p_T bin. The red line shows the Fourier decomposition from Eqn. 6.8.

6.4. As a result, the two run groups are then merged into one and analyzed as a single run group.

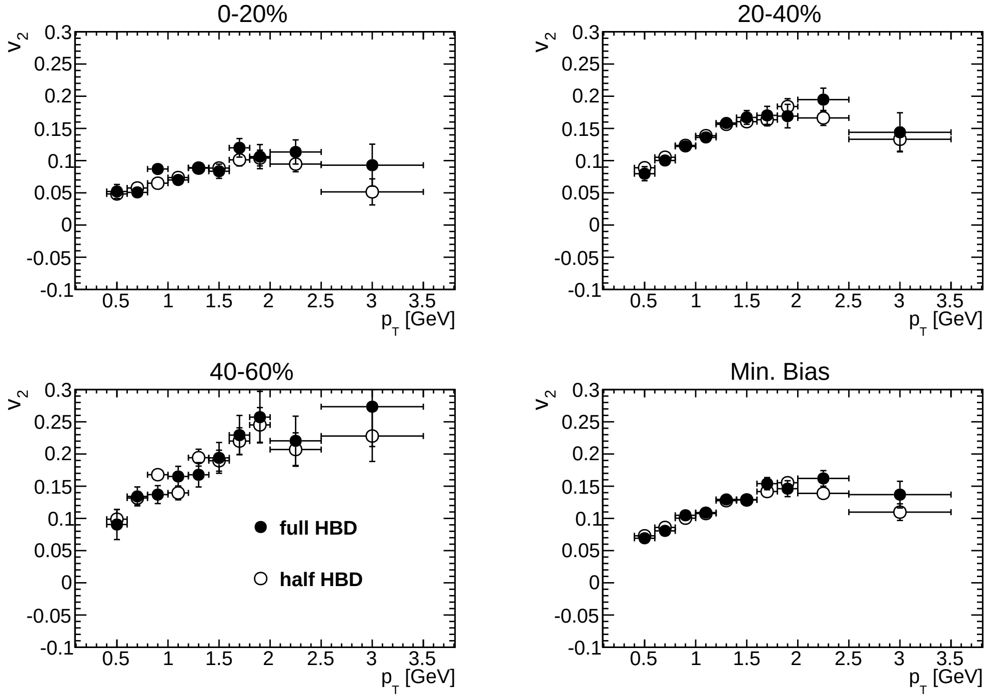

Figure 6.4: A comparison of the inclusive photon v_2 determined from the two considered run groups of the fully installed and half installed HBD configuration.

The extracted inclusive photon v_2 from the plotted correlation functions is shown in Fig. 6.5 for each centrality bin. The v_2 can be measured over the p_T range of 0.4 GeV to 3.5 GeV. The results are consistent with the result found in [30], (see Fig. 6.6). The v_2 shown in Fig. 6.5 already has been corrected for the reaction plane resolution.

6.3 Neutral Pion and Hadron Decay Photon v_2

The direct photon v_2 is measured by statistical subtraction. The v_2 of the background photons, photons from hadron decays, is estimated and extrapolated from measurement. Roughly 80% of photons come from π^0 decays, 10%

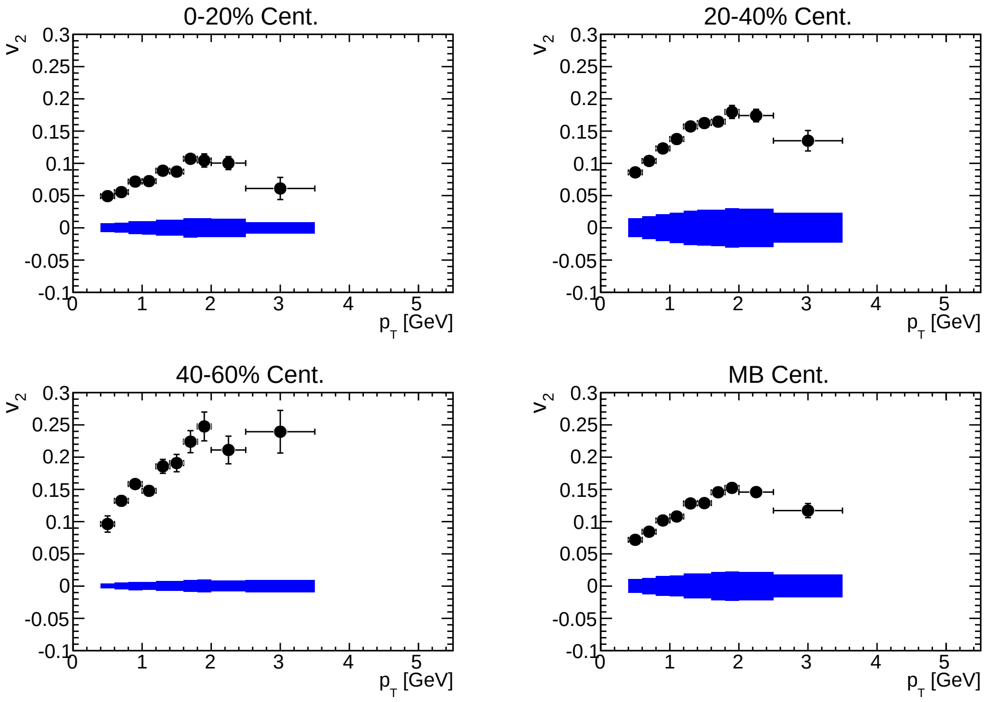

Figure 6.5: The inclusive photon v_2 for the $0-20\%$, $20-40\%$, $40-60\%$, and minimum bias centrality bins. The blue error band at the bottom represents the global scale uncertainty due to the reaction plane resolution.

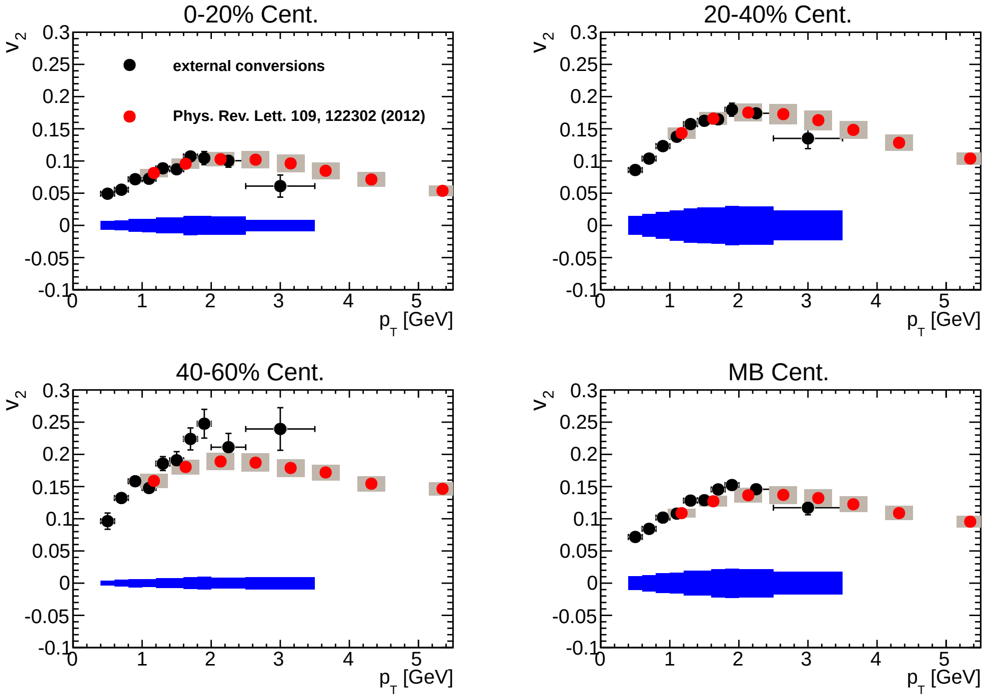

Figure 6.6: A comparison of the current inclusive photon v_2 results with the published results in [30].

from η decays, and the rest from ω and η'. Only the neutral pion v_2 is measured directly, since it represents most of the background. The rest of the hadron decay photon v_2 values are estimated from KE_T scaling ($KE_T = m_T - m$), which holds for hadrons that have been measured [9]. The yield of the hadron decays are the same as used for the decay photon cocktail of Sec. 4.2.3. The background v_2 estimation procedure is the same as in [30].

The neutral pion v_2 is parameterized from data published in [30], combined with the charged pion results [56], by fitting the data with Eqn. 6.9. The pion data with the fit is shown in Fig. 6.7. The data is plotted as v_2/n_q vs KE_T/n_q, where n_q is the number of constituent quarks of the hadron ($n_q = 2$ for the pion). The decay photon v_2 is only estimated in the minimum bias centrality bin.

$$v_2\left(p_T\right) = a_0 + a_1 p_T - \frac{1}{a_2 + \exp\left(a_3 + a_4 p_T\right)} \tag{6.9}$$

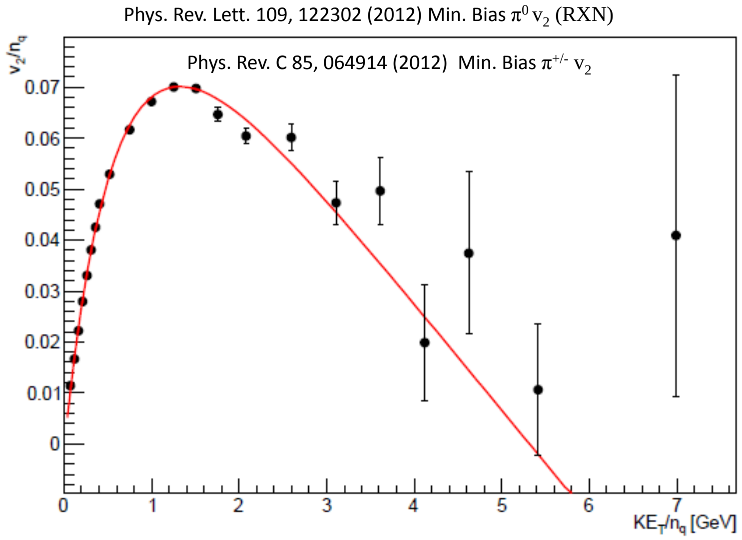

Figure 6.7: Neutral pion [30] and charged pion [56] v_2 normalized per number of constituent quarks vs. KE_T/n_q. The results are fit with Eqn. 6.9 shown by the red line. This parameterization is used to add the v_2 modulation to the cocktail.

As stated, the v_2 of the other hadrons is determined from KE_T scaling. KE_T is defined as $KE_T = m_T - m$, where m is the mass of the hadron. In this way, the v_2 of all hadrons can be determined. The v_2 modulation is built into the hadron decay cocktail introduced in Sec. 4.2.3. The modulation of the ϕ distribution of parent hadrons is imposed and then the hadrons are allowed to decay, with the children inheriting the modulation. Thus the background v_2 of photons due to hadron decays is calculated. The total background v_2, along with the v_2 of each hadron species, is shown in Fig. 6.8. The systematic uncertainty box shown is discussed in Sec. 6.4.3. The v_2 of each species are added to the total by weighting according the the branching ratios and meson to pion ratios discussed in Sec. 4.2.3.

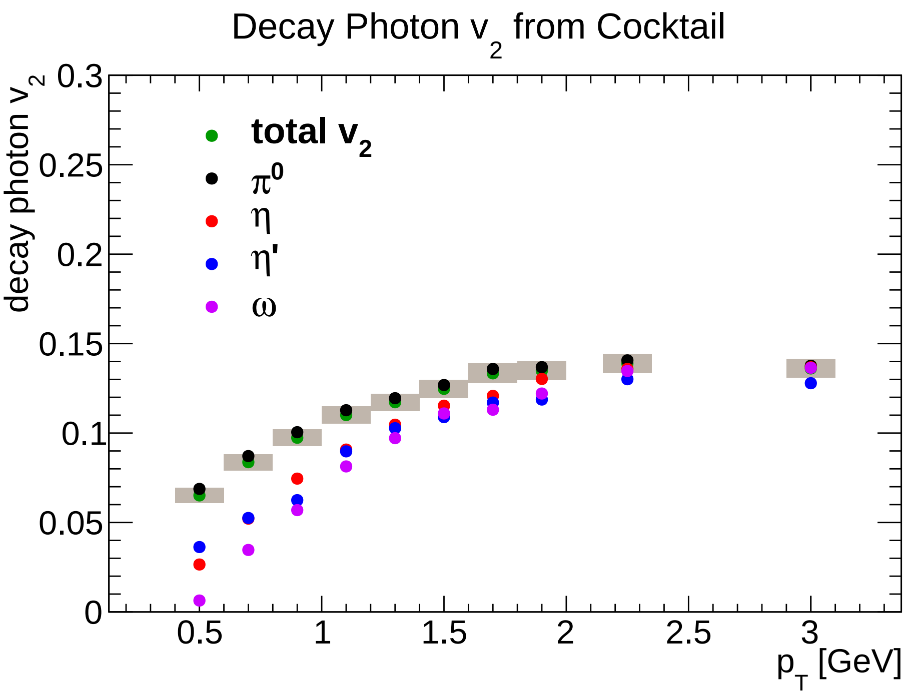

Figure 6.8: The hadron decay photon v_2 calculated from the cocktail. The total, along with each separate contribution in the cocktail is shown.

6.4 Systematic Uncertainty

The systematic uncertainty on the reaction plane resolution, inclusive photon v_2, and decay photon background v_2 is discussed in this section.

The contributing sources of systematic uncertainty are summarized in Table 6.1. The contributing uncertainties are propagated through to the v_2^{direct} via Eqn. 6.10.

Systematic Uncertainty on the Direct Photon v_2			
Contributing via	Source	Sys. Uncert. [%]	Type
$v_2^{\gamma,inc}$	contamination	1	B
	extraction method	1	B
v_2^{BG}	PID for v^{π^0}	3.7	B
	normalization	~2	B
Subtraction	R_γ	~7	B
common	Reaction plane res.	15	C

Table 6.1: A summary of the systematic uncertainties on the direct photon v_2.

$$\sigma_{v_2}^{dir.} = \sqrt{\left(\frac{v_2^{inc} - v_2^{BG}}{(R_\gamma - 1)^2}\sigma_{R_\gamma}\right)^2 + \left(\frac{R_\gamma}{R_\gamma - 1}\sigma_{v_2}^{inc}\right)^2 + \left(\frac{1}{R_\gamma - 1}\sigma_{v_2}^{BG}\right)^2} \qquad (6.10)$$

6.4.1 Systematic on the Reaction Plane Resolution

The systematic uncertainty on the reaction plane resolution is the dominant source of uncertainty in this analysis. It is independent of p_T and so is labeled as a type C global scale uncertainty. The resolution uncertainty is estimated by repeating the analysis with the reaction plane determined using the north and south detectors separately. The resolution of the N(S) only measurement compared to the (N+S) measurement has a worse resolution by a factor of $\sqrt{2}$. This is taken into account and not included as a systematic uncertainty. The comparison of the inclusive photon v_2 with the North and South only measurement to the North plus South measurement is shown in Fig. 6.9. Figs. 6.10 and 6.11 show the ratio of the N/(N+S) and S(N+S) measurements respectively. The constant systematic shift is determined by fitting the ratios with a constant. The systematic uncertainty on the inclusive photon v_2 due to the reaction plane determination for each centrality bin is estimated by averaging the values in Figs. 6.10 and 6.11. This uncertainty is shown by the colored band at the bottom of the plots in Fig. 6.5.

6.4.2 Systematic on the Inclusive Photon v_2

The systematic uncertainty on the inclusive photon v_2 is estimated in a few different ways. One way is that the v_2 is calculated with two different methods, the Fourier decomposition with fit method discussed in Sec. 6.2 and the mean

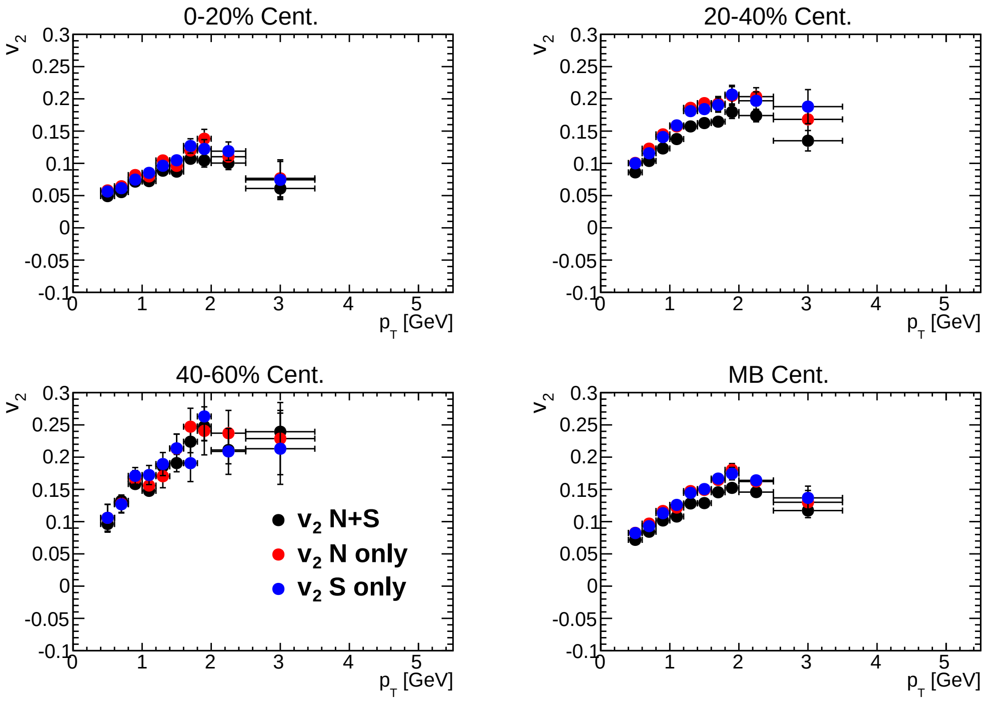

Figure 6.9: The inclusive photon v_2 calculated from the analysis performed with just the north, just the south or the north plus south detector for reaction plane determination.

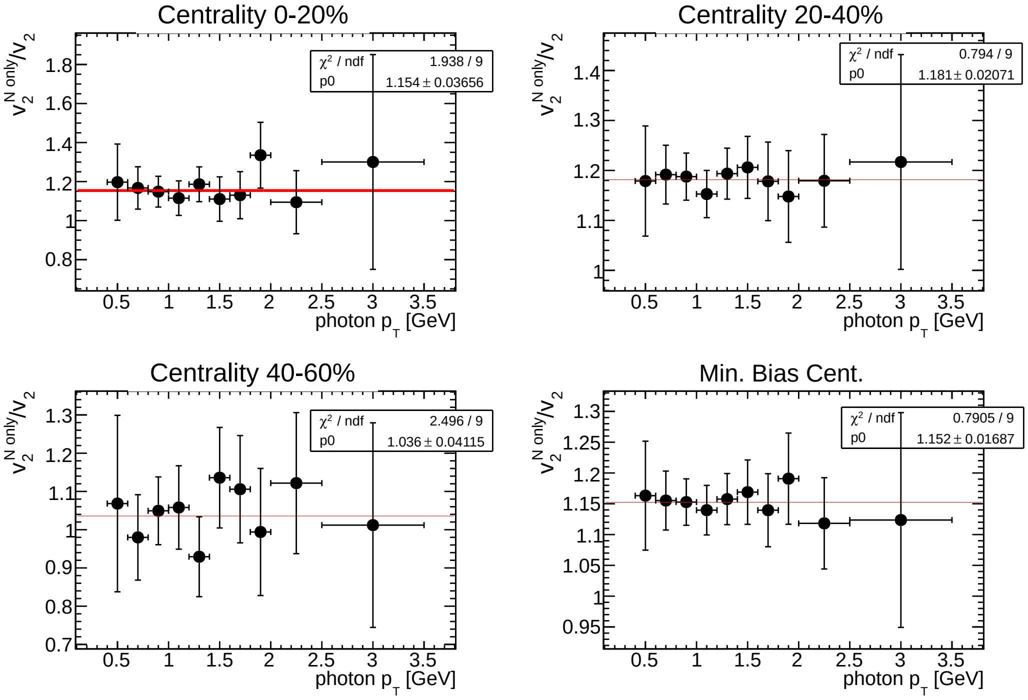

Figure 6.10: The ratio of the north detector only v_2 to the north plus south v_2. A constant shift is observed in each centrality.

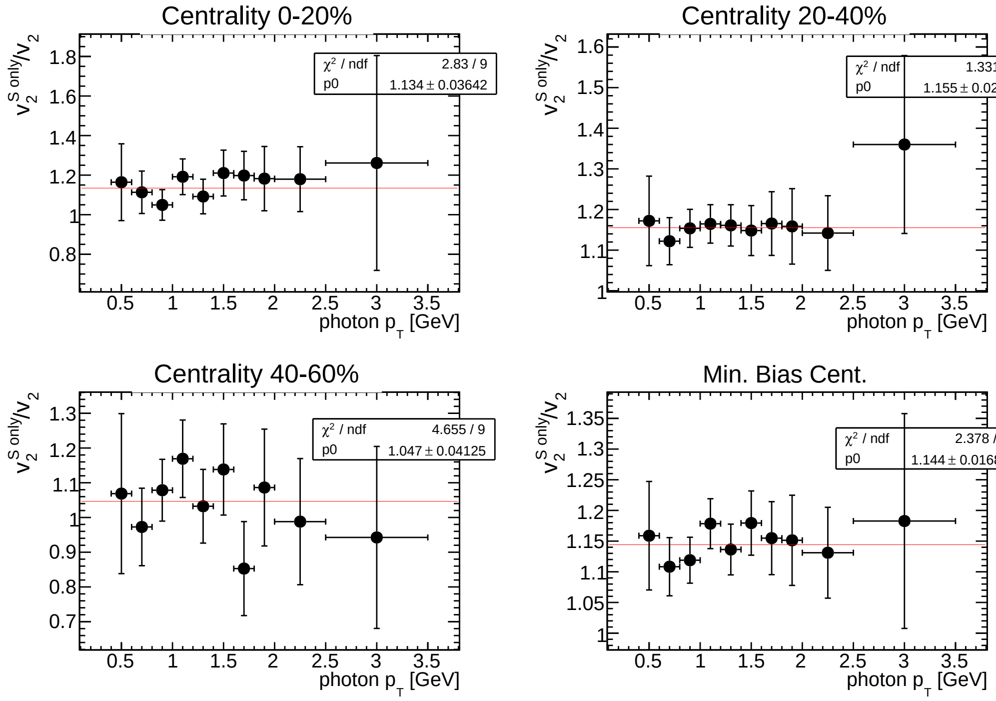

Figure 6.11: The ratio of the south detector only v_2 to the north plus south v_2. A constant shift is observed in each centrality.

projection method. In the mean projection method, the v_2 is calculated by Eqn. 6.11. This equation can be used for each p_T bin. The same reaction plane resolution value from the other method can be applied here.

$$v_2^{obs} = < cos(2(\phi - \Psi)) > \tag{6.11}$$

This method gives consistent results with the fit method described earlier, see Fig. 6.12. The deviation between the two methods is used to estimate a source of systematic uncertainty of ~ 1%.

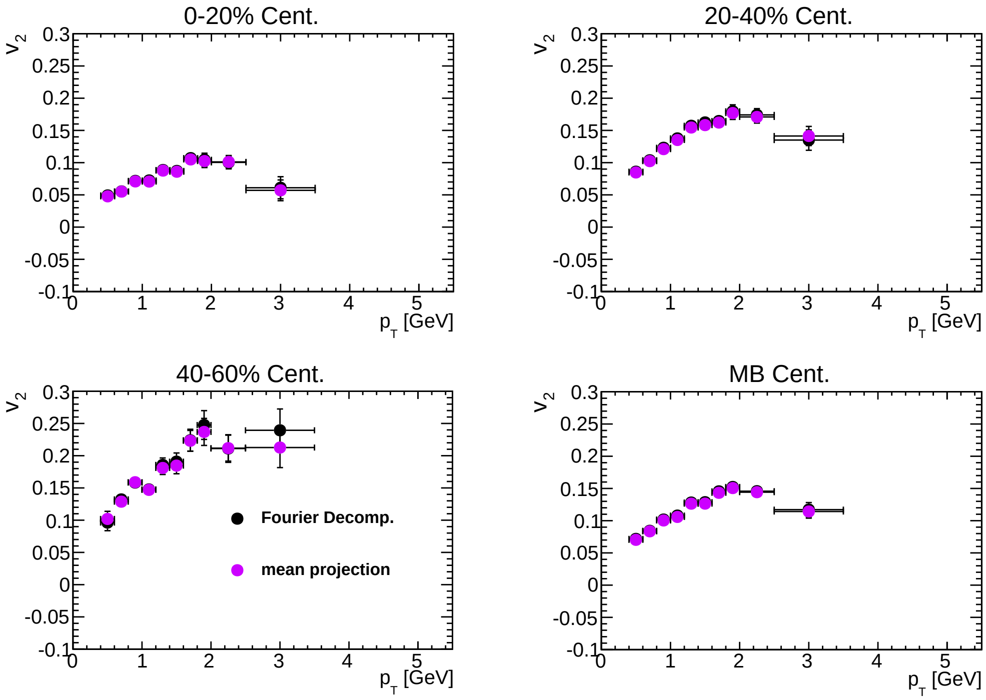

Figure 6.12: A comparison of the inclusive photon v_2 calculated by fitting with the Fourier decomposition or via the mean projection method.

An additional systematic uncertainty on the inclusive photon v_2 arises from contamination of the photon sample. As discussed in Sec. 3, the sample purity is estimated as 99%. Therefore an additional 1% type B uncertainty is added to cover the uncertainty from the contamination in the photon sample. This is added in quadrature to the method uncertainty and the result is plotted as the gray boxes around the points in Fig. 6.5.

6.4.3 Systematic on the Decay Photon v_2

The systematic uncertainty on the decay photon v_2 is estimated in part by calculating the background v_2 assuming only pion contributions and comparing the result to the full hadron cocktail. This tests the sensitivity to the total decay photon v_2 to the various subdominant contributions. The estimated systematic as a function of p_T is shown in Fig. 6.13 and varies from 5% at low p_T to 1% at high p_T.

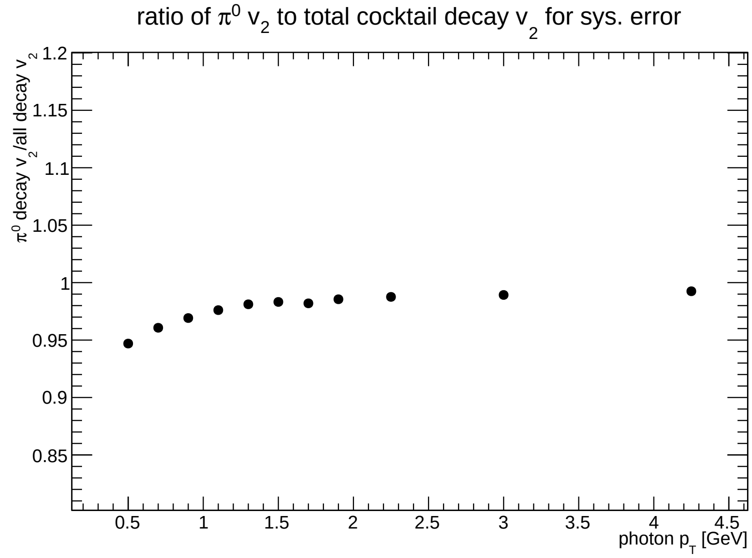

Figure 6.13: The ratio of the decay v_2 calculated by assuming only pion contributions to the cocktail and assuming the full hadron cocktail. The ratio is taken as the systematic uncertainty due to the normalization of the hadron contributions.

The systematic on the pion v_2 measurement [30] used for the cocktail input is additionally folded into the systematic uncertainty on the cocktail. This includes a 3.7% uncertainty due to the photon identification.

Chapter 7

Results: Direct Photon v_2

The direct photon v_2 is calculated from the inclusive photon v_2 (Sec. 6.2), the hadron decay photon v_2 (Sec. 6.3), and the relative fraction between the two, R_γ (Sec. 5.1) as shown in Eqn. 6.3. The measured direct photon v_2 is shown in Fig. 7.1 in minimum bias collisions. In Fig. 7.2, the result is compared to the published PHENIX result in [30]. The results are quite consistent. The background v_2 is only modeled in minimum bias collisions, and so only that centrality bin is shown. This is an important confirmation of the surprising result obtained in [30]. Fig. 7.3 shows the direct comparison of the direct photon v_2 with the measured inclusive photon v_2 and the published π^0 v_2 [30] from which the background v_2 is calculated. Table A.16 shows the points from Fig. 7.1.

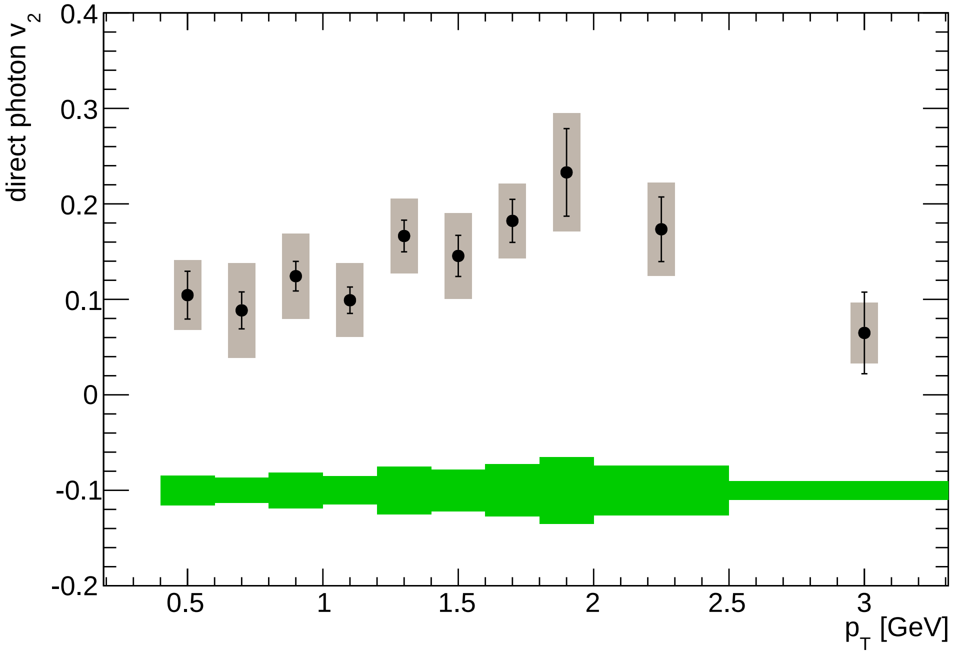

Figure 7.1: The direct photon v_2 measured in minimum bias collisions.

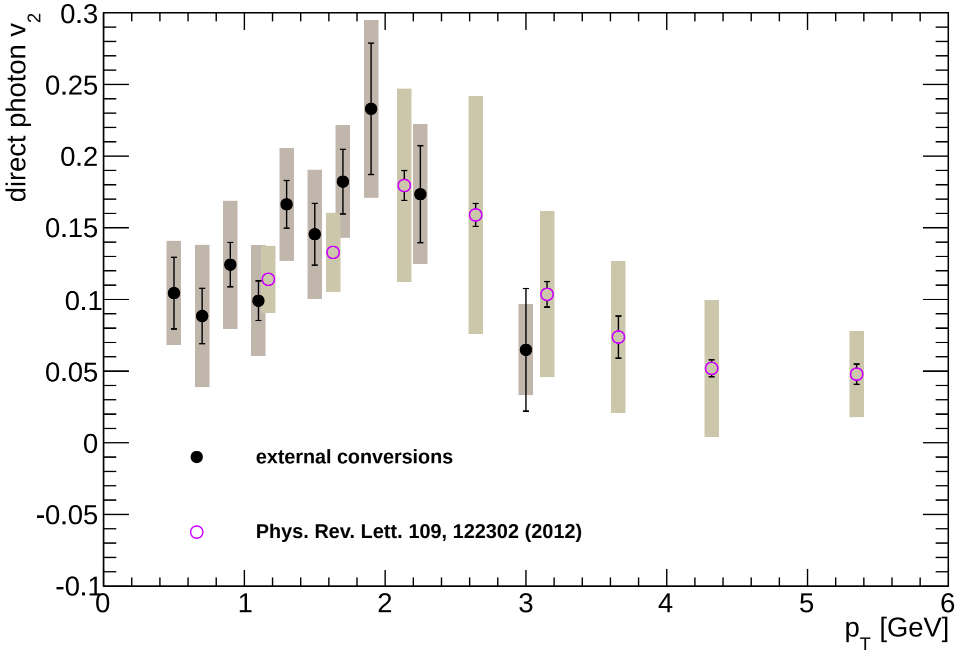

Figure 7.2: The direct photon v_2 measured in minimum bias collisions compared to the result from [30].

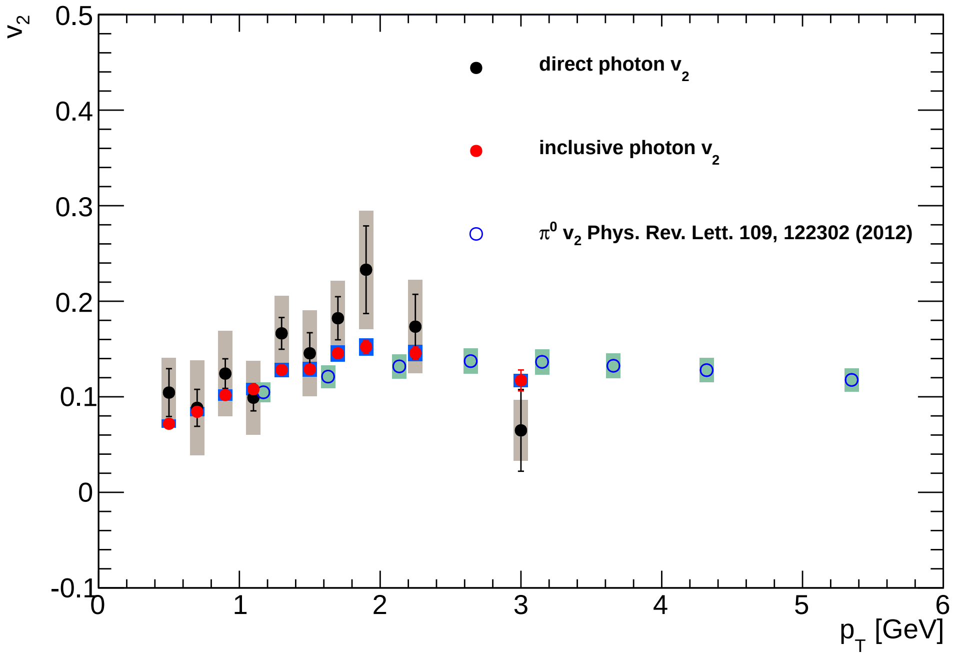

Figure 7.3: A comparison of the v_2^{direct}, v_2^{incl} and $v_2^{\pi^0 decay}$.

Chapter 8

Discussion

8.1 The Direct Photon Yield

The results and an analysis on the direct photon invariant yield shown in Figs. 5.6 and 5.7 will now be discussed. The contribution from primordial production of direct photons in hard 2→2 scattering is not relevant for this analysis. Therefore the primordial contribution is estimated and subtracted from the direct photon yield. The procedure in [27] is followed, where p+p data is used to constrain the shape. This is done because no medium effects are observed in p+p and only hard scattering processes are expected. The hard scattering processes should roughly scale as the number of binary collisions or with the nuclear thickness function, T_{AA}, in Au+Au collisions.

Simultaneous fits to the PHENIX direct photon spectra from [27] [57] [58] in p+p collisions at $\sqrt{s_{NN}} = 200 GeV$ are performed. This is shown in Fig. 8.1. The measured data points for each data set is shown by the colored points as described in the legend. In the fitting, only the statistical errors on [27] are used, while for [57] and [58] the statistical and systematic errors are added in quadrature in an effort to reduce the overwhelming precision of the latter two results dominating the fit. Various fits are performed to get an estimate of the systematic uncertainty in the extrapolation of the direct photon yield where there is no data (below 1GeV). The various fits are shown in Fig. 8.1 by the colored lines. The legend describes the color coding as well as displays the χ^2 per degree of freedom for the corresponding fit. All fits (with two exceptions) have a small χ^2 less than one, indicating that the fit is over constrained due to the large error bars on the data.

Three different parameterizations are used for the functional shape. First, the data is fitted with the modified power law function that is used in [27], $E\frac{d^3\sigma}{dp^3} = a\left(1 + p_T^2/b\right)^{-n}$ (black lines). Another fit with a pure power law func-

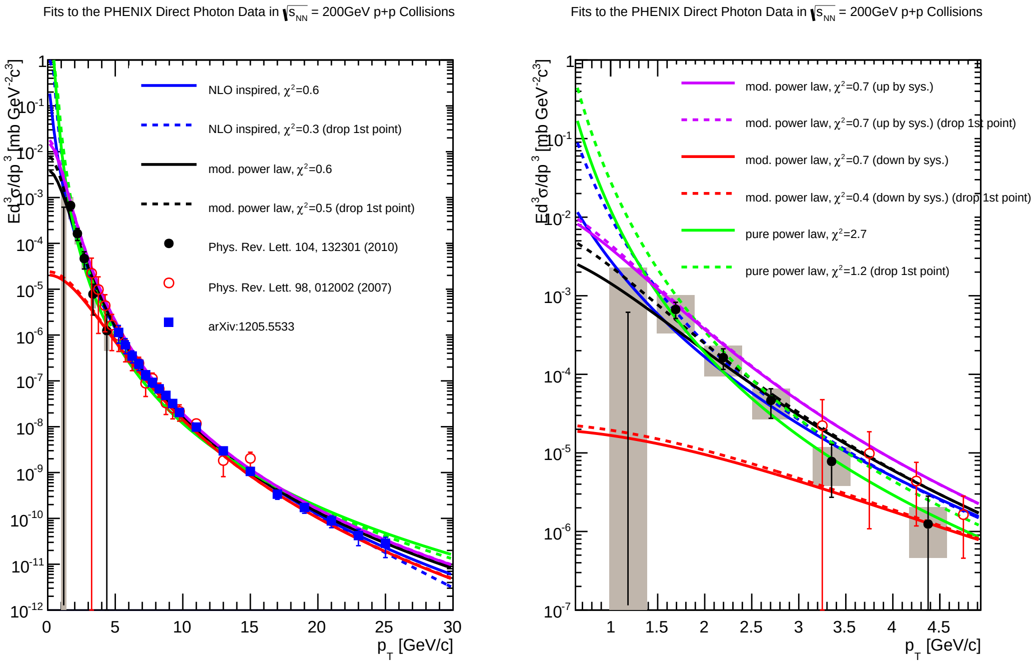

Figure 8.1: Fits to the p+p data to constrain the shape of the underlying primordial direct photon contribution. The various data sets are shown by the points and the various fits are shown by the lines, see the legend. The left panel shows the fits over the entire range of the measurements, the right panel shows a zoom in to low p_T.

tion is performed as done in [27], $E\frac{d^3\sigma}{dp^3} = a/p_T^n$, (green lines). Lastly, the data is fit with a power law like function inspired by NLO QCD used in [8], $E\frac{d^3\sigma}{dp^3} = a \cdot p_T^{-(b+c \cdot ln x_T)} \cdot (1 - x_T^2)^n$, where $x_T = 2p_T/\sqrt{s}$ (blue lines). The fit range is varied for each function to cover the full data range and also with dropping the very first p_T data point at 1GeV, where the measured yield is actually negative (indicated by the solid and dashed lines respectively). Additionally, the modified power law fits are done with all the data points shifted up and down by each point's respective systematic uncertainty (purple and red lines). The left side of Fig. 8.1 shows the results of all these fits over the full range covered by the data sets ($1 < p_T < 25GeV$), while the right side shows a zoom in for the p_T range relevant for this analysis ($p_T < 5GeV$).

The fits to the p+p spectra are then scaled by the nuclear thickness function, T_{AA}, for the corresponding centrality bin, which accounts for the increased probability of hard scattering in Au+Au compared to p+p due to more participant particles. These values are calculated from a Glauber Monte Carlo simulation [59] and are listed in Table 8.1 with the corresponding systematic uncertainties. The values are taken from [60].

T_{AA}, N_{part}, and N_{qp} for Each Centrality Bin						
Centrality	T_{AA}	sys. error	N_{part}	sys. error	N_{qp}	sys. error
0-20%	18.55	1.27	279.9	4.0	735.2	14.6
20-40%	7.06	0.58	140.4	4.9	333.2	10.7
40-60%	2.15	0.25	59.9	3.5	126.5	6.1
60-90%	0.35	0.1	14.5	2.5	30.2	4.7
0-90%	6.14	0.45	109.1	4.1	290.0	8.8

Table 8.1: T_{AA}, N_{part}, and N_{qp} values calculated from a Glauber Monte Carlo simulation [60] [61].

Fig. 8.2 shows the Au+Au direct photon spectra with the T_{AA} scaled p+p fits overlayed on the plot. The direct photons measured in Au+Au collisions from [25] are also shown by the red squares. Fig. 8.3 shows a zoom in at the relevant p_T range. The scaled p+p fits are then subtracted from the data and the result in shown in Fig. 8.4.

The RMS of the spread of the difference of the measured excess yields for each parameterization compared to the baseline measurement for each point in Fig. 8.4 is calculated and used as the additional systematic uncertainty due to the extrapolation of the p+p scaled data. This is shown in Fig. 8.5.

Fig. 8.6 shows the scaled p+p subtracted direct photon yield with its systematic uncertainties. The fit chosen to represent the baseline measurement is the modified power law fit to the data with the first p_T point dropped. This

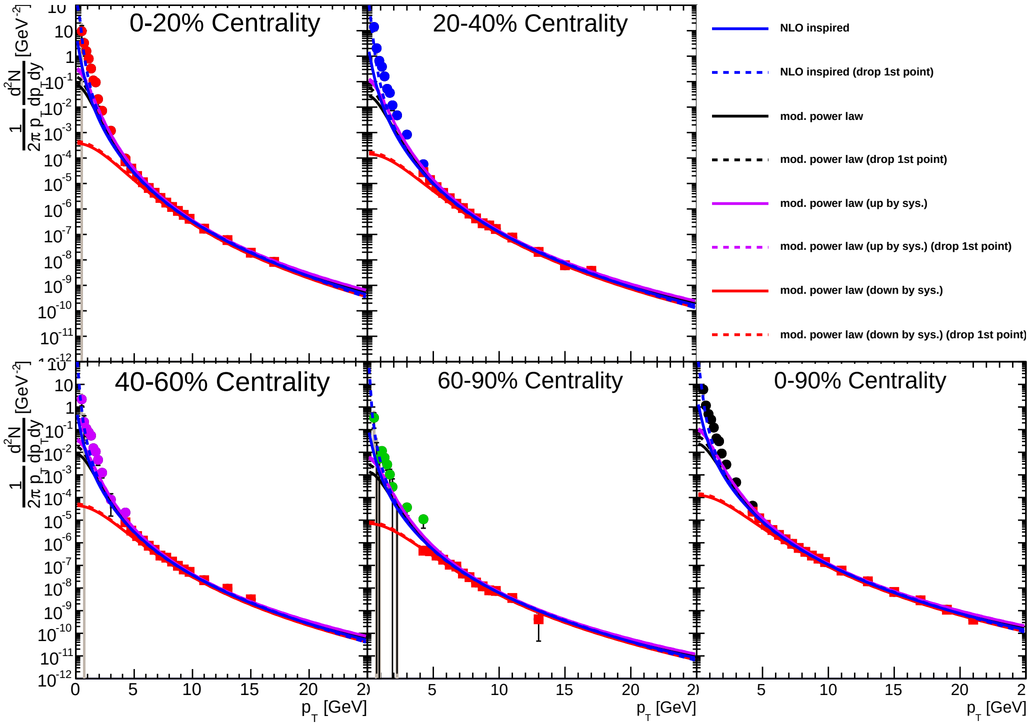

Figure 8.2: The direct photon invariant yield in Au+Au collisions. Results from [25] are also shown by the red squares. The lines represents the p+p fits scaled by T_{AA} for each centrality bin. The results are plotted in the range of $0 < p_T < 20 GeV$.

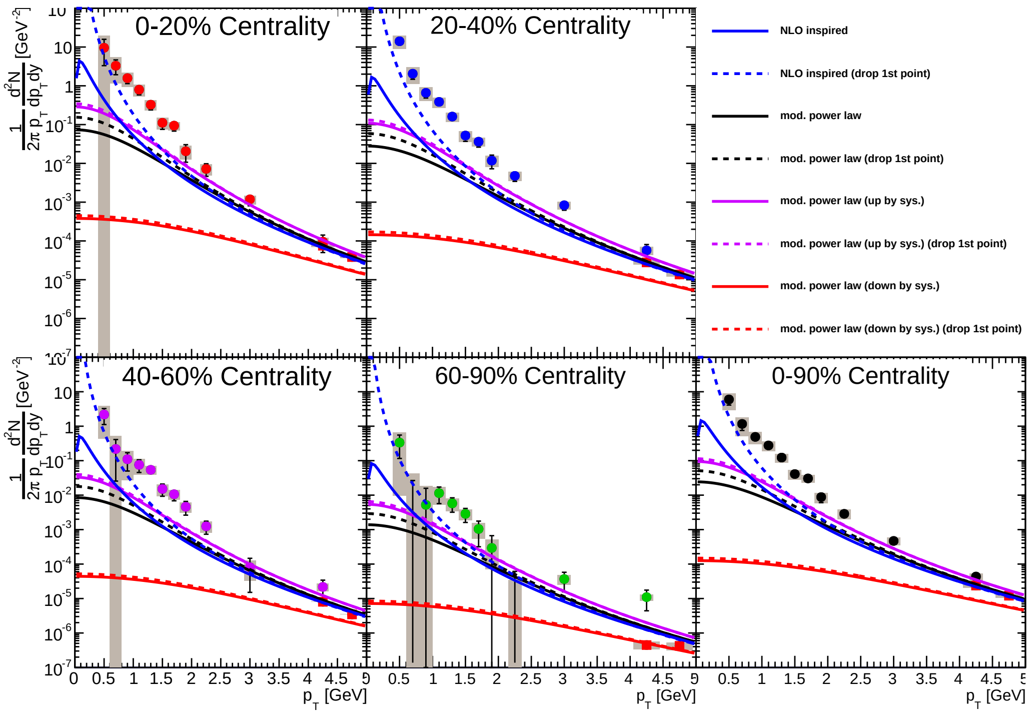

Figure 8.3: The direct photon invariant yield measured in Au+Au collisions. Results from [25] are also shown by the red squares. The lines represents the fits to the p+p data scaled by T_{AA} for each centrality. The results are plotted in the range of $0 < p_T < 5GeV$.

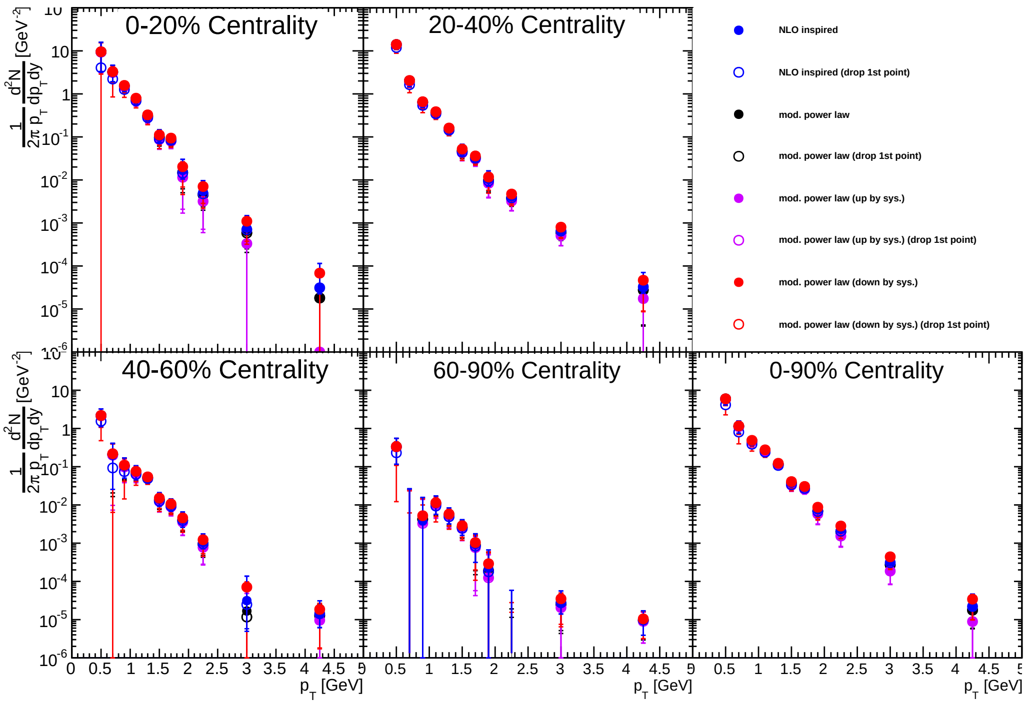

Figure 8.4: The subtracted excess for each p+p parameterization represented by each color.

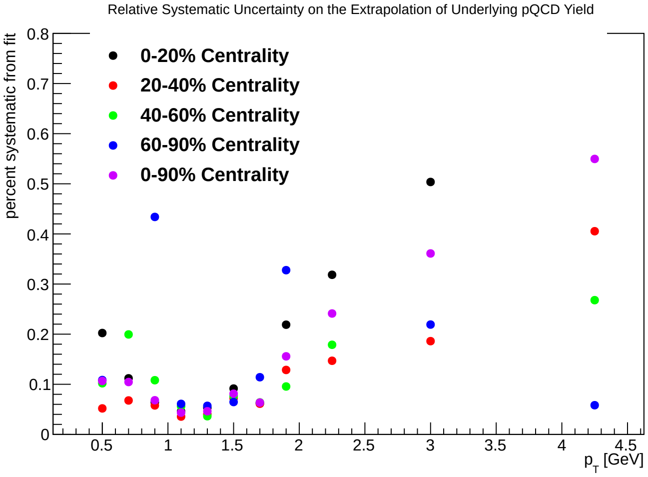

Figure 8.5: The RMS of the excess calculated by subtracting each p+p parameterization. This is used as the systematic uncertainty on the extrapolation of the fits from the p+p data.

is chosen mainly because it sits in the middle of all the parameterizations. The statistical error on the fit is propagated through to the subtracted yield. The systematic uncertainty on the unsubtracted direct photon result is propagated through to the subtracted yield and added in quadrature with the uncertainty from the extrapolation to low p_T from the spread of the various fits as shown in Fig. 8.5. Now an analysis on the pQCD subtracted direct photon yield, which is presumably dominated by thermal radiation, is presented, focusing on two aspects to be discussed below. First the observation from [27] that the spectrum is exponential is evaluated by fitting the excess with a pure exponential, as well as calculating local slopes on every set of three consecutive points. This is followed by looking at the N_{part} dependence of the integrated yield.

The excess yield of Fig. 8.6 is fit with a pure exponential function. This is shown in Fig. 8.7, along with the χ^2/NDF of each fit. The data cannot always be described well by a pure exponential (it depends on the centrality bin, and hence the size of the errors). It is true that the spectral shape is exponential over most of the p_T range of this measurement. The deviation comes in at the lowest and highest p_T . Even though it is expected that photons in this p_T range originate from a thermal source, it may not imply that the distribution is a pure exponential, given that the source is not static, but rapidly expanding. This expansion leads to blue shifts, distorting the exponential shape. The extracted inverse slope parameters from the fits are

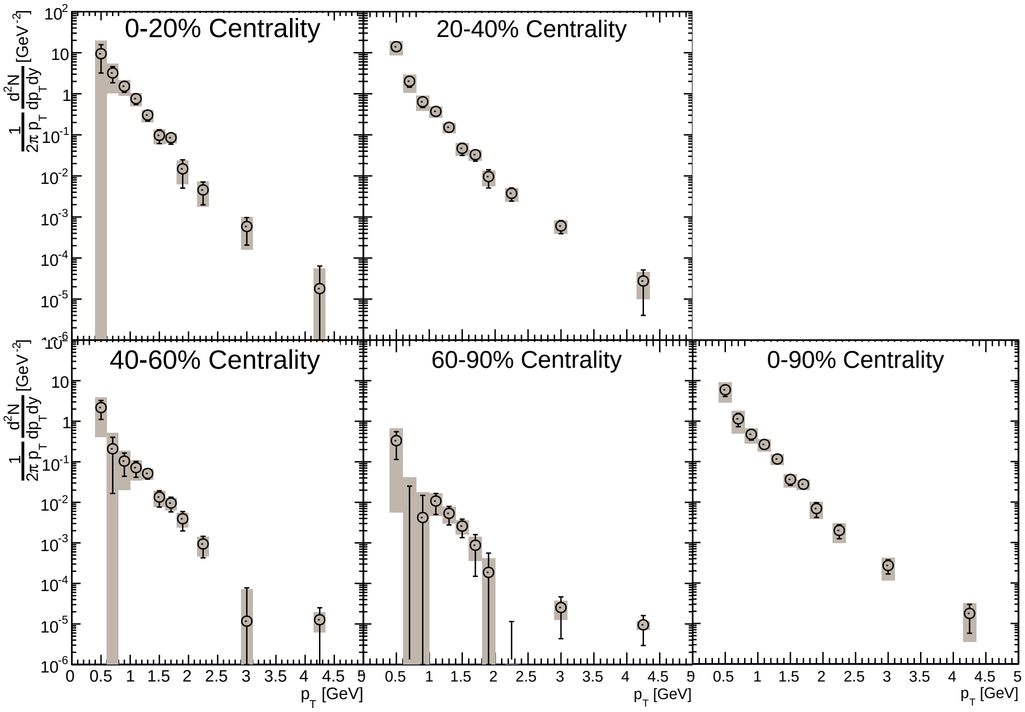

Figure 8.6: The excess direct photon yield result with its full systematic uncertainty.

shown in Table 8.2 for each centrality bin along with statistical error (extracted from the fit) and systematic uncertainty (extracted by moving all points up and down by their respective systematic uncertainties and refitting). Note that the extracted inverse slopes are all the same within uncertainties. The values are in agreement with previously published results [27]. Also note that the procedure of moving all points fully up (or down) by its systematic uncertainty and refitting may result in a slight underestimate of the systematic uncertainty on the slope.

In Ref. [27], it is stated that the inverse slope can be related to the temperature of the medium and that, by comparing to the model calculations at the time, indicated that the initial temperature of the medium is quite high and well above the expected critical temperature to quark deconfinement. Very recent work [29] has pointed out that this may not necessarily be true, as the significant radial flow can blue shift photons, making them look as if they come from a hotter medium. Within this paper, the authors find that almost all ($\sim 70\%$) of thermal photons come from late stage hadronic matter. That which does come from early time is dominated by emission from the cooler periphery of the medium. This is an extreme closing of the QGP window.

Extracted Inverse Slope Parameter from Exponential Fits			
Centrality [%]	Inverse Slope [MeV]	stat. error [MeV]	sys. error [MeV]
0-20	237	16	4
20-40	239	17	6
40-60	267	21	10
60-90	254	40	28

Table 8.2: Inverse slope parameter extracted from exponential fits to the direct photon excess in each centrality bin.

The shape is investigated further by looking at local slopes. Three separate fits of three consecutive points are performed. Non-overlapping fit ranges are chosen so that the results are statistically independent. The ranges $0.4 - 1.0 GeV$, $1.0 - 1.6 GeV$, $1.8 - 3.5 GeV$ are used for this local slope analysis. The fits are shown along the top row of Fig. 8.8. The bottom row shows the inverse slope parameter from each of the fit regions, which are fit with a first order polynomial and show a significant slope. This also supports the statement that the excess is not purely exponential in shape (and roughly the same shape for all centrality).

The next item under investigation is the centrality dependence of the yield. The centrality is chosen to be expressed either by the average number of (nucleon) participants, N_{part}, or the average number of quark participants,

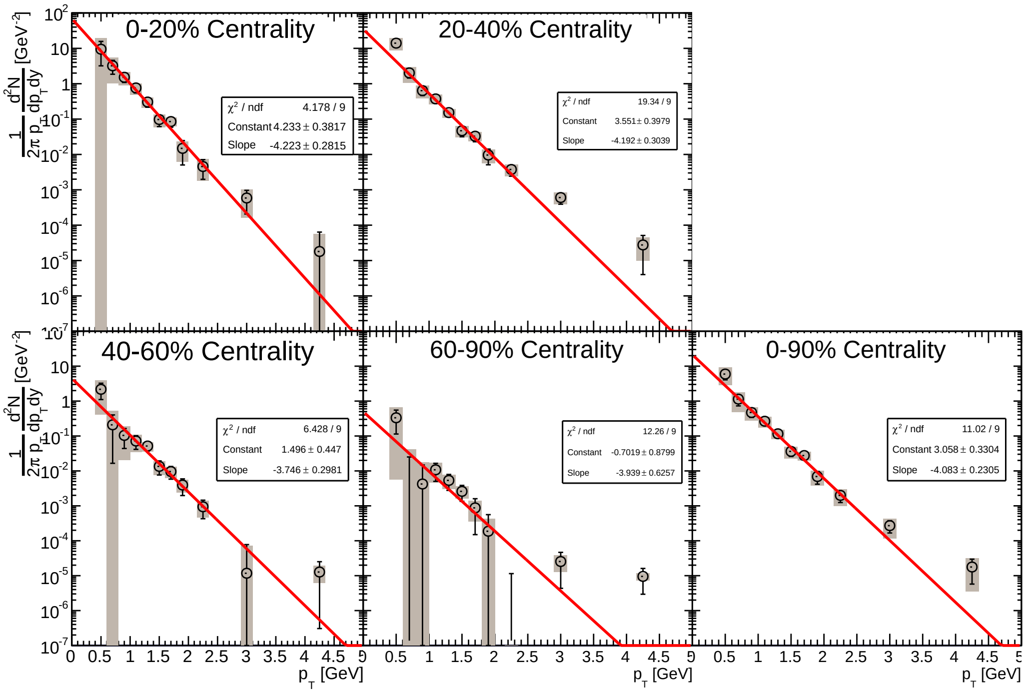

Figure 8.7: The direct photon excess fit with an exponential function for each centrality bin.

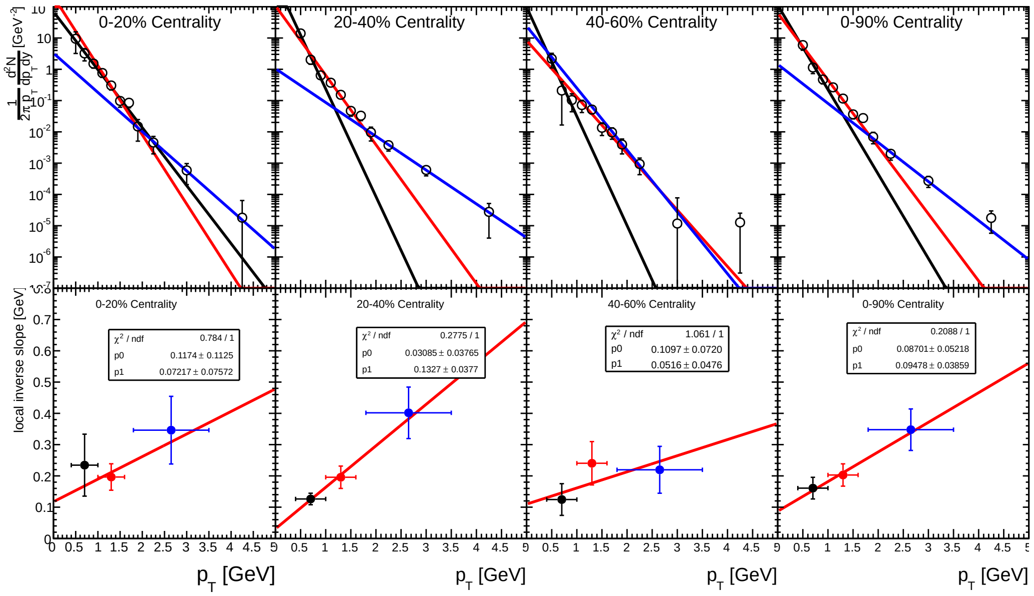

Figure 8.8: A local slope analysis on the direct photon excess. The 3-point exponential fits are shown along the top row for each centrality bin. The bottom row shows the inverse slope parameter for each fit. A first order polynomial is fit to the inverse slope parameters, indicating a change of shape.

N_{qp}. Both of these values are calculated from a Glauber Monte Carlo simulation [60] [61] and are listed in Table 8.1.

The excess spectra shown in Fig. 8.6 is cast in a different form to illustrate the N_{part} and N_{qp} dependence of the yield. Each data point of the excess invariant yield is plotted as a function of N_{part} (Fig. 8.9) and N_{qp} (Fig. 8.11). An approximate scaling is observed, showing the invariant yield of the excess scaling as a power law. No integration is performed, each single point is simply plotted as a function of $N_{part}(N_{qp})$. In this way, each p_T bin represents a statistically independent measurement of the power law. Following this, the power extracted from a fit for each p_T is plotted. Figs. 8.10 and 8.12 show this plot for the N_{part} and N_{qp} scaling respectively. The power law is extracted by fitting a constant. An N_{part} scaling with a power of $1.40 \pm 0.08 \pm 0.03$ and N_{qp} scaling with a power of $1.28 \pm 0.07 \pm 0.02$ is observed. The systematic uncertainty of 0.03(0.02) is estimated by moving all yield points up and down by the point's respective systematic uncertainties and redoing the fits.

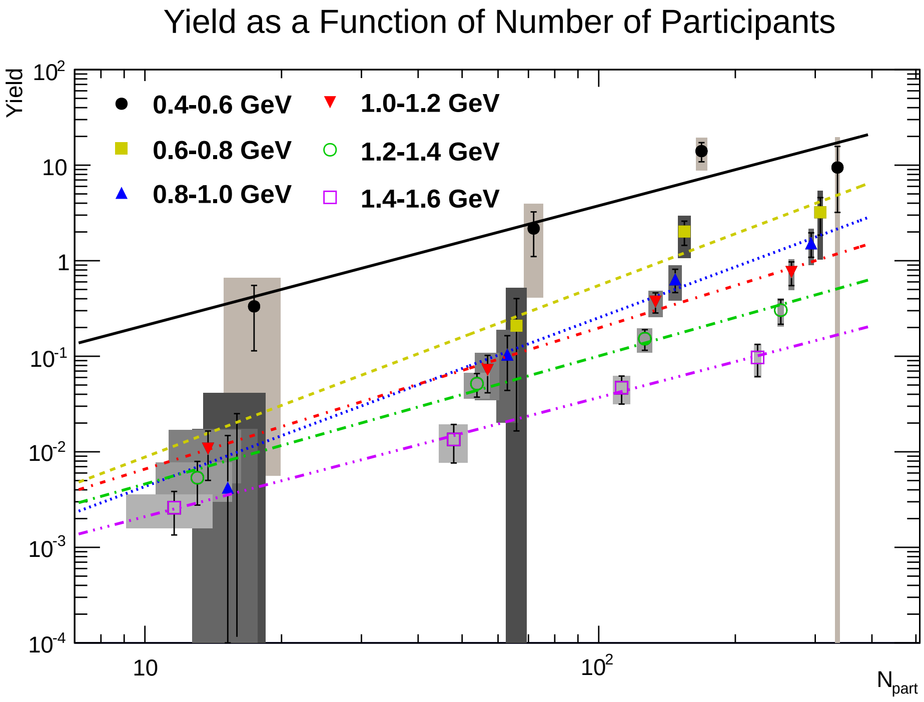

Figure 8.9: The invariant yield for each p_T bin plotted as a function of the number of participants, N_{part}.

This interesting result can be used to constrain model calculations. Currently there is very little theoretical work on the centrality dependence of low

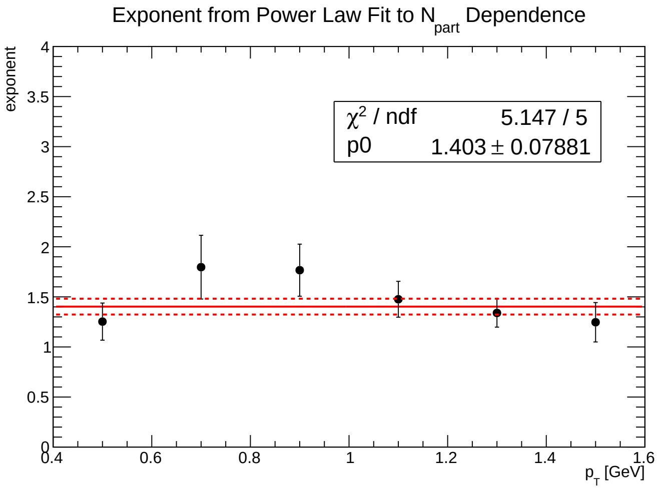

Figure 8.10: The exponent from power law fits to each p_T bin shown in Fig. 8.9.

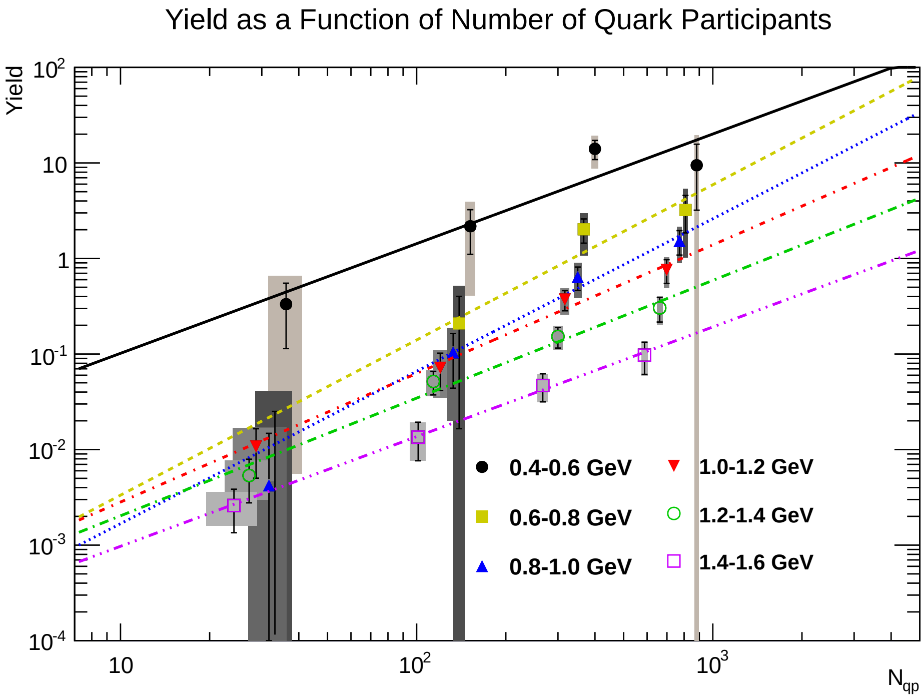

Figure 8.11: The invariant yield for each p_T bin plotted as a function of the number of quark participants, N_{qp}.

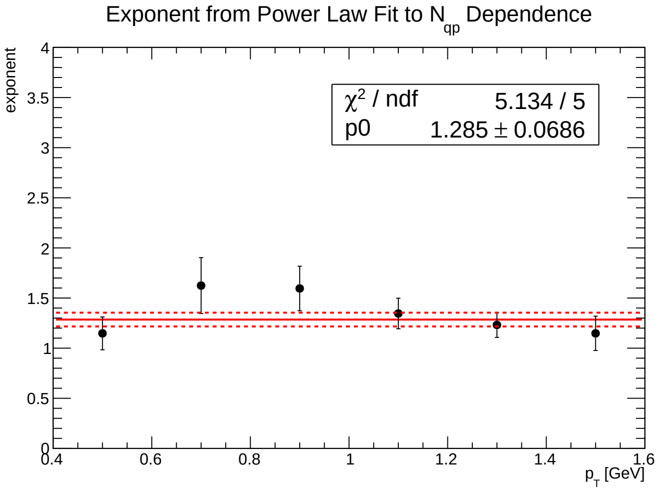

Figure 8.12: The exponent from power law fits to each p_T bin shown in Fig. 8.11.

momentum direct photons.

8.2 The Direct Photon v_2

As already discussed, theory calculations underestimate the direct photon v_2 published by PHENIX [30]. This situation remains with the current measurement within this thesis, as the two results are consistent, see Fig. 8.13. In this way, the external photon conversion analysis serves as an important cross-check to the published result and illustrates that the neutral hadron contamination is properly corrected for (which can be a concern at low p_T).

The direct photon v_2 is compared to both the inclusive photon v_2 measured in this thesis, as well as the π^0 v_2 measured in [30] in Fig. 7.3. As can be seen, the direct photon v_2 is of the same magnitude as the π^0 v_2. This is not a surprise, given the compatibility between the direct photon and inclusive photon v_2 and the fact that we do measure a significant ($\sim 20\%$) direct photon signal above hadronic background. In addition to this measurement confirming the published result, it also extends the measurement down to 400 MeV.

8.3 The Thermal Photon Puzzle

The results shown here display the first measurement of the centrality dependence of the invariant yield of the direct photon excess in heavy ion collisions.

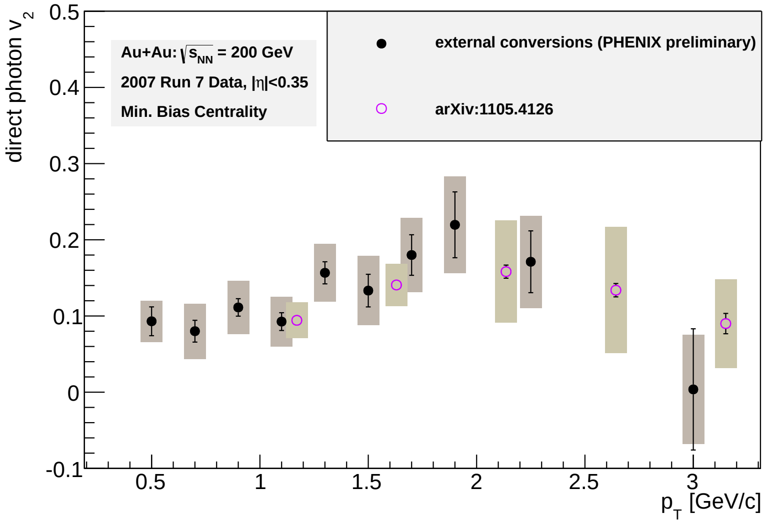

Figure 8.13: The comparison of the measured direct photon v_2 in minimum bias collisions compared to the published results [30].

The results promise to offer powerful constraints on theory calculations. As discussed in Sec. 1.4, there is currently an inconsistency with current theory and experimental observations in regard to the large direct photon excess yield and large v_2. Reconciling these two observations in a coherent model is of utmost importance to fully understand the physics of heavy ion collisions. There has been much theoretical activity as of late proposing solutions to the thermal photon puzzle. Two emerging solutions have recently come to light. They are discussed in the following subsections.

8.3.1 The Closing of the QGP Radiation Window

One solution to the thermal photon puzzle is that the radiation observed is dominated by thermal radiation from the relatively late time hadronic phase. The calculations performed in [24] predict this is the solution. In this calculation, the authors expand on their previous work, incorporating various advancements that result in increasing the yield of hadronic phase emission compared to QGP emission. The calculation does not do a full hydrodynamical description of the fireball evolution, but instead use an elliptic blastwave source model that is constrained by data measurements of bulk hadrons. A further refinement included in this calculation is the addition of effective chemical potentials for pions, kaons, and the other mesons (and baryons), which accounts for off-equilibrium effects in the hadronic phase in between chemical and kinetic freezeout (in contrast to most hydrodynamical descriptions which assume chemical equilibrium throughout the hadronic phase, such as in [23]). They state that this can augment the yield of thermal photons from the hadron gas through the enhancement of processes such as $\pi\rho \rightarrow \pi\gamma$. Another difference from hydrodynamical descriptions is that the elliptic flow builds up faster and the hadronic phase lasts longer, due to both a smaller kinetic freezeout temperature and a larger chemical freezeout temperature. And so the authors predict that the QGP radiation window is actually closed and all we observe is the shine from the hadron gas. The direct photon spectra from the calculation are confronted with data in Fig. 8.14. Note that this is for $|y| < 0.5$ around mid-rapidity.

The figure shows the breakdown of each source of photons compared to the total calculated yield, as well as the measurement presented in this thesis. This is shown for two centrality bins, $0-20\%$ and $20-40\%$. The hadron gas emission (dotted blue line) dominates the yield to about 3GeV, where primordial production (dotted-dashed green line) then begins to dominate. This is seen in both centrality bins. The emission from the QGP phase (dashed red line) is always the smallest contributor to the total yield. The calculation does a decent job describing the data in the $0-20\%$ centrality bin (although still is a little low). The calculation for the $20-40\%$ centrality bin significantly underpredicts the yield from the measurement (roughly a factor of 2). This indicates that the calculation does not quite capture the centrality dependence of the yield at this qualitative level.

The authors of [24] additionally calculate the direct photon v_2 within their framework. Due to the increased yield of late time emission, they calculate a v_2 that is about a factor of three larger than the calculation from [23], which closes the gap between measurement and theory significantly. Only the minimum bias direct photon v_2 is measured within this thesis, and so we make the comparison of the minimum bias measurement with the $20-40\%$ centrality bin from [24] (these two centrality bins have roughly the same average number of participants and so makes for a reasonable comparison). The comparison is shown in Fig. 8.15. The predicted v_2 is still significantly smaller than the measurement and does not seem to describe the data fully.

Another recent calculation claims to solve the thermal photon puzzle, able to account for the large excess yield and the large v_2 [32]. The calculation is performed under the parton-hadron-string-dynamics transport model (PHSD). The authors claim that the discrepancy is observed because of extra sources of direct photons from the hadronic phase are not taken into account in the data and thus are not subtracted. The extra source is from interactions of

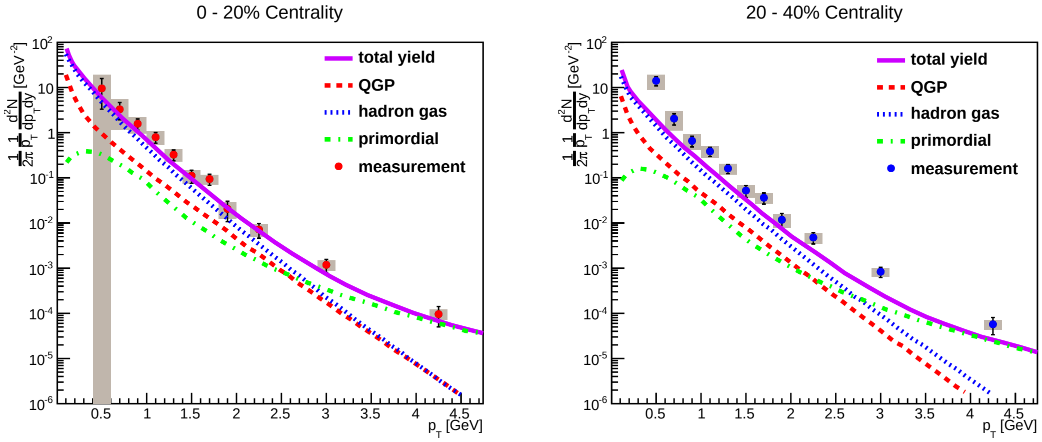

Figure 8.14: A comparison of the invariant yield result in Fig. 5.7 to theory [24], where the yield is dominated by thermal radiation from the hadron gas phase below 3GeV.

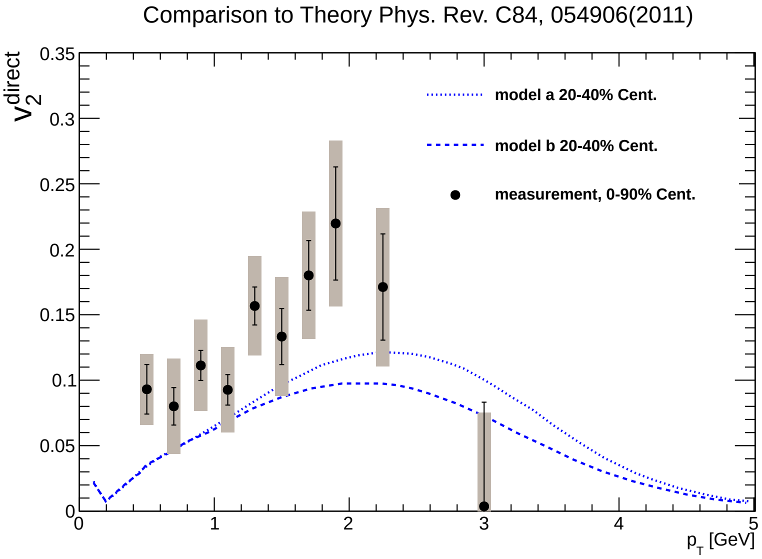

Figure 8.15: A comparison of the direct photon v_2 calculation from [24] is compared to the measurement. Note that the centrality bins for the calculation and the measurement are not exactly the same ($20-40\%$ for the calculation and $0-90\%$ (or minimum bias) centrality for the measurement).

resonances with the medium. The theory is confronted with the data in Fig. 8.16, showing the comparison to both the invariant yield (left panel) and v_2 (right panel) of direct photons for minimum bias collisions. Note that this is for $|y| < 0.5$ around mid-rapidity.

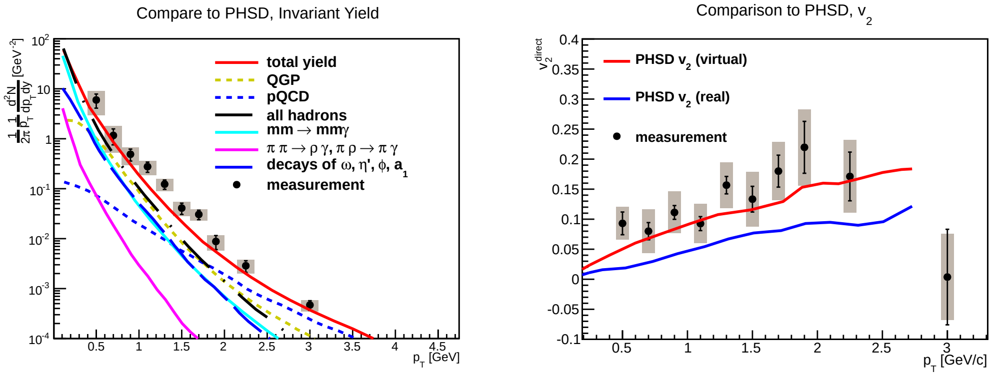

Figure 8.16: A comparison of the direct photon invariant yield (left panel) and the direct photon v_2 (right panel) calculated from the PHSD transport model [32] with the measurement.

As the figure shows and the authors state, the model calculation does a reasonable job describing both the large excess yield and the large observed v_2, but there are a few issues with this calculation that call the validity of its results into question. For one, the authors assume that ω, η', ϕ, and a_1 meson decays are not subtracted from the data and thus are labeled as direct photons in the publication [30]. This is simply not true and the removal of these sources (the dashed blue line) from the PHSD calculation will result in an underprediction of the invariant yield. Secondly, the authors calculate a significantly different direct photon fraction, R_γ, for real ($R_\gamma \sim 1.05$) and virtual ($R_\gamma \sim 1.2$) photons. The authors state that this difference is due to the fact that the contribution from pion decays effectively dies out for masses above the pion mass (and hence in the mass range between 0.15 - 0.3 GeV, where the R_γ is measured in [28]), where as the pion decay contribution still exists when going to zero mass. In fact the contriubtion from pion decays has been subtracted in the current analysis of R_γ from real photons in this thesis, the explanation from the authors of [32] seem to ingore this. The large difference in R_γ for real and virtual photons is clearly ruled out by the current results (see Fig. 5.4). The right side plot of Fig. 8.16 shows the PHSD calculated v_2 with the virtual and real photon R_γ values.

8.3.2 Novel Sources of Direct Photons

Many novel sources of direct photons have been proposed to solve the thermal photon puzzle, some with an azimuthal asymmetry in the production, reproducing the large v_2 observed, along with a comparable excess yield. These novel sources of direct photons are the subject of this section. It should be noted that much time and effort has been devoted to the calculation of conventional thermal sources. The ideas and calculations reviewed and discussed in this section are still in the early stages of development and make somewhat crude approximations which need to be refined for a more realistic picture.

Direct Photons from the Glasma

The basic physics of the Glasma and its place in the evolution of heavy ions collisions has been discussed in Sec. 1.2.1. A significant source of low p_T direct photons can be produced in the pre-equilibrium Glasma stage very early in the collision [62]. An azimuthal asymmetry in the production is also expected, but no explicit calculation has been shown at of the time of writing. In [62], the authors derive an expression for the emission of direct photons from the glasma, shown in Eqn. 8.1.

$$\frac{dN_\gamma}{dy d^2 p_T} \sim \alpha R_0^2 N_{part}^{2/3} \left(\frac{Q_{sat}}{p_T} \right)^\eta \tag{8.1}$$

In the equation, Q_{sat} is the gluon saturation scale, N_{part} is the number of participant nucleons in a collision, α is the fine structure constant, η is a parameter related to the asymmetry between the transverse and longitudinal momentum scales setting the asymmetry of the expansion, and R_0 is a constant with units of length. R_0 is expected to be on the order of 1fm, but can not be exactly determined with the crude approximations made. In the end, the absolute normalization of the yield is not determined from calculation, but is fit to the PHENIX data [27]. The paper sets a framework for further development.

The photons produced happen fairly late in the glasma development after quarks begin to become relevant (remember, gluons dominate early). Under the glasma picture, it is plausible that very few photons are produced in the time period $0 \leq t < 1/Q_{sat}$, since photon production arises from the electromagnetic charge of quarks, but gluons dominates in this time interval. The calculation focuses on production in the time range $1/Q_{sat} \ll t \ll t_{therm}$, where t_{therm} is the thermalization time. In this framework, thermalization mathematically occurs by the splitting apart of two momentum scales (Λ_s is the momentum scale at which the gluons are maximally coherent and Λ is the ultraviolet cutoff) which are initially overlapping. The scales take a long time to separate in the very high energy limit, and possibly at RHIC. This is in contrast to hydrodynamical descriptions which describe data if one assumes a small thermalization time.

Eqn. 8.1 shows that the expected yield of direct photons from the glasma is proportional to N_{part}. Since $Q^2_{sat} \propto N^{1/3}$, the the yield is proportional to $N_{part}^{\frac{2}{3}(1+\eta/4)}$. For their best fit value to the data, the authors report a power of 1.77 for $\eta = 6.65$. η has a maximal range of $9 \geq \eta \geq 25/4$, with the limits of 9 and 25/4 corresponding to maximal anisotropy and isotropic expansion respectively (and so the author's fit to the data seems to indicate isotropic expansion of the intial gluon fields due to no asymmetry between the intial longitudinal and transverse fields). This corresponds to a power of N_{part} in the range of 2.17 to 1.7. The N_{part} power measured in this thesis is $1.40 \pm 0.08 \pm 0.03$. The measured value is about 25% smaller than the power extracted from glasma calculation. The measured value of the power $1.40 \pm 0.08 \pm 0.03$ corresponds to a value of $\eta = 4.4 \pm 0.3 \pm 0.1$. This is actually outside of the allowed range of the η parameter. The model assumes only glasma and primordial production. One would still expect a high rate of thermal photons, which may soften the slope and may explain the result being outside of the physical range.

Fig. 8.17 shows the result of the calculation of direct photons from the glasma. The normalization is not calculated, but is obtained by normalizing to the data. Prompt photon production is included by taking the T_{AA} scaled fit to p+p data. The results are shown for Au+Au Min. Bias, 0-20% and 20-40% centrality selections. As can be seen, a good description of the data can be obtained by considering prompt photon production along with radiation from the glasma before equilibrium of the system is achieved. The next step here is to refine the calculations and calculate the yield on an absolute level, though the calculation already seems to get the correct centrality dependence.

The calculations also need to be extended to the calculation the v_2 of the radiation from the glasma. This is not possible to calculate in the current framework, but it is expected that there is some azimuthal anisotropy, although detailed calculations need to be done to see if the magnitude explains the experimental observations.

Fig. 8.18 compares the result in this thesis to the calculation shown in Fig. 8.17. There is reasonable agreement of the yield for most of the p_T range.

Direct Photons Induced from Strong Magnetic Fields

As discussed in Sec. 1.2.2, very large magnetic fields can be produced in heavy ion collisions. The presence of the magnetic field can modify the yield of

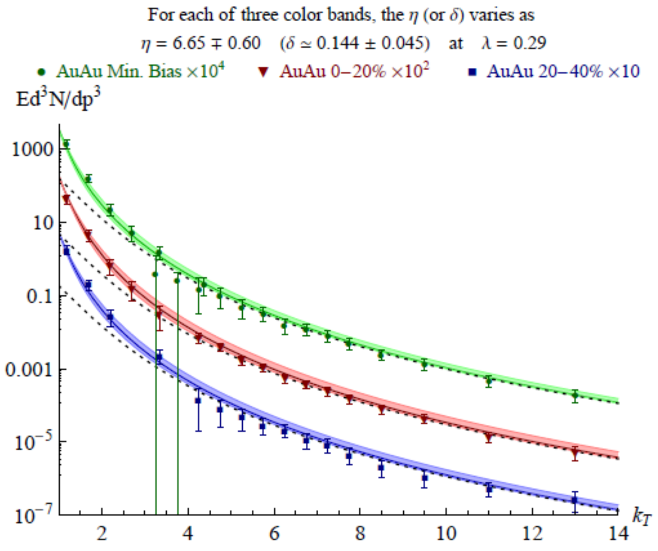

Figure 8.17: The total photon yield including the calculated contribution of emission from the glasma and the prompt contribution. The prompt contribution is from a fit to PHENIX data. The calculation is compared to PHENIX data in centrality selections described in the legend [62].

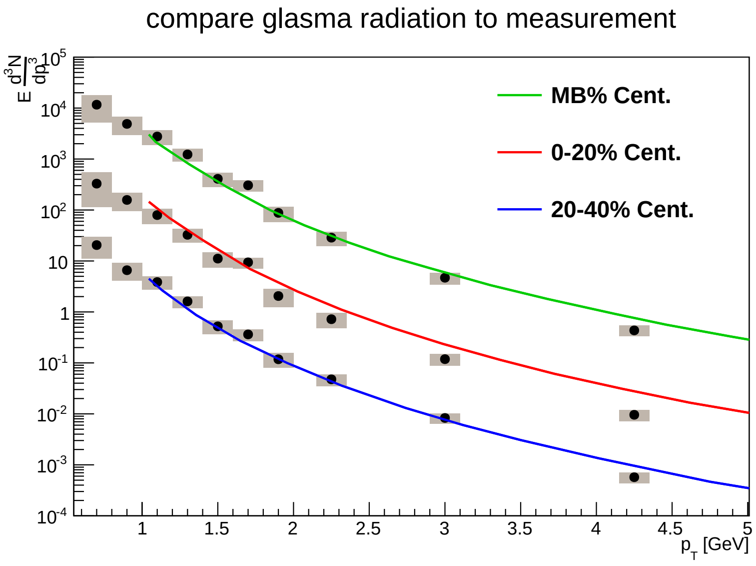

Figure 8.18: A comparison of the invariant yield result in Fig. 5.7 to theory [62], where the yield is calculated from the glasma.

photons emitted from the fireball. One effect is photon decay. In an extremely large magnetic field, photons can decay into e^+e^- pairs. This is discussed in [12] [63] and is calculated to be a small depletion of the photon yield on the order of a few percent at RHIC (but can be up to 20% at the LHC). The decay of photons is azimuthally asymmetric (due to the B field) and can contribute to the observed v_2.

Another effect due the the magnetic field is synchrotron radiation. This is discussed in detail in [12] [64]. It is expected that quarks moving through the strong magnetic field will produce synchrotron radiation. This has an effect on both photon production (via thermal quarks emitting electromagnetic synchrotron radiation) and on jet quenching (via fast quarks emitting gluonic synchrotron radiation). The discussion on jet quenching is outside the current scope of the thesis, but it is interesting to note that it is claimed in [12] that synchrotron radiation of gluons by fast quarks in the high magnetic field alone can account for jet quenching seen in data (currently jet quenching is thought mainly to occur from some combination of collisional energy loss of partons in the plasma and gluon bremsstrahlung processes).

The magnetic field will polarize the emitted photons, and so measuring a polarization of the final photon spectrum will give supporting evidence to the idea of these high magnetic fields.

It is interesting to note that emission due to the strong external magnetic fields should have a characteristic centrality dependence to the yield from these processes. Very naively, one can imagine that in a completely head-on collision the external magnetic field will be zero (or very near so) due to symmetry. On the other hand, as the impact parameter between the ions is increased, the field should grow stronger and stronger. So in a very naive view, the centrality dependence of the yield from strong magnetic fields seems to go in the opposite direction as that is observed. Of course this statement needs to be fully verified as effects from the expansion of the medium and the electrical conductivity of the medium can have an effect on the evolution of the field with time, Fig. 1.10.

Direct Photons from Anomalies of QCD

Anomalies exist in QCD [65]. One such anomaly occurs from the non-vanishing divergence of the dilatational current S_μ, leading to a coupling of QED and QCD in the extremely high magnetic field. This is shown in Eqn. 8.2. In the Eqn. 8.2, $\beta(g)$ is the beta-function of QCD which describes the running of the coupling constant, m_q is the quark mass, and $\gamma_m(g)$ are the corresponding anomalous dimensions. This divergence can be coupled to the magnetic field, producing a photon. This is shown in the diagram of Fig. 8.19.

$$\partial^\mu S_\mu = \theta^\mu_\mu = \frac{\beta(g)}{2g} G^{\mu\nu\alpha} G_{\mu\nu\alpha} + \sum_q m_q [1 + \gamma_m(g)] \bar{q} q \tag{8.2}$$

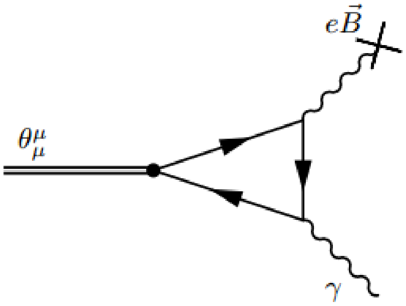

Figure 8.19: The coupling of the diverging current from the conformal anomaly θ^μ_μ to the external magnetic field, eB, resulting in the production of a photon, γ. [65]

The current acting on the vacuum creates color-singlet states, σ, of mass, m_σ, and amplitude, f_σ. In [65], the identification of the lightest σ dilaton with the $f_0(600)$ is made. This dilaton couples to the magnetic field, producing a photon. The bulk hydrodynamical modes of the plasma donate their energy to produce the photons due to their interaction with the anomaly in the presence of the magnetic field.

The calculation in [65] shows that this source of photons can be significant at low momentum and comparable to emission from conventional sources, see Fig. 8.20. Furthermore, they calculate a large v_2 of these photons, comparable to that measured by PHENIX in [30]. The comparison to the current measurement is shown in Fig. 8.21. The calculation finds a v_2 comparable to the measurement.

It is interesting to note that the authors of [65] state that the initial state eccentricity and the conformal anomaly effects on the v_2 can be separated by studying U+U collisions, where the U ions have a significant deformation from spherical (in contrast to Au ions). Collisions of a specific orientation (central body-body) will have no magnetic field present, due to symmetry, but will have a significant eccentricity [67]. Therefore a large v_2 measured would indicate an elliptic flow origin, not magnetic field. Another interesting measurement is a test of the v_4^2/v_2 scaling breaking (expected for a v_2 with production dominated by magnetic field effects). A small v_4^2/v_2 ratio is expected from production from a magnetic field, where hydrodynamics predicts closer to the order of unity. In addition to these measurements, more refined calculations

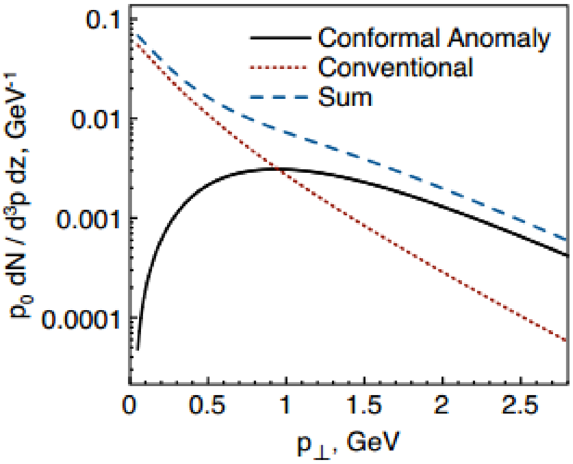

Figure 8.20: The yield of photons from the conformal anomaly compared the the yield of thermal photons calculated on the lattice [65] [66].

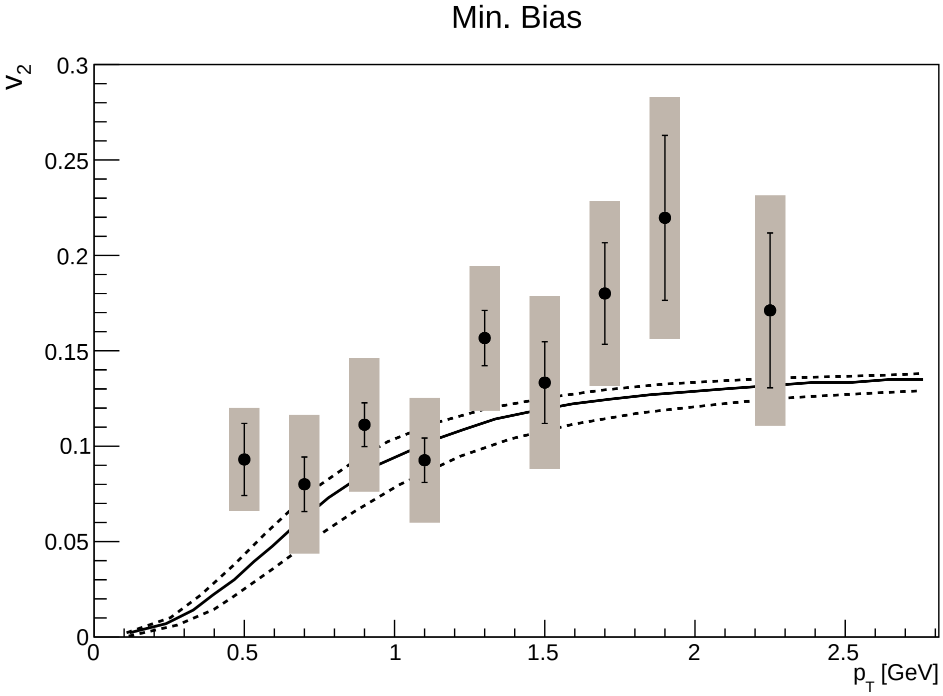

Figure 8.21: A comparison of the direct photon v_2 with the v_2 calculated from emission due to the conformal anomaly [65] to the measured result.

in the models is always desired.

8.4 Conclusions

An analysis on the invariant yield of direct photons in the transverse momentum range of $0.4 < p_T < 5GeV$ in Au+Au collisions at $\sqrt{s_{NN}} = 200GeV$ for the 2007 dataset from RHIC has been detailed and discussed. Additionally, the measurement of the direct photon v_2 has also been discussed in this same momentum range. The measurement has employed a novel technique of photon identification via external conversions to get a clean photon sample ($\sim 99\%$ purity). To further reduce systematic uncertainties to manageable levels, the direct photon fraction R_γ is measured through a double ratio, canceling major sources of uncertainties when forming each ratio of the double ratio.

The measurement makes several improvements to previously published results on the invariant yield of direct photons in Au+Au collisions at $\sqrt{s_{NN}} = 200GeV$. One improvement is that the direct photons are measured down to lower p_T. Another improvement is from the significantly reduced uncertainties on R_γ compared to the preliminary 2004 result from the Emcal only method. This measurement also serves as an important cross-check to the direct photon fraction measured through the virtual photon analysis [28] [27]. The direct photon fractions measured from real photons and from virtual photons is consistent within uncertainties, putting to rest any claims that the two direct photon fractions will differ by a substantial amount. The extended p_T reach (along with the greater statistical precision illustrating by the increase in number of data points in the range of 1-2GeV compared to [27]), allows for an improved constraint on the possible exponential shape of the spectrum. It is found that the excess is not described well by a pure exponential and that the spectral shape of the excess appears to be roughly the same for all centralities (in contrast to the strong centrality dependence of the magnitude of the yield). The analysis further details the centrality dependence of the low momentum direct photon excess above primordial contributions to a greater extent than has been previously achieved. It is found that the invariant yield of the excess is proportional to $N_{part}^{1.40\pm0.08\pm0.03}$ and $N_{qp}^{1.28\pm0.07\pm0.02}$.

This analysis also reports an important cross-check on the surprising direct photon v_2 result published by PHENIX [30]. Consistency on the level of the inclusive photon v_2 is shown in various centrality bins, while the direct photon v_2 measurements are shown to be consistent in minimum bias collisions.

The presented results offer strong constraints to model calculations of sources of direct photons at low momentum. Disentangling these contributions experimentally is very difficult, requiring the need for advancements in both theory and experiment. The centrality dependence of the yield needs to be studied in more detail in the theory. Additional measurements on direct photons for higher flow harmonics in Au+Au and in different collision species (such as U+U) will help to clarify the overall picture. The thermal photon puzzle is not yet solved, but the results in this thesis will be of utmost importance in constraining possible solutions.

Bibliography

[1] H. Geiger & E. Marsden, *Proceedings of the Royal Society* Series A 82, 495500 (1909).

[2] E. Rutherford, *Philosophical Magazine* Series 6 21, 669688 (1911).

[3] F. Halzen, A. Martin Quarks & Leptons: An Introductory Course in Modern Particle Physics, John Wiley & Sons, Inc. 1984.

[4] Siegfried Bethke. Experimental tests of asymptotic freedom. *Prog.Part.Nucl.Phys.*, 58:351–386, 2007.

[5] R. Vogt, *Int. J. Mod. Phys. E* **12**, 211 (2003).

[6] K.J. Eskola, H. Paukkunen, and C.A. Salgado, *JHEP* **04**, 065 (2009).

[7] I. Vitev, *Phys. Rev. C* **75**, 064906 (2007).

[8] A. Adare, S.S. Adler, S. Afanasiev, C. Aidala, N.N. Ajitanand, et al. Direct photon production in d+Au collisions at $\sqrt{s_{NN}} = 200$ GeV. 2012.

[9] A. Adare et al. Scaling properties of azimuthal anisotropy in Au+Au and Cu+Cu collisions at s(NN) = 200-GeV. *Phys.Rev.Lett.*, 98:162301, 2007.

[10] J. -P. Blaizot, F. Gelis, J. -F. Liao, L. McLerran and R. Venugopalan, *Nucl. Phys.* **A 873**, 68 (2012).

[11] Larry McLerran. The Color Glass Condensate and Glasma. 2008.

[12] Kirill Tuchin. Particle production in strong electromagnetic fields in relativistic heavy-ion collisions. *Adv.High Energy Phys.*, 2013:490495, 2013.

[13] B. A. Boyko at. al., *Pulsed Power Conference. Digest of Technical Papers. 12th IEEE International* **2**, 746 (1999).

[14] C. Kouveliotou, R. C. Duncan and C. Thompson, *Sci. Am.* **288N2**, 24 (2003).

[15] U. Heinz and P. Kolb, *Nucl. Phys.* **A702**, 269(2002).

[16] P. Romatschke and U. Romatschke, *Phys. Rev. Lett.* **99**, 172301 (2007).

[17] Z. Xu, C. Greiner, and H. Stocker, *Phys. Rev. Lett.* **101**, 082302 (2008).

[18] A. Adare et al. Measurements of Higher-Order Flow Harmonics in Au+Au Collisions at $\sqrt{s_{NN}} = 200$ GeV. *Phys.Rev.Lett.*, 107:252301, 2011.

[19] K. Adcox et al. Flow measurements via two particle azimuthal correlations in Au+Au collisions at s(NN)**(1/2) = 130-GeV. *Phys.Rev.Lett.*, 89:212301, 2002.

[20] A. Adare et al. Heavy Quark Production in $p + p$ and Energy Loss and Flow of Heavy Quarks in Au+Au Collisions at $\sqrt{s_N N} = 200$ GeV. *Phys.Rev.*, C84:044905, 2011.

[21] Y. L. Dockshitzer and D. E. Kharzeev, *Phys. Lett.* **B519**, 199 (2001).

[22] N. Armesto, A. Dainese, C. A. Salgado, and U. A. Wiedemann, *Phys. Rev. D* **71**, 054027 (2005).

[23] Chatterjee, Srivastava, *Phys. Rev.* **C79**, 021901 (2009).

[24] H. van Hees, *et al.Phys. Rev.* **C84**, 054906(2011).

[25] S. Afanasiev et al. Measurement of Direct Photons in Au+Au Collisions at $\sqrt{s_{NN}} = 200$ GeV. *Phys.Rev.Lett.*, 109:152302, 2012.

[26] A. Adare et al. Suppression pattern of neutral pions at high transverse momentum in Au + Au collisions at s(NN)**(1/2) = 200-GeV and constraints on medium transport coefficients. *Phys.Rev.Lett.*, 101:232301, 2008.

[27] A. Adare et al. Enhanced production of direct photons in Au+Au collisions at $\sqrt{s_{NN}} = 200$ GeV and implications for the initial temperature. *Phys.Rev.Lett.*, 104:132301, 2010.

[28] A. Adare et al. Detailed measurement of the e^+e^- pair continuum in $p+p$ and Au+Au collisions at $\sqrt{s_{NN}} = 200$ GeV and implications for direct photon production. *Phys.Rev.*, C81:034911, 2010.

[29] Chun Shen, Ulrich W Heinz, Jean-Francois Paquet, and Charles Gale. Thermal photons as a quark-gluon plasma thermometer revisited. 2013.

[30] A. Adare et al. Observation of direct-photon collective flow in $\sqrt{s_{NN}} =$ 200 GeV Au+Au collisions. *Phys.Rev.Lett.*, 109:122302, 2012.

[31] Rupa Chatterjee, Dinesh K. Srivastava, and Ulrich Heinz. Time Evolution of Thermal Photon Elliptic Flow. pages 534–536, 2009.

[32] O. Linnyk, V.P. Konchakovski, W. Cassing, and E.L. Bratkovskaya. Photon elliptic flow in relativistic heavy-ion collisions: hadronic versus partonic sources. 2013.

[33] K. Dusling and I. Zahed, *Phys. Rev. C* **82**, 054909 (2010).

[34] M. Allen *et al.Nuclear Inst. and Methods in Physics Research* **A499** 549-559 (2003).

[35] E. Richardson *et al.Nuclear Inst. and Methods in Physics Research* **A636** 99-107 (2011).

[36] S. H. Aronson *et al.Nuclear Inst. and Methods in Physics Research* **A499** 480-488 (2003).

[37] K. Adcox *et al.Nuclear Inst. and Methods in Physics Research* **A499** 489-507 (2003).

[38] A. Oskarsson *et al.*, *Nuclear Inst. and Methods in Physics Research* **A497/2-3** pp 263-293 (2003).

[39] P. Nilsson for the PHENIX pad chamber group *Nuclear Physics* **A661**, 665 (1999).

[40] J. T. Mitchell *et al.Nuclear Inst. and Methods in Physics Research* **A482** 498 (2002).

[41] M. Aizawa *et al.Nuclear Inst. and Methods in Physics Research* **A499** 508-520 (2003).

[42] W. Anderson, B. Azmoun, A. Cherlin, C. Y. Chi, Z. Citron, M. Connors, A. Dubey, J. M. Durham, Z. Fraenkel, T. Hemmick, J. Kamin, A. Kozlov, B. Lewis, M. Makek, A. Milov, M. Naglis, V. Pantuev, R. Pisani, M. Proissl, I. Ravinovich, S. Rolnick, T. Sakaguchi, D. Sharma, S. Stoll, J. Sun, I. Tserruya, and C. Woody. Design, construction, operation and performance of a Hadron Blind Detector for the PHENIX experiment. *Nuclear Instruments and Methods in Physics Research A*, 646:35–58, August 2011.

[43] L. Aphecetche *et al.Nuclear Inst. and Methods in Physics Research* **A499** 521-536 (2003).

[44] S. S. Adler *et al.Nuclear Inst. and Methods in Physics Research* **A499** 560-592 (2003).

[45] S.S. Adler et al. Identified charged particle spectra and yields in Au+Au collisions at S(NN)**1/2 = 200-GeV. *Phys.Rev.*, C69:034909, 2004.

[46] S.S. Adler et al. Suppressed pi$^0 productionatlargetransversemomentumincentralAu+AucollisionsatS(NN) * *1/2 = 200GeV. Phys.Rev.Lett., 91 : 072301, 2003.$

[47] A. Adare et al. Neutral pion production with respect to centrality and reaction plane in Au+Au collisions at $\sqrt{s_{NN}}$=200 GeV. *Phys.Rev.*, C87:034911, 2013.

[48] R. Averbeck PHENIX Internal Analysis Note **349** (2005).

[49] V. Ryabov. First measurement of the omega-meson production at RHIC by PHENIX. *Nucl.Phys.*, A774:735–738, 2006.

[50] S.S. Adler et al. Common suppression pattern of eta and pi0 mesons at high transverse momentum in Au+Au collisions at S(NN)**(1/2) = 200-GeV. *Phys.Rev.Lett.*, 96:202301, 2006.

[51] A. Adare, S. Afanasiev, C. Aidala, N.N. Ajitanand, Y. Akiba, et al. Production of ω mesons in $p + p$, d+Au, Cu+Cu, and Au+Au collisions at $\sqrt{s_N N} = 200$ GeV. *Phys.Rev.*, C84:044902, 2011.

[52] http://www.robots.ox.ac.uk/ mebden/reports/GPtutorial.pdf.

[53] A. Adare et al. Measurement of neutral mesons in p+p collisions at $\sqrt{(s)}$= 200 GeV and scaling properties of hadron production. *Phys.Rev.*, D83:052004, 2011.

[54] Jean-Yves Ollitrault, *Nucl. Phys.* **A590** (1995) 561-564c.

[55] A. M. Poskanzer and S. A. Voloshin, *Phys. Rev.* **C58**, Issue 3, 1671-1678 (1998).

[56] A. Adare et al. Deviation from quark-number scaling of the anisotropy parameter v_2 of pions, kaons, and protons in Au+Au collisions at $\sqrt{s_{NN}} =$ 200 GeV. *Phys.Rev.*, C85:064914, 2012.

[57] S.S. Adler et al. Measurement of direct photon production in p + p collisions at s**(1/2) = 200-GeV. *Phys.Rev.Lett.*, 98:012002, 2007.

[58] A. Adare et al. Direct-Photon Production in $p+p$ Collisions at $\sqrt{s} = 200$ GeV at Midrapidity. *Phys.Rev.*, D86:072008, 2012.

[59] R. J. Glauber, *Phys. Rev.* **100**, 242 (1955).

[60] K. Reygers, *Glauber Monte-Carlo Calculations for Au+Au Collisions at* $\sqrt{s_{NN}} = 200 GeV$ PHENIX Internal Analysis Note 169 (2003).

[61] J. T. Mitchell *et al.*PHENIX Internal Analysis Note **1091** (2013).

[62] Mickey Chiu, Thomas K. Hemmick, Vladimir Khachatryan, Andrey Leonidov, Jinfeng Liao, et al. Production of Photons and Dileptons in the Glasma. *Nucl.Phys.*, A900:16–37, 2013.

[63] Kirill Tuchin. Photon decay in strong magnetic field in heavy-ion collisions. *Phys.Rev.*, C83:017901, 2011.

[64] Kirill Tuchin. Electromagnetic radiation by quark-gluon plasma in magnetic field. *Phys.Rev.*, C87:024912, 2013.

[65] Basar, Gokce, Kharzeev, and Skokov. Conformal anomaly as a source of soft photons in heavy ion collisions. *Phys.Rev.Lett.*, 109:202303, 2012.

[66] H. T. Ding et al., *Phys. Rev.* **D 83**, 034504 (2011).

[67] S. A. Voloshin, *Phys. Rev. Lett.* **105**, 172301 (2010).

Appendix A

Data Tables

R_γ 0-20% Centrality Bin			
$p_T[GeV]$	R_γ	stat. error	sys. error
0.5	1.12111	0.0791906	0.125594
0.7	1.15333	0.0634072	0.0995596
0.9	1.23404	0.0648062	0.0893503
1.1	1.2579	0.0686202	0.083109
1.3	1.28736	0.0770755	0.0820595
1.5	1.25041	0.0809436	0.0788826
1.7	1.398	0.110273	0.0879423
1.9	1.20065	0.0959552	0.0753031
2.25	1.25627	0.0917922	0.0779453
3	1.39125	0.125497	0.0838908
4.25	1.4989	0.237869	0.0961899

Table A.1: The data table for the 0-20% centrality binned direct photon fraction, R_γ, shown in Fig. 5.3.

R_γ 20-40% Centrality Bin			
$p_T[GeV]$	R_γ	stat. error	sys. error
0.5	1.39225	0.0887569	0.140443
0.7	1.21241	0.0594257	0.0953658
0.9	1.21591	0.057315	0.0799818
1.1	1.27212	0.0626204	0.0756473
1.3	1.3007	0.0693589	0.0741205
1.5	1.24047	0.0702609	0.069817
1.7	1.30733	0.0847607	0.0734369
1.9	1.22322	0.0857904	0.0686356
2.25	1.3134	0.0874065	0.073082
3	1.47502	0.121444	0.0796573
4.25	1.49336	0.203364	0.0869452

Table A.2: The data table for the 20-40% centrality binned direct photon fraction, R_γ, shown in Fig. 5.3.

R_γ 40-60% Centrality Bin			
$p_T[GeV]$	R_γ	stat. error	sys. error
0.5	1.1595	0.0779259	0.12675
0.7	1.05988	0.0528528	0.0844881
0.9	1.09546	0.0520857	0.0714303
1.1	1.14049	0.0561782	0.0668506
1.3	1.26178	0.0690067	0.0705254
1.5	1.17661	0.0683756	0.0645539
1.7	1.22472	0.0799916	0.0667173
1.9	1.21219	0.0908954	0.0657811
2.25	1.19192	0.0788647	0.0642209
3	1.10159	0.0826614	0.0584061
4.25	1.38983	0.222579	0.0786536

Table A.3: The data table for the 40-60% centrality binned direct photon fraction, R_γ, shown in Fig. 5.3.

R_γ 60-90% Centrality Bin			
$p_T[GeV]$	R_γ	stat. error	sys. error
0.5	1.12448	0.0813254	0.120324
0.7	0.987948	0.0514598	0.0744577
0.9	1.02541	0.0514419	0.0633161
1.1	1.12079	0.0607982	0.0631223
1.3	1.16046	0.0717593	0.0630818
1.5	1.19228	0.0839259	0.0640342
1.7	1.12592	0.0875223	0.0601931
1.9	1.07636	0.0966749	0.0573458
2.25	0.976564	0.074658	0.0516004
3	1.23039	0.132346	0.0637598
4.25	1.90262	0.540173	0.104288

Table A.4: The data table for the 60-90% centrality binned direct photon fraction, R_γ, shown in Fig. 5.3.

R_γ MB Centrality Bin			
$p_T[GeV]$	R_γ	stat. error	sys. error
0.5	1.20281	0.063771	0.100851
0.7	1.1465	0.0516231	0.0794413
0.9	1.19573	0.0525809	0.0742787
1.1	1.24009	0.0556377	0.0732277
1.3	1.28691	0.0605373	0.0745624
1.5	1.23918	0.0604774	0.0713991
1.7	1.33178	0.0713066	0.0766229
1.9	1.21663	0.0677234	0.0699104
2.25	1.24999	0.0651785	0.0714926
3	1.36275	0.0803636	0.0768795
4.25	1.51183	0.140849	0.0874081

Table A.5: The data table for the MB centrality binned direct photon fraction, R_γ, shown in Fig. 5.4.

Inclusive Photon Invariant Yield MB Centrality Bin			
$p_T[GeV]$	$\gamma^{incl}[(GeV)^{-2}]$	stat. error	sys. error
0.5	30.0525	0.094214	5.70206
0.7	8.25774	0.0199666	1.5668
0.9	3.05686	0.00793297	0.579998
1.1	1.32586	0.00456697	0.251564
1.3	0.516865	0.00249449	0.0980683
1.5	0.235339	0.00157242	0.0446524
1.7	0.116003	0.00105636	0.02201
1.9	0.0533489	0.000656083	0.0101222
2.25	0.0166178	0.000204862	0.00315301
3	0.00188107	3.89613e-05	0.000356907
4.25	0.000146842	8.1832e-06	2.78614e-05

Table A.6: The data table for the MB centrality binned corrected inclusive photon yield shown in Fig. 4.39.

γ^{direct} 0-20% Centrality Bin			
$p_T[GeV]$	$\gamma^{direct}[(GeV)^{-2}]$	stat. error	sys. error
0.5	9.56192	6.2525	9.95818
0.7	3.29173	1.3612	2.16024
0.9	1.57503	0.436125	0.619786
1.1	0.795194	0.211584	0.26725
1.3	0.325941	0.087425	0.0981343
1.5	0.111309	0.0359792	0.0366355
1.7	0.0940647	0.0260626	0.022639
1.9	0.020523	0.0098147	0.00794724
2.25	0.00719742	0.00257803	0.00235555
3	0.00118457	0.000379961	0.000307531
4.25	9.58682e-05	4.57083e-05	2.42667e-05

Table A.7: The data table for the 0-20% centrality binned direct photon invariant yield, γ^{direct}, shown in Fig. 5.7.

γ^{direct} 20-40% Centrality Bin			
$p_T[GeV]$	$\gamma^{direct}[(GeV)^{-2}]$	stat. error	sys. error
0.5	14.0719	3.18417	5.21418
0.7	2.05017	0.573562	0.940994
0.9	0.658864	0.174903	0.252036
1.1	0.385604	0.088737	0.113333
1.3	0.161092	0.0371566	0.0425774
1.5	0.0521884	0.0152483	0.0159489
1.7	0.0362365	0.00999402	0.00932334
1.9	0.0117783	0.00452673	0.00379185
2.25	0.00476326	0.00132845	0.001251
3	0.000831802	0.00021266	0.00018515
4.25	5.72222e-05	2.3587e-05	1.37758e-05

Table A.8: The data table for the 20-40% centrality binned direct photon invariant yield, γ^{direct}, shown in Fig. 5.7.

γ^{direct} 40-60% Centrality Bin			
$p_T[GeV]$	$\gamma^{direct}[(GeV)^{-2}]$	stat. error	sys. error
0.5	2.18601	1.06798	1.7496
0.7	0.218028	0.192454	0.308351
0.9	0.110186	0.0601227	0.0831195
1.1	0.07581	0.0303143	0.036791
1.3	0.0542053	0.014289	0.0154919
1.5	0.0151219	0.00585461	0.00571252
1.7	0.01063	0.00378384	0.00331484
1.9	0.0045984	0.00196981	0.00149152
2.25	0.00124646	0.000512192	0.000443446
3	8.10403e-05	6.59392e-05	4.80771e-05
4.25	2.17416e-05	1.24139e-05	5.65323e-06

Table A.9: The data table for the 40-60% centrality binned direct photon invariant yield, γ^{direct}, shown in Fig. 5.7.

γ^{direct} 60-90% Centrality Bin			
$p_T[GeV]$	$\gamma^{direct}[(GeV)^{-2}]$	stat. error	sys. error
0.5	0.334729	0.218692	0.325135
0.7	-0.00812251	0.0346824	0.0501883
0.9	0.00522407	0.0105777	0.0130289
1.1	0.0114315	0.00575408	0.00607276
1.3	0.00577037	0.00258062	0.00233438
1.5	0.00286343	0.0012498	0.00099193
1.7	0.00104234	0.000724475	0.000508079
1.9	0.000294163	0.000372438	0.000222698
2.25	-2.80505e-05	8.93589e-05	6.1854e-05
3	3.6717e-05	2.1092e-05	1.14951e-05
4.25	1.09867e-05	6.57499e-06	2.20418e-06

Table A.10: The data table for the 60-90% centrality binned direct photon invariant yield, γ^{direct}, shown in Fig. 5.7.

γ^{direct} MB Centrality Bin			
$p_T[GeV]$	$\gamma^{direct}[(GeV)^{-2}]$	stat. error	sys. error
0.5	5.97465	1.87868	3.02523
0.7	1.16459	0.410365	0.641196
0.9	0.489053	0.131383	0.191372
1.1	0.276485	0.0640703	0.0883548
1.3	0.123115	0.0259773	0.034083
1.5	0.0408989	0.0103414	0.0128172
1.7	0.0305221	0.00655979	0.00762653
1.9	0.00878568	0.00274655	0.00295652
2.25	0.00286512	0.000747004	0.000889503
3	0.000468796	0.000103857	0.000120747
4.25	4.34685e-05	1.1962e-05	1.02924e-05

Table A.11: The data table for the MB centrality binned direct photon invariant yield, γ^{direct}, shown in Fig. 5.6.

Inclusive Photon v_2 $0-20\%$ Centrality Bin				
$p_T[GeV]$	v_2	stat. error	corr. sys. error	scale sys. error
0.5	0.0491613	0.00575206	0.000695245	0.00688258
0.7	0.0554021	0.0036701	0.000783505	0.0077563
0.9	0.0716897	0.00345246	0.00101385	0.0100366
1.1	0.0724095	0.0039203	0.00102403	0.0101373
1.3	0.0885822	0.0047846	0.00125274	0.0124015
1.5	0.0871476	0.00608722	0.00123245	0.0122007
1.7	0.107052	0.0078971	0.00151395	0.0149873
1.9	0.10444	0.0102288	0.001477	0.0146216
2.25	0.100388	0.0100601	0.0014197	0.0140543
3	0.0610236	0.0171683	0.000863005	0.00854331

Table A.12: Data Table for the inclusive photon v_2 measured in $0-20\%$ central collisions, shown in Fig. 6.5.

Inclusive Photon v_2 $20-40\%$ Centrality Bin				
$p_T[GeV]$	v_2	stat. error	corr. sys. error	scale sys. error
0.5	0.085987	0.00575341	0.00121604	0.0146178
0.7	0.103714	0.00368256	0.00146674	0.0176314
0.9	0.123099	0.00349638	0.00174088	0.0209268
1.1	0.137653	0.00394676	0.0019467	0.023401
1.3	0.157231	0.00482983	0.00222358	0.0267293
1.5	0.162432	0.00603753	0.00229713	0.0276134
1.7	0.164602	0.00782082	0.00232782	0.0279823
1.9	0.179651	0.0100877	0.00254065	0.0305406
2.25	0.17409	0.00972269	0.002462	0.0295953
3	0.135049	0.0158431	0.00190988	0.0229583

Table A.13: Data Table for the inclusive photon v_2 measured in $20-40\%$ central collisions, shown in Fig. 6.5.

Inclusive Photon v_2 $40-60\%$ Centrality Bin				
$p_T[GeV]$	v_2	stat. error	corr. sys. error	scale sys. error
0.5	0.0962971	0.0126061	0.00136185	0.00385188
0.7	0.132222	0.00815037	0.0018699	0.00528887
0.9	0.158265	0.00778563	0.0022382	0.00633059
1.1	0.147732	0.00888117	0.00208924	0.00590926
1.3	0.185711	0.010782	0.00262634	0.00742842
1.5	0.190771	0.0134562	0.00269791	0.00763085
1.7	0.223959	0.0170746	0.00316726	0.00895838
1.9	0.247577	0.0223348	0.00350126	0.00990306
2.25	0.211098	0.0214402	0.00298538	0.00844394
3	0.23941	0.0330532	0.00338577	0.0095764

Table A.14: Data Table for the inclusive photon v_2 measured in $40-60\%$ central collisions, shown in Fig. 6.5.

Inclusive Photon v_2 Min. Bias Centrality				
$p_T[GeV]$	v_2	stat. error	corr. sys. error	scale sys. error
0.5	0.0717537	0.00384872	0.00101475	0.0107631
0.7	0.0843155	0.00246518	0.0011924	0.0126473
0.9	0.101785	0.00233598	0.00143945	0.0152677
1.1	0.10794	0.00264889	0.0015265	0.016191
1.3	0.128187	0.00323617	0.00181284	0.0192281
1.5	0.128732	0.00407687	0.00182055	0.0193099
1.7	0.145536	0.00526413	0.00205819	0.0218304
1.9	0.152333	0.00682029	0.00215431	0.0228499
2.25	0.145793	0.00661154	0.00206183	0.021869
3	0.117141	0.0109535	0.00165663	0.0175712

Table A.15: Data Table for the inclusive photon v_2 measured in minimum bias collisions, shown in Fig. 6.5.

Direct Photon v_2 MB Centrality Bin				
p_T	v_2	stat. error	corr. sys. error	scale sys. error
0.5	0.104416	0.0250302	0.0364085	0.0156625
0.7	0.088434	0.0193465	0.0497173	0.0132651
0.9	0.124279	0.0154977	0.0446441	0.0186419
1.1	0.0990897	0.0138344	0.0386959	0.0148635
1.3	0.166369	0.0166015	0.0392071	0.0249553
1.5	0.145504	0.0215436	0.0449732	0.0218256
1.7	0.182209	0.0225524	0.0391591	0.0273313
1.9	0.232984	0.0458566	0.0619429	0.0349475
2.25	0.173405	0.0338335	0.0488095	0.0260108
3	0.0648402	0.0427491	0.0317165	0.00972603

Table A.16: Data Table for the direct photon v_2 measured in minimum bias collisiosn, shown in Fig. 7.1.